Forschungszentrum Jülich

Institut für Festkörperforschung

Electronic Structure of Low-Dimensional Magnetic Systems

Valerio Bellini

Jül-3856

Electronic Structure of Low-Dimensional Magnetic Systems

Valerio Bellini

Berichte des Forschungszentrums Jülich ; 3856
ISSN 0944-2952
Institut für Festkörperforschung Jül-3856
D82 (Diss., Aachen, RWTH, 2001)

Zu beziehen durch: Forschungszentrum Jülich GmbH · Zentralbibliothek
52425 Jülich · Bundesrepublik Deutschland
☎ 02461/61-5220 · Telefax: 02461/61-6103 · e-mail: zb-publikation@fz-juelich.de

ABSTRACT

Electronic Structure of Low-Dim. Magnetic Systems

In this thesis we applied a recently developed version of the Screened Korringa-Kohn-Rostoker (SKKR) method for the study of the electronic and magnetic properties of three different low dimensional systems. Firstly we focussed our attention to the study of the magnetic properties at the bcc Fe/Co interfaces, and investigated in particular the relation between the magnetic profile at the interface and the hyperfine fields induced on substitutional Cd probe atoms. The results are compared with the experimental observations obtained by means of TDPAC spectroscopy. Then we took advantage of the favourable scaling of the SKKR method with the system size, and tackled the problem of the magnetic properties of nearly one-dimensional systems. In particular, we investigated the case of infinite monoatomic 4d rows placed on different Ag substrates, exploiting the idea of high Miller index surfaces. Finally, we dealt with the complex band structure of insulators, e.g. of ZnSe, MgO and $SrTiO_3$, which can be used to describe the transport properties in Ferromagnet/Insulator/Ferromagnet junctions and showed how this complex bandstructure can be obtained by means of the SKKR method.

Contents

Chapter 1

Introduction

The study of the magnetic properties of surfaces, ultrathin films and multilayers has received an increasing attention from the physics community during the last decades. The discovery of new magnetic properties have led to a renewed interest in magnetism leading not only to a proper understanding of the underlying physics, but also to possible fascinating industrial applications. Since the reduced dimension significantly modifies the magnetic properties [HOMW98], such low-dimensional systems are of central interest within material science since they offer the possibility to create new materials with uniquely tailored magnetic properties. One of the more representative example in this respect, is the discovery of the Giant Magnetoresistance (GMR) [BGSZ89, BBF$^+$88] and Interlayer Exchange Coupling (IEC) [GSP$^+$86, PMR90] effects in multilayer systems composed of magnetic layers separated by non-magnetic spacer-layers, and the following application in magnetic storage and reading-head devices. Simultaneously, the experimental techniques for crystal growing refined so much that systems like interfaces and overlayers on metals and semiconductors can be constructed with high accuracy. Among them, Molecular Beam Epitaxy (MBE) excelled [CP85] in this goal; since it processes in the ultra-high vacuum regime, a number of diagnostic methods such as reflection high-energy electron diffraction (RHEED), Auger electron spectroscopy (AES) or thermal Energy Atom Scattering (TEAS) can be used for an in situ real-time control of the deposition stage. Moreover with the modern Scanning Tunneling Microscopy (STM) techniques [Bes96] atom resolved information of the surface structure of such materials can be obtained.

From the theoretical point of view the progress made in electronic structure calculations leads nowadays to such a degree of precision regarding the calculated electronic and magnetic properties, that they are of enormous help for the un-

derstanding of the basic processes in solid state physics, and moreover can also interprete or predict the results of the experimental investigations. As a central key these calculations aim at the solution of the Schrödinger equation associated to the many particles system of which the solid is composed. Two different approaches have been adopted to face this problem: the use of taylored parametrized methods, fast and reasonable accurate, or parameter-free, i.e. "*ab initio*", methods, more involved and computationally demanding, but also more flexible and very accurate. Among the different *ab initio* methods, the more successful ones were based on the Density Functional Theory, which allows very elegantly to transform the many-particles problem associated with the Schrödinger equation into an effective single-particle one [HK64, KS65, JG89]. Different sub-categories of *ab initio* programs can be characterized, depending on the basis set chosen for the solution of the Schrödinger equation. Each method presents advantages as well as drawbacks regarding the study of a specific system, and therefore different methods can be more convenient depending on the problem one wants to tackle. For instance the pseudopotential method, for which the basis set is composed by plane waves, was extensively applied for the characterization of the electronic properties of bulk semiconductors as well as semiconductor surfaces, interfaces and heterostructures [CL96]. Other methods like the Linear Muffin-Tin-Orbitals (LMTO) method [Skr83] together with its Tight-Binding version (TB-LMTO) [AJ84], and the Full-Potential-Augmented-Plane-Waves (FLAPW) method [JMA78], describe the crystal by means of the Muffin-Tin concept, and are well suited for the study of closer packed materials, e.g. transition metals.

In this thesis we use the Korringa-Kohn-Rostoker (KKR) method, which is one of the most accurate and flexible *ab-initio* band structure method for the study of periodic systems as well as localized perturbations. The KKR method is based on multiple scattering theory and was originally proposed independently by Korringa [Kor47] and by Kohn and Rostoker [KR54]. Within a Green's function approach, Dupree [KR61], Beeby [Bee67] and Holzwarth [Hol75] developed a first version of the KKR method being able to treat localized perturbations, and successively Zeller und Dederichs [ZD79] integrated it in the frame of the DFT for realistic self-consistent calculations of point defects in metals. Since then, the Jülich group has developed many different conceptual improvements to the KKR method, from the full potential formulation [Dri91, DDZ92], to the introduction of lattice relaxations [PZDS97, SBZD87], to fully relativistic versions developed in collaboration with the Munich group [Ebe, Non00].

Another major implementation, which is also used in this thesis, is the transfor-

mation into the "screened" (also called *tight-binding*) KKR method. In electronic structure calculations the use of tight-binding methods with short-ranged hopping parameters has many advantages. For instance most of our understanding on transition metals and other localized systems comes from a tight-binding picture of localized orbitals with small overlap between nearest-neighboring sites. Moreover tight-binding methods are also from the numerical point of view very favourable, since the short range of the coupling simplifies enormously the complexity and the numerical effort of the calculations and permits to tackle problems, the solution of which is otherwise not attainable. Therefore many attempts have been made in order to combine the simplicity of the tight-binding approaches with the accuracy and precision of *ab-initio* methods. For the KKR method, a screened version was originally proposed by Andersen *et al.* [APS92] and a reasonable way to calculate the screened KKR structure constants was proposed by Szunyogh *et al.* [SÚWK94], but the degree of localization of these structure constants was very poor. A more efficient and transparent way to derive well localized screened KKR structure constants was obtained by Zeller *et al.* [ZDÚ+95, Zel97] and successively implemented into a program able to study layered systems [Wil97, WZD97] and supercells [Zah98]. During this work the existing version of the SKKR code has been further developed in collaboration with N. Papanikolaou to treat on the same footing systems with arbitrary two- or three-dimensional periodicity.

In the **second chapter** of this study the basic concepts of the Density Functional Theory (DFT) and of the Local Spin Density Approximation (LSD) are resumed. In particular we discuss the Kohn-Sham equations and the calculation of the total energy.

In the **third chapter** the "traditional" KKR-Green's function method is reviewed. After a brief summary of the general properties of Green's function, we discuss the scattering from a single potential. Afterwards the case of multiple scatterers and the connection to the KKR method is considered. At the end of the chapter a brief summary of the full potential treatment within this formalism is given.

The main concepts of the *screened* KKR method will be presented in the **fourth chapter**. In the first section the derivation of the ideal structure constants and the problems arising in a "traditional" KKR calculation are discussed. Afterwards we introduce the concept of a reference system; a suitable reference system, which will lead to exponentially decaying "screened" structure constants is presented. After the description of the different geometries which can be studied by the present SKKR program, in section (3.4) a formulation adapted to layered systems is presented.

In the following section the half-space geometry is discussed in detail. At the end test calculations of the surface energy for the three low-index surfaces of Cu are presented; the surface energies calculated by means of slab as well as half-space geometries are compared with other theoretical results in the literature.

In the following chapters we apply these methods to three different systems.

The **fifth chapter** is devoted to the study of the magnetic and hyperfine properties of the *bcc* Fe/Co interfaces, and of dilute and ordered Fe/Co alloys. In the first section the formulas used to calculate the hyperfine fields induced from the magnetic environment at the considered atomic position are described. The rest of the chapter is divided in two parts. The calculations presented in the first part have been motivated by recent experimental investigations of the magnetic properties at the Fe/Co interfaces performed by means of a Time Differential Perturbed Angular Correlation (TDPAC) spectroscopy [SMD+97]; in the work of Swinnen *et al.* [SMD+97] the hyperfine fields of Cd probe atoms, implanted in a *bcc* Fe/Co multilayer system, were measured, and from this the magnetization profile at the Fe/Co interface was deduced based on a model proposed by Stearns for the hyperfine fields [Ste73]. The magnetic moment profile at the Fe/Co (001) and (110) interface obtained with our SKKR program is discussed and compared with other theoretical calculations as well as with the fitted magnetic moment profile suggested by Swinnen *et al.* [SMD+97]. The hyperfine fields of a Cd impurity at the Fe/Co interface are also calculated and a detailed comparison with the experimental measurements is given. In the second part, the attention is shifted to the Fe and Co hyperfine fields at the Fe/Co interface as well as in dilute and ordered FeCo alloys. After a detailed discussion about the origin of the hyperfine field in the *bcc* Fe-Co systems a comparison with the experimental findings obtained by means of Mössbauer and Nuclear Magnetic Resonance (NMR) spectroscopies is presented.

Only recently, by means of MBE techniques together with real time control of the deposition stage, one has succeeded to grow one-dimensional monoatomic rows on stepped surfaces [RHB+93, GBB+00a]. Motivated by the success of the modern experimental techniques, in the **sixth chapter** an investigation of the magnetic properties of monoatomic lines adsorbed on metal substrates is presented. Since among all the materials, the ones which are on the borderline of magnetism, e.g. $4d$ and $5d$ elements, present the more unexpected behaviour regarding their magnetic properties, results for $4d$ monoatomic lines at different Ag substrates are given. In the section (6.1), (6.2) and (6.3) a detailed discussion on the structure and electronic properties of high Miller index surfaces used as a template for the characterization of the magnetic lines is given. The attentions is also devoted to the calculations

of Cu and Ag step energies. In section (6.4) the results for the $4d$ magnetic lines at the (711), (410) and (221) Ag high-index surfaces are presented, and at the end of the chapter the occurrence of ferro- or antiferromagnetic order in these rows is investigated by means of total-energy calculations. For the large size of the systems considered, these calculations have to be viewed as a first challenging application of our *Screened* KKR program.

In the **seventh chapter** one of the implementations to the SKKR program, which was performed during this study, is described, i.e. the calculation of real and complex band structures. After a brief discussion on the importance of the complex band structures for an intuitive interpretation of the transport properties in metal/insulator/metal tunnel junctions, the complex band structures of ZnSe, MgO and $SrTiO_3$ are presented.

In the **eigth chapter** a short summary of the results of this thesis is given.

Chapter 2

Density Functional Theory (DFT)

This chapter intends to give a very brief summary of the basic concepts of Density Functional Theory (DFT). This method has been applied since the first formulation of Hohenberg-Kohn and Kohn-Sham [HK64, KS65] to the study of many particle systems; it provides a practical and computationally efficient scheme of solving the Schrödinger equation of N-interacting electrons for the study of electronic and magnetic properties (in its spin polarized formulation) of solids, atoms and molecules. Herewith I follow the presentation offered by Parr and Yang [PY89], and refer to this article and the references therein for a more in-depth presentation of DFT and related theories.

2.1 Schrödinger equation

Let us consider a system of N-interacting electrons in the presence of an external potential $v(\mathbf{r})$, namely the potential due to the nuclei of charges Z_α. For the two components (electrons + nuclei) system, we adopt the so called *adiabatic approximation.* Due to the much smaller electron mass, the electrons adjust practically instantaneously to the motion of the heavy nuclei; the nuclear coordinates can therefore be considered as parameters and only the coordinates of the electrons occur as variables in the Schrödinger equation.

For a system with time-independent interactions, we can write the Hamilton operator (in atomic units [1]) as

$$\hat{H} = \sum_{i=1}^{N}(-\nabla_i^2) + \sum_{i=1}^{N} v(\mathbf{r}_i) + \sum_{ij}^{N} \frac{1}{\mathbf{r}_{ij}} + \sum_{\alpha\beta} \frac{Z_\alpha Z_\beta}{\mathbf{R}_{\alpha\beta}} \ , \tag{2.1}$$

[1] i.e. $\hbar = 1$, $m_e = \frac{1}{2}$, $e^2 = 2$ and $a_0 = 0.529177\,\mathring{A}$, the Bohr radius, as length unit.

in which $v(\mathbf{r}_i) = -\sum_\alpha \frac{Z_\alpha}{\mathbf{r}_{i\alpha}}$ is the "external" potential acting on the electron i due to the nuclei with charges Z_α.
We can rewrite (2.1), considering only the electronic part, in a more compact form, i.e.

$$\hat{H} = \hat{T} + \hat{V}_{ne} + \hat{V}_{ee} \quad \text{with}$$
$$\hat{T} = \sum_{i=1}^{N}(-\nabla_i^2) \quad , \quad \hat{V}_{ne} = \sum_{i=1}^{N} v(\mathbf{r}_i) \quad \text{and} \quad \hat{V}_{ee} = \sum_{ij}^{N} \frac{1}{\mathbf{r}_{ij}} \tag{2.2}$$

where the three terms are, respectively, the kinetic ($\hat{T}$), the electron-nucleus attraction ($\hat{V}_{ne}$) and the electron-electron repulsion ($\hat{V}_{ee}$) energy operators.

With the Hamilton operator $\hat{H}$ the Schrödinger equation reads

$$\hat{H}\,\Psi = E\,\Psi \tag{2.3}$$

where $\Psi = \Psi(\mathbf{x}_1, \mathbf{x}_2, ..., \mathbf{x}_N)$ is the electronic wave function, E the electronic energy eigenvalue and $\mathbf{x}_i$ comprises the atomic coordinate $\mathbf{r}_i$ and the spin coordinate s_i of electron no. i. A full set of wave functions $\{\Psi\}$ can be solution of the (2.3), and each Ψ will be associated with an energy eigenvalue E. If we denote the ground state energy by E_0 and the ground state wave function Ψ_0, the following variational principle due to Ritz holds:

$$E[\Psi] = (\Psi, H\Psi) \geq E_0 = E[\Psi_0] \tag{2.4}$$

provided the wave functions Ψ used in the variation are normalized and satisfy Pauli's principle. Thus the minimization of the functional $E[\Psi]$ with respect to Ψ provides the ground state of the N electrons system. Equivalently, since the Hamilton operator $\hat{H}$ is determined completely by the external potential $v(\mathbf{r})$ acting on the N-electron system, $v(\mathbf{r})$ will determine all properties of the ground state.

2.2 Hohenberg-Kohn theorems

If we introduce the electronic density $n(\mathbf{r})$ defined as the number of electrons per unit volume in a given state Ψ,

$$n(\mathbf{r}_1) = N \int \cdots \int |\Psi(\mathbf{x}_1, \mathbf{x}_2, ..., \mathbf{x}_N)|^2 ds_1 d\mathbf{x}_2 \cdots d\mathbf{x}_N \tag{2.5}$$

which satisfies the condition $\int n(\mathbf{r})d\mathbf{r} = N$, we can formulate the first Hohenberg-Kohn theorem. It states that "the external potential $v(\mathbf{r})$ is determined, within a

trivial additive constant, by the ground state density $n_0(\mathbf{r})$". The second Hohenberg-Kohn theorem accordingly shifts the problem of the functional minimization in the (2.4) from the wave functions to the more simple electron density $n(\mathbf{r})$, i.e.

$$E[n(\mathbf{r})] \geq E_0 = E[n_0(\mathbf{r})] \tag{2.6}$$

where E_0 is the ground state energy; in order to write the above functional minimization, the density $n(\mathbf{r})$ has to be v-representable, i.e. it has to be associated with the antisymmetric ground state wave function of an (interaction-free) N-particle Hamiltonian (2.1). We can then write $E[n]$ as the sum of three terms

$$E[n] = T[n] + V_{ne}[n] + V_{ee}[n] \tag{2.7}$$

each of them being functional of the density $n(\mathbf{r})$.

The v-representable ground-state density has then to fulfill the stationary principle

$$\delta \left\{ E[n(\mathbf{r})] - \mu \left[\int n(\mathbf{r}) d\mathbf{r} - N \right] \right\} = 0 \tag{2.8}$$

where the total number N of electrons is imposed through the Lagrangian parameter μ which is the *chemical potential.* Eq. (2.8) leads to the Euler-Lagrange equation

$$\mu = \frac{\delta E[n]}{\delta n(\mathbf{r})} \tag{2.9}$$

which can be considered as the basic equation of the Density Functional Theory.

2.3 Kohn-Sham equations

Already in 1920s in the Thomas-Fermi model [Tho27, Fer27] it was understood that the electron energy E could be seen as a functional of the electron density, but just with the advent of the Hohenberg-Kohn contribution [HK64], the full implications of this statement have become more evident. The principle idea was to look at the Thomas-Fermi model as an approximation of an *exact* theory. In order to show this we write the energy functional $E[n]$ separating the kinetic term and the electron-electron repulsion term from the electron-external potential term, i.e.

$$E[n] = \int n(\mathbf{r}) v(\mathbf{r}) d\mathbf{r} + F[n] \tag{2.10}$$

where,

$$F[n] = T[n] + V_{ee}[n] \ . \tag{2.11}$$

From the Euler-Lagrange equation (2.9) we have then

$$\mu = v(\mathbf{r}) + \frac{\delta F[n]}{\delta n(\mathbf{r})} \ . \tag{2.12}$$

Instead of giving explicit approximate formula for $T[n]$ and $V_{ee}[n]$ (like in the Thomas-Fermi model), Kohn and Sham [KS65] proposed an indirect approach to the kinetic functional $T[n]$.

Let us suppose to consider a system of N noninteracting electrons; the ground state wave function is given by the determinant

$$\Psi_s = \frac{1}{\sqrt{N!}} \det[\psi_1 \cdots \psi_2] \tag{2.13}$$

with ψ_i the lowest N eigenstates of the one-electron Hamiltonian $\hat{h}_s$

$$\hat{h}_s \psi_i = [-\nabla^2 + v_s(\mathbf{r})]\psi_i = \epsilon \psi_i \tag{2.14}$$

where $v_s(\mathbf{r})$ is an external potential. The ground state density can be written as a sum over the occupied single particle wave functions as

$$n(\mathbf{r}) = \sum_i^N \sum_s |\psi_i(\mathbf{r}, s)|^2 \ . \tag{2.15}$$

For such a system the kinetic energy can be calculated by the following equation:

$$T_s = \sum_i^N \sum_s \langle \psi_i | - \nabla^2 | \psi_i \rangle \ . \tag{2.16}$$

The Kohn-Sham idea [KS65] consists in rearranging the energy functional (2.10) of the interacting system, in such a way that the kinetic energy functional in first-order is replaced by the one of a noninteracting system in the presence of a particular external potential, which can be exactly evaluated by considering the Eq. (2.15) and (2.16) as an implicit representation of this functional $T_s[n]$. We can rewrite (2.11) as

$$F[n] = T_s[n] + J[n] + E_{xc}[n] \tag{2.17}$$

$$E_{xc}[n] = T[n] - T_s[n] + V_{ee}[n] - J[n] \tag{2.18}$$

where the classical part of $V_{ee}[n]$, the Coulomb term $J[n]$, is extracted from $V_{ee}[n]$, and the exchange-correlation energy $E_{xc}[n]$ contains also a kinetic correction $T - T_s$. The Euler-Lagrange equation gives then

$$\mu = v_{eff}(\mathbf{r}) + \frac{\delta T_s[n]}{\delta n(\mathbf{r})} \tag{2.19}$$

with

$$v_{eff}(\mathbf{r}) = v(\mathbf{r}) + \int \frac{n(\mathbf{r}')}{|\mathbf{r} - \mathbf{r}'|} d\mathbf{r}' + v_{xc}(\mathbf{r}) \tag{2.20}$$

being the Kohn-Sham effective potential v_{eff} and $v_{xc}(\mathbf{r})$ the exchange-correlation potential given by

$$v_{xc}(\mathbf{r}) = \frac{\delta E_{xc}[n]}{\delta n(\mathbf{r})} \ . \tag{2.21}$$

If we look at (2.19), we recognize the same equation one would obtain by applying density functional theory to a system of noninteracting electrons moving under the influence of the external potential $v_s(\mathbf{r}) = v_{eff}(\mathbf{r})$; for a given $v_{eff}(\mathbf{r})$, in order to obtain the $n(\mathbf{r})$, from the solution of (2.19), we have now to solve a system of single-particle equations,

$$[-\nabla^2 + v_{eff}(\mathbf{r})]\psi_i = \epsilon_i \psi_i \tag{2.22}$$

$$\text{with} \qquad n(\mathbf{r}) = \sum_i^N \sum_s |\psi_i(\mathbf{r}, s)|^2 \ . \tag{2.23}$$

Equations (2.20) (2.22) and (2.23) are the well known Kohn-Sham equations; they have to be solved self-consistently in order to obtain the electron density $n(\mathbf{r})$ which minimizes the energy functional (2.10).

The KS-eigenvalues ϵ_i unfortunately have no direct physical meaning, because the KS-orbitals ψ_i have only been introduced to sum up to the correct total electron density $n(\mathbf{r})$; a second important point is that the theory up to now is *exact* for the ground state and all the complications of the many-body problem is shifted on the choice of the exchange-correlation potential v_{xc}. This means that if the exchange-correlation potential v_{xc} would be known exactly, then the Eq. (2.10) would give the correct total energy of the N-electron interacting system. To this point I will come back in section 2.5, where the Local Density Approximation (LDA) of the exchange-correlation potential is discussed.

2.4 Total energy

If we indicate with $\tilde{v}_{eff}$ an effective trial potential (approximation of the exact one v_{eff}) the kinetic energy of the system can then be derived from (2.16) and (2.22) as

$$T_s[n] = \sum_i^N \epsilon_i - \int n(\mathbf{r}) \tilde{v}_{eff} d\mathbf{r} \ . \tag{2.24}$$

Using (2.10) and (2.17) we can express the total energy functional as the sum of two contributions [DWZD89], the single-particle term $E_{sp}[n]$ and the double-counting term $E_{dc}[n]$

$$E[n] = E_{sp}[n] + E_{dc}[n] \tag{2.25}$$

$$E_{sp}[n] = \sum_{i}^{N} \epsilon_i \tag{2.26}$$

$$E_{dc}[n] = -\int n(\mathbf{r})\tilde{v}_{eff}d\mathbf{r} + \int n(\mathbf{r})v(\mathbf{r})d\mathbf{r} + \int\int \frac{n(\mathbf{r})n(\mathbf{r}')}{|\mathbf{r}-\mathbf{r}'|}d\mathbf{r}d\mathbf{r}' + E_{xc}[n] \tag{2.27}$$

where the Coulomb term $J[n]$ has been written explicitly. In usual calculations for the bulk systems the Fermi energy is determined such that charge neutrality is achieved. In calculation for systems like impurities in metals or metallic surfaces, the Fermi level is fixed by the bulk and neutrality can only been achieved through a selfconsistently determined "screened" potential $v_{eff}(\mathbf{r})$. Since in these calculations the deviation of the potential $v_{eff}(\mathbf{r})$ from the bulk value is restricted to a finite region around the impurity or at the surface, charge neutrality cannot be achieved correctly, with remanent charges of typically $10^{-2} - 10^{-3}$ electrons. In such non-charge conserving calculations one has to go back to eq. (2.8) in order to be able to calculate reliable total energies,

$$\tilde{E}[n(\mathbf{r})] = E[n(\mathbf{r})] - E_F\left[\int n(\mathbf{r})d\mathbf{r} - N\right] \tag{2.28}$$

which, as is shown in [DWZD89], is extremal also for non-particle conserving variation $\delta n(\mathbf{r})$. The single-particle contribution $E_{sp}[n]$ becomes then,

$$E_{sp}[n] = \int^{E_F} \epsilon n(\epsilon)d\epsilon - E_F\left[\int^{E_F} d\epsilon n(\epsilon) - N\right] \tag{2.29}$$

where $n(\epsilon)$ is the density of states. By introducing the integrated density of states $N(E) = \int^{E} n(\epsilon)d\epsilon$ the expression can be tranformed to

$$E_{sp}[n] = E_F N + \int^{E_F} d\epsilon(\epsilon - E_F)n(\epsilon) = E_F N - \int^{E_F} d\epsilon N(\epsilon)\ . \tag{2.30}$$

The change in the integrated density of states $\Delta N(E)$, due to the presence of the defect, has to be calculated either by summing shell-by-shell or in a analytical way through the Lloyd's formula; for a discussion of this problem I refer to [DWZD89].

2.5 Local Density Approximation

As anticipated in section (2.3), in order to the treat a real system, we have to supply an approximate form of the exchange-correlation potential, which contains the complicated many-particle properties of the N-electron system. Already in their 1965's paper, Kohn-Sham [KS65] proposed what still nowadays is considered a good approximation for v_{xc}, the Local Density Approximation (LDA). In the LDA, the exchange-correlation functional is given by the formula

$$E_{xc}^{LDA}[n] = \int n(\mathbf{r})\epsilon_{xc}(n(\mathbf{r}))d\mathbf{r} \tag{2.31}$$

where $\epsilon_{xc}(n)$ denotes to the exchange-correlation energy of a uniform-electron gas of density n being a simple function of n. The corresponding exchange-correlation potential results to be

$$v_{xc}^{LDA}(\mathbf{r}) = \frac{\delta E_{xc}^{LDA}(n)}{\delta n(\mathbf{r})} = \epsilon_{xc} + n(\mathbf{r})\left.\frac{\delta \epsilon_{xc}(n)}{\delta n}\right|_{n(\mathbf{r})} . \tag{2.32}$$

The usual approach to ϵ_{xc} is to separate the two contributions, the exchange and the correlation terms; the first one is the Dirac exchange-energy functional [PY89], given by

$$\epsilon_x(n(\mathbf{r})) = -\frac{3}{4}\left(\frac{3}{\pi}\right)^{1/3} n(\mathbf{r})^{1/3} \tag{2.33}$$

and for the second a parametrization is used (e.g.. the one of Vosko, Wilk and Nusair [VWN80] in the case of spin-polarized systems) fitted to Monte Carlo results for the homogeneous electron gas (jellium) [CA80]). At first glance, Eq. (2.31) seems to provide good results just for slowly (in space) varying densities, while it turned out that also for inhomogeneous systems (atoms, molecules, solids) the LDA gives generally good ground states properties.

2.6 Spin Density Functional Theory

In order to study of the magnetic properties of materials, one is forced to formulate a spin-polarized version of the DFT [vBH72]. The charge density n and magnetization density m are defined as

$$n(\mathbf{r}) = n^+(\mathbf{r}) + n^-(\mathbf{r}) , \tag{2.34}$$

$$\text{and } m(\mathbf{r}) = n^+(\mathbf{r}) - n^-(\mathbf{r}) \tag{2.35}$$

where $n^+(\mathbf{r})$ and $n^-(\mathbf{r})$ are the density of electron with spin "up" and spin "down".

In the Spin Density Functional Theory (SDFT) the second Hohenberg-Kohn theorem can be rewritten as a functional simultaneously of the spin "up" and spin "down" electron density as

$$E[n^+(\mathbf{r}), n^-(\mathbf{r})] \geq E[n_0^+(\mathbf{r}), n_0^-(\mathbf{r})] = E_0 \ . \tag{2.36}$$

Since the presence of an external magnetic field $\mathcal{H}(\mathbf{r})$ introduces a one-electron term into the energy functional, Eq. (2.10) becomes (in the case of collinear magnetism)

$$E[n^+, n^-] = \int n(\mathbf{r})v(\mathbf{r})d\mathbf{r} - \int \mathcal{H}(\mathbf{r})m(\mathbf{r})d\mathbf{r} + F[n^+, n^-] \tag{2.37}$$

where $F[n^+, n^-]$ is then given by the following terms

$$F[n^+, n^-] = T_s[n^+, n^-] + J[n] + E_{xc}[n^+, n^-] \ . \tag{2.38}$$

The spin dependent effective potential is then defined as

$$v_{eff}^{\sigma}(\mathbf{r}) = v^{\sigma}(\mathbf{r}) + \int \frac{n(\mathbf{r}')}{|\mathbf{r} - \mathbf{r}'|}d\mathbf{r}' + \frac{\delta E_{xc}[n^+(\mathbf{r}), n^-(\mathbf{r})]}{\delta n^{\sigma}(\mathbf{r})} \tag{2.39}$$

where we grouped together into $v^{\sigma}(\mathbf{r})$ the nuclear potential and the magnetic interaction term. The charge and magnetization densities can then be obtained from the spin polarized wave functions $\psi_i^{(\sigma)}$,

$$n^+ = \sum_i \left|\psi_i^{(+)}(\mathbf{r})\right|^2 \quad \text{and} \quad n^- = \sum_i \left|\psi_i^{(-)}(\mathbf{r})\right|^2 \tag{2.40}$$

which are the solutions of the spin-resolved single particle equations

$$[\nabla^2 + v_{eff}^{\sigma}(\mathbf{r})]\psi_i^{(\sigma)} = \epsilon_i^{\sigma}\psi_i^{(\sigma)} \ . \tag{2.41}$$

Even in the case of zero external magnetic field $\mathcal{H} = 0$, the above discussed SDFT is of dramatic importance while it allows to "build" more physics by introducing spin-dependent exchange-correlation functionals. Similarly to the DFT, a very simple approximation was proposed, the Local Spin Density Approximation (LSDA); in the LSDA the exchange-correlation energy is approximated by

$$E_{xc}[n^+, n^-] \simeq E_{xc}^{LSDA}[n^+, n^-] = \int n(\mathbf{r})\epsilon_{xc}(n^+(\mathbf{r}), n^-(\mathbf{r}))d\mathbf{r} \tag{2.42}$$

where $\epsilon_{xc}(n^+(\mathbf{r}), n^-(\mathbf{r}))$ is the exchange-correlation energy of a homogeneous spin polarized electron gas.

Chapter 3

The KKR Green's Function method

As already discussed in the previous chapter, the ground state properties of a system of N-interacting electrons are fully determined by the electron density that minimize the energy functional (2.10). There are two kinds of approaches in order to calculate the ground state density; either solving the single particle wavefunctions using Eq. (2.22) and from this the density (2.23) or by introducing Green's functions. In this chapter I will describe one of the methods which use Green's functions to solve the Schrödinger equation, the Korringa-Kohn-Rostoker (KKR) method [Kor47, KR54], which is based on multiple scattering theory. After a brief introduction on Green's functions (for a review on Green's functions theories I refer to [Eco79]), I will discuss the problem of the scattering from a single Muffin-Tin potential and subsequently move to a system of multiple scatterers. The description of the basic ideas to obtain the *screened* version of the KKR, used to obtain the results presented in the present work, will be postponed to the next chapter.

3.1 Green's functions and physical observables

Let us return to the Schrödinger equation associated to an Hamilton operator $\hat{H}$, describing a single particle under the influence of a local potential $\hat{V} = \hat{V}(\mathbf{r})$, which for simplicity is in this chapter assumed to be spin-independent,

$$\hat{H}\psi = (\hat{H}_0 + \hat{V})\psi = E\psi \ , \tag{3.1}$$

where $\hat{H}_0$ is the Hamilton operator for the free-electron, i.e. $\hat{V} = 0$, and ψ is the electronic wave function. We can rearrange the terms in the above equation,

obtaining

$$(\hat{H}_0 - E)\psi = -\hat{V}\psi \ , \tag{3.2}$$

where the potential $\hat{V}$ appears as an inhomogeneity in the space. If the term $\hat{V}\psi$ is replaced by a Dirac's δ perturbation, we can define the Green's function $\mathcal{G}_0$ of the unperturbed Hamiltonian H_0 (in the $\mathbf{r}$-representation)

$$(-\nabla^2 - E)\mathcal{G}_0(\mathbf{r}, \mathbf{r}'; E) = -\delta(\mathbf{r} - \mathbf{r}') \ , \tag{3.3}$$

where the Hamiltonian of the free-particle system $\hat{H}_0 = -\nabla^2$ has been written explicitly (in atomic units). The Green's function $\mathcal{G}_0(\mathbf{r}, \mathbf{r}'; E)$ describes the propagation of a free particle which has been inserted at position $\mathbf{r}'$ into the system. From (3.2) and (3.3), we can derive the *Lippmann-Schwinger equation* for the wave-functions

$$\psi(\mathbf{r}) = \psi_0(\mathbf{r}) + \int \mathcal{G}_0(\mathbf{r}, \mathbf{r}'; E)V(\mathbf{r}')\psi(\mathbf{r}')d\mathbf{r}' \ , \tag{3.4}$$

where ψ_0 is the solution of the free-particle Schrödinger equation

$$-\nabla^2\psi_0 = E_0\psi_0 \tag{3.5}$$

which satisfies the appropriate boundary condition for an incoming wave. Analogously $\mathcal{G}_0(\mathbf{r}, \mathbf{r}'; E)$ is the retarded or causal Green function obtained from $\mathcal{G}_0(E + i\gamma)$ in the limit of $\gamma \to +0$.

We can similarly, define the Green's function $\mathcal{G}(\mathbf{r}, \mathbf{r}'; E)$ in the presence of the source $[\delta(\mathbf{r} - \mathbf{r}') + \hat{V}\mathcal{G}(\mathbf{r}, \mathbf{r}'; E)]$ as the solution of

$$(H_0 - E)\mathcal{G}(\mathbf{r}, \mathbf{r}'; E) = -\underbrace{[\delta(\mathbf{r} - \mathbf{r}') + \hat{V}\mathcal{G}(\mathbf{r}, \mathbf{r}'; E)]}_{\text{source } Q(\mathbf{r}, \mathbf{r}')} \ . \tag{3.6}$$

Inserting (3.3) in the above equation we obtain in operator notation

$$-\hat{G}_0^{-1}\hat{G} = -\hat{Q}$$

which transforms to

$$\hat{G} = \hat{G}_0\hat{Q}$$

Inserting the explicit value of the source term $Q(\mathbf{r}, \mathbf{r}')$, we obtain in the $\mathbf{r}$-representation the linear inhomogeneous integral Lippmann-Schwinger equation for the Green's functions

$$\mathcal{G}(\mathbf{r}, \mathbf{r}'; E) = \mathcal{G}_0(\mathbf{r}, \mathbf{r}'; E) + \int \mathcal{G}_0(\mathbf{r}, \mathbf{r}''; E)V(\mathbf{r}'')\mathcal{G}(\mathbf{r}'', \mathbf{r}'; E)d\mathbf{r}'' \ , \tag{3.7}$$

Other useful relations can be obtained from (3.7); if we write the Dyson equation in operator notation as

$$\hat{G} = \hat{G}_0 + \hat{G}_0 \hat{V} \hat{G} \tag{3.8}$$

expanding iteratively the term $\hat{G}$ on the right side of the above equation we obtain,

$$\begin{aligned} \hat{G} &= \hat{G}_0 + \hat{G}_0 \hat{V} \hat{G}_0 + \hat{G}_0 \hat{V} \hat{G}_0 \hat{V} \hat{G}_0 + \cdots \\ &= \frac{1}{1 - \hat{G}_0 \hat{V}} \hat{G}_0 = \hat{G}_0 + \hat{G}_0 \hat{T} \hat{G}_0 \end{aligned} \tag{3.9}$$

where we define the T-matrix as

$$\hat{T} = \hat{V} \frac{1}{1 - \hat{G}_0 \hat{V}} \tag{3.10}$$

Eq. (3.7) expresses one of the main principle of the Green's function technique. It states that for two system with Hamiltonians $\hat{H}_0$ and $\hat{H}_0 + \hat{V}$, it is always possible to write a relation between the associated Green's functions, $\hat{\mathcal{G}}$ and $\hat{\mathcal{G}}_0$, on condition that the perturbation $\hat{V}$ is known. For instance, an atom where the electrons move under the action of a potential $\hat{V}$, can be considered as a perturbation to the free-space. But, much more generally, we can consider whatsoever system as a "reference", and look at every other system as a "perturbation" to it; for their Green's function the relation (3.7) holds, on condition that we replace $\hat{V}$ with the more general perturbation $\Delta V = \hat{V} - \hat{V}_0$. This introduces a certain freedom in the choice of the reference system. The choice will depend on the real system we intend to study; in the traditional KKR approach the surfaces are considered as perturbations to a perfect crystal [Lan96], very similarly to how impurities, in bulk or at surfaces, have been treated throughout the years [ZD79, BZLD84, PZD80]. However also fictitious reference systems can be choosen. For instance, in the screened KKR-method we introduce a system with strongly repulsive potentials, in order to obtain reference Green's functions which decay exponentially.

Another important characteristic of the Green's function approach becomes evident as soon as we write explicitly the connection between the Green's function and the wave functions, using the so-called *spectral representation* of the Green's function,

$$\mathcal{G}(\mathbf{r}, \mathbf{r}'; E) = \lim_{\gamma \to 0^+} \sum_{\alpha} \frac{\psi_\alpha(\mathbf{r}) \psi_\alpha{}^*(\mathbf{r}')}{E + i\gamma - E_\alpha} \ , \tag{3.11}$$

where $\psi_\alpha(\mathbf{r})$ and E_α are the eigenfunctions and eigenvalues of Eq. (3.1), and the infinitesimally small positive quantity γ guarantees the causality of the Green's

function. Physical observables like electron density $n(\mathbf{r})$ and consequently magnetic moments, can be easily derived from Eq. (3.11). If we consider the diagonal elements, i.e. $\mathbf{r} = \mathbf{r}'$, of the Green's function in Eq. (3.11) we can rewrite them as,

$$\mathcal{G}(\mathbf{r},\mathbf{r};E) = \sum_{\alpha} |\psi_\alpha(\mathbf{r})| \lim_{\gamma\to+0} \frac{2}{E + i\gamma - E_\alpha} \tag{3.12}$$

Using the Dirac's identity

$$\lim_{\gamma\to+0} \frac{1}{x \pm i\gamma} = \mathcal{P}\left(\frac{1}{x}\right) \mp i\pi\delta(x)$$

where $\mathcal{P}$ is the Cauchy's Principal Value, and considering only the imaginary part of the equation, we obtain

$$n(\mathbf{r}) = \sum_{E_\alpha<E_F} |\psi_\alpha(\mathbf{r})|^2 = -\frac{2}{\pi}\int^{E_F} \mathcal{I}m\mathcal{G}(\mathbf{r},\mathbf{r};E)dE \tag{3.13}$$

where the sum is over all occupied states E_α up to the Fermi Energy E_F. Similarly from (3.11) integrating directly over the space coordinate $\mathbf{r}$, we get the density of states (DOS) at the energy E as

$$n(E) = -\frac{2}{\pi}\mathcal{I}m\int \mathcal{G}(\mathbf{r},\mathbf{r};E)d\mathbf{r} \tag{3.14}$$

It is worth here to comment on how, in practice, the integral over the energies in (3.13) will be carried out. Separating the integration over the core and the valence states via a conveniently chosen energy E_b (where the letter b stays for *bottom* of the valence band)

$$\int_{-\infty}^{E_F} = \int_{-\infty}^{E_b} + \int_{E_b}^{E_F} , \tag{3.15}$$

we take advantage on the analyticity of the Green's functions $\mathcal{G}(\mathbf{r},\mathbf{r};z)$ in their prolongation in the complex energy plane, i.e. $z = E + i\delta$. In practical calculations we will consider an energy contour starting at E_b below the valence band on the real axis, that extends into the complex plane (typically following a semicircle or a rectangle) and ending at the Fermi energy on the real axis.

As explained in [ZDD82, WLZD95] the introduction of a complex energy coincides with an additional weighting factor inside the integral of the form of a Lorentzian with a FWHM equal to 2δ centered around the real energy E. This "smearing" results in a much less structured Green's function in the complex plane;

in order to carry out the integral over a complex contour starting from E_B and ending at E_F, very few points (typically around $\simeq 30$) are needed in comparison to the number of real energy points required if the integration is carried out along the real axis (even up to 1000).

Another important point is that the Green's function reflects the symmetry of the Hamiltonian $\hat{H}$. For instance, if the Hamiltonian is symmetric

$$\hat{H}^T = \hat{H} \quad \text{and} \quad \hat{H}(\mathbf{r},\mathbf{r}') = \hat{H}(\mathbf{r}',\mathbf{r}) \ ,$$

which is always the case for a local potential $V(\mathbf{r},\mathbf{r}') = V(\mathbf{r})\delta(\mathbf{r}-\mathbf{r}')$, also the Green's function is symmetric

$$\mathcal{G}(\mathbf{r},\mathbf{r}';z) = \mathcal{G}(\mathbf{r}',\mathbf{r};z) \ , \tag{3.16}$$

On the other hand if the Hamiltonian, the potential $V(\mathbf{r})$ respectively, is real we obtain for the Green's function

$$\mathcal{G}^*(\mathbf{r},\mathbf{r}';z) = \mathcal{G}(\mathbf{r},\mathbf{r}';z^*) \ . \tag{3.17}$$

Moreover in the systems which we will be interested in, additional symmetries are present in the real space, like point symmetries, which take into account the invariance of the system under point group rotations.

3.2 Scattering from a single potential

In the previous section we learned how to construct the Green's function $\hat{\mathcal{G}}$ associated to a system with Hamiltonian of the type $\hat{H} = \hat{H}_0 + \hat{V}$. We didn't specify the form of the potential $\hat{V}$, but simply considered it as a perturbation to a "reference system" with Hamiltonian $\hat{H}_0$, which can be the free-space or more generally a system tuned to fulfill some special requirements. In this section, I will describe the solution of the Schrödinger equation in the presence of a single spherically symmetric local potential $V = V(r)$, and in the next section the case of multiple scatteres, for instance a crystal, will be discussed.

Let us considered the case of a Muffin-Tin potential defined as

$$V(r) = \begin{cases} \neq 0 \ , \text{ if } r < r_{MT} \\ = 0 \ , \text{ if } r > r_{MT} \end{cases} \ , \tag{3.18}$$

where r_{MT} is the Muffin-Tin radius, the meaning of which will be given in the next section; for the moment it is just a radius out of which the potential $V(r)$ is zero.

If we introduce spherical polar coordinates (θ, ϕ, r), the radial Schrödinger equation assumes the form

$$[-\frac{\partial}{\partial r^2} + \frac{l(l+1)}{r^2} + V(r) - E]rF_l(r;E) = 0 \ , \tag{3.19}$$

where we separated the radial and angular part of the wave functions as

$$\psi(\mathbf{r}, E) = F_l(r, E)Y_{lm}(\theta, \phi) \ , \tag{3.20}$$

where $Y_{lm}(\theta, \phi) = Y_L(\hat{\mathbf{r}})$ are the spherical harmonics, and L stands for $L \equiv (l, m)$. For each E and l, two solutions exist for Eq. (3.19), the regular or physical solution, behaving as r^l for $r \to 0$, and the irregular solution, called in this way because it diverges near the origin as $\frac{1}{r^{l+1}}$.

Let us suppose that the reference system is the free-space; in this case the solution of the unperturbed Schrödinger equation can be described as a plane wave,

$$\psi(\mathbf{r}) = \exp(i\mathbf{k} \cdot \mathbf{r}) \ . \tag{3.21}$$

which can also be expanded into spherical harmonics,

$$\exp(i\mathbf{k} \cdot \mathbf{r}) = 4\pi \sum_L i^l j_l(\sqrt{E}r)Y_L(\hat{\mathbf{k}})Y_L(\hat{\mathbf{r}}) \ . \tag{3.22}$$

where $j_l(\sqrt{E}r)$ is the Bessel function, which is the regular solution of the free-particle system. Inserting (3.22) in (3.11), we obtain for the free-particle Green's function, after some straightforward calculations,

$$\begin{aligned} g(\mathbf{r}, \mathbf{r}'; E) &= -\frac{1}{4\pi} \frac{e^{i\sqrt{E}|\mathbf{r}-\mathbf{r}'|}}{|\mathbf{r}-\mathbf{r}'|} = \sum_L Y_L(\hat{\mathbf{r}}) g_l(r, r'; E) Y_L(\hat{\mathbf{r}}') \ , \\ \text{with } g_l(r, r'; E) &= \sqrt{E} j_l(\sqrt{E}r_<) h_l(\sqrt{E}r_>) \ . \end{aligned} \tag{3.23}$$

where $r_< := \min\{r, r'\}$, $r_> := \max\{r, r'\}$, and $h_l = n_l - ij_l$ is the Hankel function and n_l the Neumann function (irregular solution of the free-particle system).

The regular solution $R_L(\mathbf{r}, E) = R_l(r, E)Y_L(\hat{\mathbf{r}})$ of Eq. (3.19) is given by the Lippmann-Schwinger equation, which due to the spherical simemtry of the potential $V(r)$ reduces to

$$R_l(r, E) = j_l(\sqrt{E}r) + \int_0^{r_{MT}} g(r, r'; E)V(r')R_l(r', E)r'^2 dr' \ , \tag{3.24}$$

which describes the scattering of the "free" incoming wave $j_l(\sqrt{E}r)$ by the potential $V(r)$. Let us consider first the solution outside the Muffin-Tin radius; in this case

we have $r > r_{MT}$ and, looking at the integral over r' in (3.24), also the relation $0 < r' < r_{MT}$; these two conditions mean that $r_< = r'$ and $r_> = r$. The quantity $h_l(\sqrt{E}r)$ can then be taken out from the integral over the variable r'. For $r > r_{MT}$ the regular solution $R_l(r, E)$ becomes

$$R_l(r, E) = j_l(\sqrt{E}r) + \sqrt{E}t_l(E)h_l(E) \ , \tag{3.25}$$

where we defined the *scattering matrix* (or simply t-matrix) $t_l(E)$ as

$$t_l(E) = \int_0^{r_{MT}} r'^2 j_l(\sqrt{E}r')V(r')R_l(r', E)dr' \ . \tag{3.26}$$

The t-matrix contains all the information of the scattering, and represents the transition-operator between the free, incoming wave $j_l(\sqrt{E}r)$ and the scattered wave $R_l(r, E)$ in the presence of the potential $V(r)$. Since $j_l(\sqrt{E}r) \sim r^l$ for $r \to 0$, we obtain from eq. (3.24) and (3.23) in the limit of $r \to 0$

$$R_l(r, E) \cong j_l(\sqrt{E}r)\alpha_l(E) \ , \tag{3.27}$$

where we have defined the α-factors as

$$\alpha_l(E) = 1 + \sqrt{E}\int_0^{r_{MT}} r'^2 h_l(\sqrt{E}r')V(r')R_l(r', E)dr' \ , \tag{3.28}$$

which represent the enhancement of the regular solution $R_l(r, E)$ over the free particle solution j_l around the origin.

Similar to Eq. (3.24), the Lippmann-Schwinger equation for the irregular solution $H_L(\mathbf{r}, E) = H_l(r, E)Y_L(\hat{\mathbf{r}})$ holds, i.e.

$$H_l(r, E) \ = \ \tilde{H}_l(r, E) + \int_0^{r_{MT}} g(r, r'; E)V(r')H_l(r', E)r'^2 dr' \ . \tag{3.29}$$

Yet for the spherical irregular solution $H_L(\mathbf{r}, E)$ another boundary condition holds; outside the Muffin-Tin sphere the wave function it has to behave like an unperturbed outgoing way, given by the Hankel function

$$H_l(r, E) = h_l(\sqrt{E}r), \quad r > r_{MT} \ . \tag{3.30}$$

We can then, by using the Lippmann-Schwinger equation (3.22), deduce an expression for the irregular solution $\tilde{H}_L(\mathbf{r}, E)$, in the limit of $r \to 0$

$$\tilde{H}_L(\mathbf{r}, E) = h_l(\sqrt{(E)}r)\left[1 - \sqrt{E}\int_0^{r_{MT}} r^2 j_l(\sqrt{E}r)V(r)H_l(r, E)dr\right] \ . \tag{3.31}$$

Thus near the origin the behaviour of $H_l(r,E)$ is the same as the one of the Hankel function, and diverges as $\frac{1}{r^{l+1}}$; the relation between the two, is then given by

$$H_l(r,E) \cong h_l(\sqrt{E}r)\frac{1}{\alpha_l(E)} \ , \tag{3.32}$$

where the α-factors are the same as in (3.28) [MMZ87]. For the "perturbed" Green's function, we can finally give an expansion over regular and irregular solutions similar to the expansion for the free-particle Green's function (3.23),

$$\begin{aligned} G(\mathbf{r},\mathbf{r}';E) &= \sum_L Y_L(\hat{\mathbf{r}})G_l(r,r';E)Y_L(\hat{\mathbf{r}}') \ , \\ \text{with } G_l(r,r';E) &= \sqrt{E}R_l(r_<,E)H_l(r_>,E) \ . \end{aligned} \tag{3.33}$$

The regular and irregular solutions have to fulfill the Wronski-relation [Dri91],

$$[H_l(r;E),R_l(r;E)] = (\partial_r H_l(r;E))R_l(r;E) - (\partial_r R_l(r;E))H_l(r;E) = \frac{1}{r^2\sqrt{E}} \tag{3.34}$$

3.3 Multiple scattering theory

The goal of this section is to explain how the influence of an arbitrary system of scatterers can be calculated, taking into account the results obtained in section 3.2, for a single scattering potential. For an example, in Fig. 3.1 we show a special case of multiple scatterers, namely a crystal which consists of an ordered array of potentials, where $\mathbf{R}^n$ are the lattice vectors.

We consider here an arbitrary arrangement of non-overlapping muffin-tin potentials centered at positions $\mathbf{R}^n$,

$$V(\mathbf{r}) = \begin{cases} \sum_n V^n(|\mathbf{r}-\mathbf{R}^n|), & \text{if } |\mathbf{r}-\mathbf{R}^n| \le r_{MT} \\ 0, & \text{otherwise} \end{cases} \tag{3.35}$$

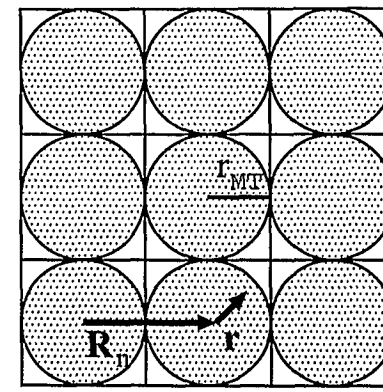

Figure 3.1: Example of multiple scatteres: a crystal

The following considerations are also true for a constant potential in the interstitial region, since the energy zero level can be adjusted in order to set as new energy zero the value in the interstitial region.

Another possible approximation for the potentials (which is the one used in this work) is the Atomic Sphere Approximation (ASA); it consists in choosing the radius,

inside which the potential is spherical and $\neq 0$, in such way that the volume of the sphere associated to it is equal to the volume of the Wigner-Seitz cell; this radius is called Wigner-Seitz radius, and denoted by r_{WS}. The spheres are, in this way, slightly overlapping; this gives a better treatment of the interstitial region, which is important for a correct treatment of surfaces or impurities in the bulk or at surfaces [Lan96, NWZD98, MSN+98].

If we move to a cell-centered coordinates system via the transformation

$$\mathbf{r} \longrightarrow \mathbf{r} + \mathbf{R}^n \ ; \ \mathbf{r}' \longrightarrow \mathbf{r}' + \mathbf{R}^{n'} \ , \tag{3.36}$$

where $\mathbf{R}^n$ and $\mathbf{R}^{n'}$ are the coordinates of the atoms n and n', the Schrödinger equation (3.6), which defines the Green's function, becomes

$$(-\nabla^2 + V^n(r) - E)\mathcal{G}(\mathbf{r} + \mathbf{R}^n, \mathbf{r}' + \mathbf{R}^{n'}; E) = -\delta_{nn'}\delta(\mathbf{r} - \mathbf{r}') \ . \tag{3.37}$$

In constructing the solution of this equation, we first split off the solution for the single potential $V^{n'}$ in free space, being according to (3.33) given by

$$\mathcal{G}_s^n(\mathbf{r} + \mathbf{R}^n, \mathbf{r}' + \mathbf{R}^n; E) = \delta_{n,n'}\sqrt{E}\sum_L H_L^n(\mathbf{r}_>; E)R_L^n(\mathbf{r}_<; E) \ , \tag{3.38}$$

which takes into account the source condition in eq. (3.37). Therefore the remaining term is a solution of the homogeneous Schrödinger equation, i.e. without any source term in total space, and therefore can be expanded in each cell n as a function of $\mathbf{r}$ into regular solutions R_L. Due to the symmetry of $\mathcal{G}(\mathbf{r}, \mathbf{r}') = \mathcal{G}(\mathbf{r}', \mathbf{r})$, the same can be done for the dependence on the variable $\mathbf{r}'$, so that we obtain the following general result:

$$\begin{aligned}\mathcal{G}(\mathbf{r} + \mathbf{R}^n, \mathbf{r}' + \mathbf{R}^{n'}; E) &= \delta_{nn'}\mathcal{G}_s^n(\mathbf{r} + \mathbf{R}^n, \mathbf{r}' + \mathbf{R}^n; E) \\ &+ \sum_{LL'} R_L^n(\mathbf{r}; E)\mathrm{G}_{LL'}^{nn'}(E)R_{L'}^{n'}(\mathbf{r}'; E) \ ,\end{aligned} \tag{3.39}$$

The second, the *back scattering* term, contains all the multiple-scattering processes acting on an electron under the influence of all the potentials $V^{n'}(r)$.

It is through the Eq. (3.39) that we can appreciate one of the main characteristic of the KKR approach. The information on the geometrical ordering of the atoms is separated from the information on the single scattering process; the Green's function turns out to be a sum of a "single scattering" part and a "structural" part. The expansion coefficients $\mathrm{G}_{LL'}^{nn'}$, that have still to be determined, are indeed called *structural Green's function matrices.*

In order to determine these structural matrices, the crystal with potential $V(\mathbf{r})$, as we saw in section 3.1, is then considered as perturbation to an appropriately choosen reference system. If we indicate with $\mathcal{G}$ and $\mathcal{G}_0$ the correspondent Green's functions, we can expand both systems as in (3.39); inserting these two expansions into the Lippman-Schwinger equation (3.7), and replacing V with $\Delta V = (V - V_0)$, we obtain after some algebraic operations, the following *algebraic* Dyson equation

$$\mathrm{G}^{nn'}_{LL'} = \mathrm{G}^{nn'}_{0\,LL'} + \sum_{n'',L''} \mathrm{G}^{nn''}_{0\,LL''} \Delta t^{n''}_{l''}(E) \mathrm{G}^{n''n'}_{L''L'} \ , \qquad (3.40)$$
$$\text{with} \quad \Delta t^n_l(E) = t^n_l(E) - t^n_{0\,l}(E) \ ,$$

which relates the structural Green's functions of the real and the reference systems. In practice, in order to calculate the "perturbed" Green's function $\hat{G}$, we will follow these steps:

- At first, we have to calculate the t-matrix $t^n_{0\,l}(E)$ and the structural Green's functions $\mathrm{G}^{nn'}_{0\,LL'}$ of the reference system.

- Secondly the "perturbed system" t-matrix $t^n_l(E)$, together with the regular $R^n_L(\mathbf{r}_<; E)$ and irregular $H^n_L(\mathbf{r}_>; E)$ solutions, have to be calculated.

- Using (3.40), the structural Green's function of the perturbed system $\mathrm{G}^{nn'}_{LL'}$ can then be calculated.

- Then we have to insert $\mathrm{G}^{nn'}_{LL'}$ in the expansion on the regular solutions in (3.39) and then add the single-site term G^n_s from the Eq. (3.38) to obtain the full Green's function $\mathcal{G}(\mathbf{r}, \mathbf{r}'; E)$

3.4 The full-potential approach

It is worth now to spend a few words on the *full potential* treatment [DDZ92, PZDS97, Set99], as opposed to ASA, of an array of crystal potentials. If we suppose to take into account the full anisotropic Wigner-Seitz cell around each potential, we can divide the space in non-overlapping space-filling volumes; due to this anisotropy of both the potentials in each cell and the faceted form of the cells, the angular momentum is not conserved anymore, and it is necessary include possible $L \longrightarrow L'$ transitions in the solution of the Schrödinger equation.

The potentials, and consequently the regular and irregular solutions have then to be expanded over the spherical harmonics; for instance for the potential it holds

$$V^n(\mathbf{r}) = \sum_L V_L^n(r) Y_L(\hat{\mathbf{r}}) \ . \tag{3.41}$$

and for the regular solution $R_L^n(\mathbf{r}, E)$ the following expansion is valid

$$R_L^n(\mathbf{r}, E) = \sum_{L'} R_{L'L}^n(r, E) Y_{L'}(\hat{\mathbf{r}}) \tag{3.42}$$

Here the L index denotes the angular momentum of the incoming spherical waves and the L' index the angular momenta induced by the anisotropy of the potential. Each of the Eq. (3.24) and Eq. (3.29) becomes a system of coupled equation in the angular momentum. They can be solved, introducing a Lippmann-Schwinger equation between the spherical and non-spherical part of the solutions; it is possible to solve them with an iterative procedure by a Born expansion series with respect to the anisotropic part of the potential, as explained by Drittler [Dri91], where it is usually sufficient to stop at the second order Born approximation to obtain good results. The solution of the radial equation will be carried out modelling the non-spherical parts of the cell by using the shape functions technique [SAZ90].

The dependence over two different angular momentums L and L', appears also in the t-matrix, i.e. $t^n(E) = t_{LL'}^n(E)$, while for the ASA case the t-matrix turned out to be diagonal in L and L'. In the algebraic Dyson equation (3.40) the sum runs then over two angular momentum indices, as

$$\mathrm{G}_{LL'}^{nn'} = \mathrm{G}_{0\,LL'}^{nn'} + \sum_{n'',L''L'''} \mathrm{G}_{0\,LL''}^{nn''} \Delta t_{L''L'''}^{n''}(E) \mathrm{G}_{L'''L'}^{n''n'} \ , \tag{3.43}$$

$$\text{with} \quad \Delta t_{LL'}^n(E) = t_{LL'}^n(E) - t_{0\,LL'}^n(E) \ ,$$

This FP (Full-Potential) treatment obviously requires more computational effort, for instance in the solution of the coupled radial equation, but doesn't increase the efforts for solving the Dyson equation (3.43). Therefore the additional effort for the full potential treatment scales only linearly with the number of atoms. The better treatment of the interstitial space between atoms, on the other hand, has shown in the past to improve sensibly the treatment of hyperfine fields and electric field gradients [Set99], and allowed to calculate forces and relaxations in the system [PZDS97, Set99].

To obtain most of the results presented in chapters 5, 6 and 7, the ASA approximation was used; full-potential calculations were performed now and then to test the validity of the ASA approach, especially for the Cd-probe atoms calculation presented in chapter 5.

Chapter 4

Screened KKR method

In the electronic structure calculations the use of tight-binding methods with short-ranged hopping parameters has many advantages. For instance most of our understanding on transition metals and other localized systems comes from a tight-binding picture of localized orbitals with small overlap between nearest-neighboring sites. Moreover tight-binding methods are from the numerical point of view very favorable, since the short range of the coupling enormously simplifies the complexity and the numerical effort of the calculations and permits to tackle problems, the solution of which is otherwise not attainable.

Therefore many attempts have been made in order to combine the simplicity of the tight-binding approaches with the accuracy and precision of the *ab-initio* methods. One of the most successful attempt was performed by Andersen *et al.* [AJ84, APJ86], presenting a tight-binding (TB) version of the Linear-Muffin-Tin-Orbital (LMTO) method. In the context of the KKR method, localized tight-binding parameters can be achieved by benefitting from the freedom left in choice of the reference system [ZDÚ+95]. A first "screened" version of the KKR method has been proposed by Andersen [APS92] and later simplified by L. Szunyogh *et al.* [SÚWK94], but the procedure adopted to build the desired "screening" was rather complicated and with an *ad-hoc* character.

In this chapter, I will discuss a recently introduced more efficient formulation of "*screened*" KKR Green's Function (SKKR-GF) method. It is possible, by an appropriate choice of the reference system, to introduce an exact transformation which leads to exponentially decaying structure constants as a function of the distance $|\mathbf{R}_n - \mathbf{R}_{n'}|$ [Zel97, Wil97, WZD97]. The range of the Green's function is then restricted to a limited region of space around each atomic site, and in some cases, in particular for "2-dimensional" layered systems, it is possible to introduce a numeri-

cal algorithm for the solution of the algebraic Dyson equation, which scales linearly with the number N of non-equivalent atoms (where N, in the case of 2D systems, is the number of layers in the system).

In the case, as presented in chapter 6, of high-Miller-index surfaces (vicinal surfaces), the spacing between layers is very much reduced in comparison with low-index surfaces; this implies that more atoms (layers) are needed in the calculation if a thick slab of material has to be considered. Similarly for interfaces, the decreased periodicity in the plane leads to a large number of atoms that have to be considered in the self-consistence procedure. The "traditional" KKR approach , successfully applied for the study of impurities in bulk [ZD79, PZD80, BAZD87, DWZD89] or at surfaces [WSL$^+$95, SHW$^+$96, LSW$^+$94, NWZ$^+$98, MSN$^+$98], or to the study of surfaces and interfaces [WZD$^+$98, ZLDD92, Lan96] cannot by applied for large systems with many atoms since the numerical effort scales with the third power N^3 of the number of non-equivalent atoms.

Several tests [Wil97, Zel97] have shown that the SKKR method is a precise and reliable method for the study of the electronic and magnetic properties of large systems, joining a easier and faster approach for the calculation of the structure constants together with the preservation of the numerical precision typical of traditional KKR methods. At the end of this chapter I will present some additional tests for the calculation of surface energies.

4.1 Problems of the traditional KKR method

The calculation of the perturbed Green's function of a crystal, as we saw in the previous chapter, consists in two different steps: the calculation of the regular $R_l(r;E)$ and irregular solutions $H_l(r;E)$ of the radial Schrödinger equation, together with the t-matrices $t_l(E)$, and the calculation of the structural Green's function $\mathrm{G}^{nn'}_{LL'}$, which is related to the reference structural Green's functions $\mathrm{G}^{nn'}_{0\,LL'}$ by the Dyson equation (3.43). In the traditional KKR approach, the reference system is chosen to be the free-space. This seems to be a good choice, since the free-space regular and irregular radial solutions are known analytically (Bessel and Neumann functions). Thus the Green's function for free space is given by

$$\begin{aligned}\mathcal{G}_0(\mathbf{r}+\mathbf{R}^n,\mathbf{r}'+\mathbf{R}^{n'};E) &= \delta_{nn'}\mathcal{G}^n_{0\,s}(\mathbf{r}+\mathbf{R}^n,\mathbf{r}'+\mathbf{R}^n;E)\\ &+\sum_{LL'} Y_L(\hat{\mathbf{r}};E)j_l(r;E)\mathrm{G}^{nn'}_{0\,LL'}(E)j_{l'}(r';E)Y_{L'}(\hat{\mathbf{r}}';E)\ , \end{aligned} \tag{4.1}$$

where $\mathcal{G}_{0\,s}$ is the single site solution given by Eq. (3.25)

The structure constants for $n \neq n'$ can be calculated from the solution (3.23) by means of the addition theorem [MMZ87]. One obtains

$$\mathrm{G}_{0\,LL'}^{nn'}(E) = 4\pi\sqrt{E}\sum_{L''} i^{l-l'+l''} C_{LL'L''} h_{l''}(\sqrt{E}|\mathbf{R}^n - \mathbf{R}^{n'}|) Y_{L''}(|\mathbf{R}^n - \mathbf{R}^{n'}|) \qquad (4.2)$$

while the diagonal elements $\mathrm{G}_{0\,LL'}^{nn}$ vanish. Here the Gaunt's coefficients $C_{LL'L''}$ are defined as

$$C_{LL'L''} = \int Y_L(\hat{\mathbf{r}}) Y_{L'}(\hat{\mathbf{r}}) Y_{L'}(\hat{\mathbf{r}}) d\hat{\mathbf{r}}$$

where the integral is over the solid angle $d\hat{\mathbf{r}}$. For the case of a finite perturbation in real space, e.g. a cluster or molecule, the Dyson Eq. (3.43) can be solved in the real space by inverting the matrix $1 - \hat{\mathcal{G}}_0\hat{t}$; in the case of an infinite bulk crystal one can make use of the translation symmetry and solve the equation in the reciprocal space. Thus we Fourier transform Eq. (3.43), which, by introducing the Fourier-transformed structural Green's functions, the so called KKR structure constants,

$$\mathrm{G}_{0\,LL'}(\mathbf{k}; E) = \sum_n \exp[i\mathbf{k}(\mathbf{R}^n - \mathbf{R}^{n'})] \mathrm{G}_{0\,LL'}^{nn'}(E) \ , \qquad (4.3)$$

$$\mathrm{G}_{LL'}(\mathbf{k}; E) = \sum_n \exp[i\mathbf{k}(\mathbf{R}^n - \mathbf{R}^{n'})] \mathrm{G}_{LL'}^{nn'}(E) \ . \qquad (4.4)$$

transforms into the wave-vector dependent Dyson equation,

$$\mathrm{G}_{LL'}(\mathbf{k}; E) = \mathrm{G}_{0\,LL'}(\mathbf{k}; E) + \sum_{L''L'''} \mathrm{G}_{0\,LL''}(\mathbf{k}; E) t_{L''L'''}(E) \mathrm{G}_{L'''L'}(\mathbf{k}; E) \qquad (4.5)$$

One problem in the choice of the free-space as the reference system lies on the calculation of the KKR structure constants $\mathrm{G}_{0\,LL'}(\mathbf{k}; E)$. Since the $\mathrm{G}_{0\,LL'}^{nn'}(E)$ are long-ranged and vary oscillatory with the distance $|\mathbf{R}^n - \mathbf{R}^{n'}|$, the sum over n in Eq. (4.3) is poorly converging. In practical application this problem can only be overcome by using Ewald's summation technique [Ebe, MJW71, Set96] which is rather time consuming.

A second problem appears when we try to solve Eq. (4.5) in the case of layered systems. For these "planar systems" only the 2-dimensional periodicity in the "layer" plane can be conserved, while the periodicity perpendicular to this plane is in general broken (see Sec. 4.4). Therefore only a two-dimensional Fourier transform can be carried out for atoms in the same plane, and "layer" indices will remain explicit in Eq. (4.5). The order of the determinant associated to the system, will be proportional to the number N of layers in the system. In the same time the long range interaction of the free-space leads to a long-ranged structural matrix G_0;

this means that the full-inversion of the determinant is the only possible algorithm, resulting in a N^3-scaling behavior. In contrast to these unpleasant characteristics for the free-space reference system, we will propose in the following section an alternative reference system, which allows a much easier calculation of the corresponding structure constants and moreover allows for planar systems the use of N-scaling algorithms for the solution of the Dyson equation.

4.2 The "screened" reference system

Before illustrating the particular choice of the reference system in order to transform the traditional KKR method in a "screened" one, let us summarize the relations that hold between the real system, the free space, and a new arbitrary reference system. Working for simplicity in the operator notation, i.e. $\hat{G} = \{\mathrm{G}_{LL'}^{nn'}(E)\}$, $\hat{G}_0 = \{\mathrm{G}_{0\,LL'}^{nn'}(E)\}$ and $\hat{t} = \{t_l^n(E)\delta_{nn'}\}$, we can rewrite the algebraic Dyson equation 3.43 as

$$\begin{aligned} \hat{G} &= \hat{G}_0 + \hat{G}_0\hat{t}\hat{G} && (4.6)\\ &= \hat{G}_0 + \hat{G}_0\hat{t}\hat{G}_0 + \hat{G}_0\hat{t}\hat{G}_0\hat{t}\hat{G}_0 + \cdots \\ &= \hat{G}_0(\hat{I} - \hat{t}\hat{G}_0)^{-1} && (4.7) \end{aligned}$$

where $\hat{I}$ stands for the identity-operator. We introduce now the scattering-path operator $\hat{\tau} = \{\tau_{LL'}^{nn'}(E)\}$ [MMZ87] defined as

$$\hat{\tau} = (\hat{t}^{-1} - \hat{G}_0)^{-1} \tag{4.8}$$

Between the scattering-path operator $\hat{\tau}$ and the perturbed structural Green's function the following relation holds

$$\hat{G} = \hat{G}_0 + \hat{G}_0\hat{\tau}\hat{G}_0$$

or similarly

$$\hat{G} = \hat{t}^{-1}\hat{\tau}\hat{t}^{-1} - \hat{t}^{-1} \tag{4.9}$$

Let us now introduce a *new reference system* which from now on will be indexed with the letter "r". Between this new reference system and the free-space a Dyson equation similar to the (4.6) holds,

$$\hat{G}^r = \hat{G}_0 + \hat{G}_0\hat{t}^r\hat{G}^r \tag{4.10}$$

where $\hat{G}^r = \{G^{r\,nn'}_{LL'}(E)\}$ and $\hat{t}^r = \{t^{r\,n}_l(E)\delta_{nn'}\}$ are respectively the structure constants and the t-matrix of the new reference system. The "perturbed" system can be related to this new reference system by a similar equation;

$$\hat{G} = \hat{G}^r + \hat{G}^r \Delta\hat{t}\hat{G} \tag{4.11}$$

where $\Delta\hat{t} = \hat{t} - \hat{t}^r$. Now a new scattering-path operator related to the perturbation $\Delta\hat{t}$ can be introduced,

$$\hat{\tau}_\Delta = [(\Delta\hat{t})^{-1} - \hat{G}^r]^{-1} \tag{4.12}$$

which has to fulfill the following relations

$$\hat{G} = \hat{G}^r + \hat{G}^r\hat{\tau}_\Delta\hat{G}^r \tag{4.13}$$

$$= (\Delta\hat{t})^{-1}\hat{\tau}_\Delta(\Delta\hat{t})^{-1} - (\Delta\hat{t})^{-1} \tag{4.14}$$

All the transformations presented above are exact: thus the solution of Eq. (4.6) gives equivalent results to the solution of the two Dyson equations (4.10) and (4.11). The choice of the reference system becomes thus arbitrary, provided that its structural Greens' functions are known; if they are not known analytically, Eq. (4.10) has then to be solved numerically.

It is time now to introduce the choice of this reference system which can optimally "screen" the structure constants. The basic idea is the following; the structure constants for the free-particles system $G^{nn'}_{0\,LL'}(E)$, decay exponentially with the distance $|\mathbf{R}^n - \mathbf{R}^{n'}|$ for negative energy values, i.e. $E < 0$. The reason for that can be traced back to the absence of eigensolutions of the Schrödinger equation which have negative energy eigenvalues. If we find a reference system, which can be also unphysical, which has no solutions in the energy range relevant for electronic structure calculations, we obtain the desired "screening". Normally the occupied states of the Schrödinger equation exist up to around $1Ry$ above the energy zero of the system; it will be then sufficient to "clean" the new reference system from eigensolutions up to this energy. Between all

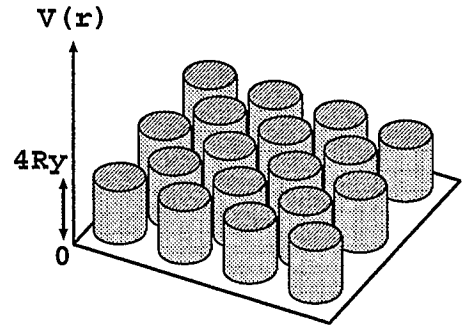

Figure 4.1: Schematic representation in 2D of repulsive $4Ry$-high muffin-tin potentials

the possible reference systems fulfilling this requirement, R. Zeller *et al* [ZDÚ+95] considered a particularly simple one, i.e. an ordered array of *repulsive spherical potential wells* V^r (as sketched in Fig. 4.1 for the case of $4Ry$ high potentials). The reference potentials retain the same crystal structure of the real system we want to study. The radius inside which the repulsive potential are constant and $\neq 0$, can be the muffin-tin radius r_{MT} or the Wigner-Seitz radius r_{WS} introduced in section 3.3; in the first case we call the potentials V^r muffin-tin wells, while for the second we denote them as ASA wells. Several tests have been carried out [Wil97, Zel] to check the differences induced in real system calculations (for bulk Cu and the (001) Cu surface) by the choice of MT wells as opposed to ASA wells; the conclusion is that the muffin-tin description of the repulsive potentials generally leads to better results than the ASA description (probably due to the overlap between the ASA repulsive potentials). Consequently muffin-tin wells have been choosen as the reference system for all the results presented in this work. The structure constants for this repulsive reference system are indeed screened and decay exponentially with distance.

In order to answer the question, how fast these structure constants decay in real space, we rewrite Eq. (4.10,) with all indices:

$$\mathrm{G}^{r\,nn'}_{LL'}(E) = \mathrm{G}^{nn'}_{0\,LL'}(E) + \sum_{n''L''} \mathrm{G}^{nn'}_{0\,LL'}(E) \cdot t^{r\,n''}_{l''}(E) \cdot \mathrm{G}^{r\,n''n'}_{L''L'}(E) \qquad (4.15)$$

In principle, the solution of the above equation involves the inversion of an infinite matrix, where n and n' span all over the space. Alternatively, as discussed in section 4.1, we can use the periodicity of the system, and Fourier transform the Dyson equation, thus solving it in the reciprocal space. If the structure constants decay fast enough as a function of the distance $|\mathbf{R}_n - \mathbf{R}_{n'}|$, as sketched in Fig. (4.3), we can solve Eq. (4.15) taking into account the back-scattering processes inside a small finite cluster of atomic sites (called Tight-Binding cluster). We include here the results obtained by R. Zeller [ZDÚ+95], and present in Fig. (4.2) a comparison between

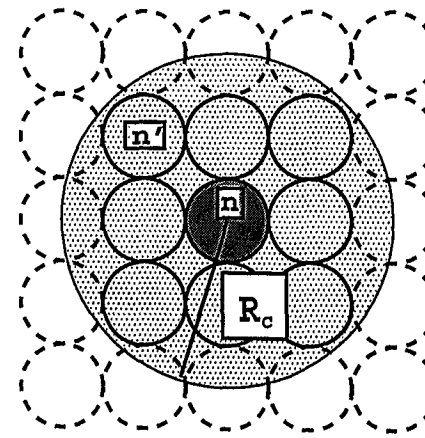

Figure 4.2: Cluster of sites in real space delimited by the cut-off radius R_c

the structural Green's functions of the free-space and the one for the "screened" reference system; the geometry choosen for the tests was an *fcc* lattice with lattice constant of $a_0 = 6.76$ (which is the lattice structure used normally for a Cu bulk calculation). In order to show the decay in space of the quantities $G^{nn'}_{LL'}(E)$ and $G^{nn'}_{LL'}(E)$, it's necessary to introduce partial norms, $N_{ll'}$, defined as

$$N_{ll'}(|\mathbf{R}_n - \mathbf{R}_{n'}|; E) = \frac{|E|^{(l+l')/2}}{(2l+1)!!(2l'+1)!!} \left[\sum_{mm'} |G^{r\,nn'}_{lm,l'm'}(E)|^2 \right]^{\frac{1}{2}} \tag{4.16}$$

with $(2l+1)!! = (2l+1)(2l-1)\cdots(3)(1)$.

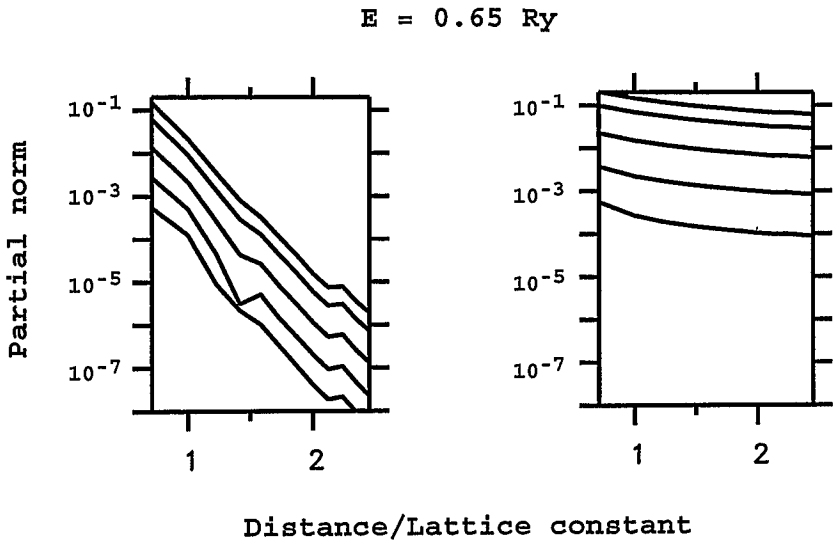

Figure 4.3: Screened (left) and free-space (right) structure partial norms for the structure constants in function of the distance $|\mathbf{R}^n - \mathbf{R}^{n'}|$; a cluster of 225 potentials of $2Ry$ height has been used and the partial norms for $l = 0, 1, 2, 3$ and 4 are shown [ZDÚ+95], for the energy value $E = 0.65Ry$

From Fig.(4.3), the essentially exponential decay of the structure constants of the system of repulsive muffin-tin potentials is evident, as well as the very slow decay of the free-space structure constants. In the distance range in Fig. (4.2), the screened structure constants decrease to about 10^{-5} of their nearest-neighbor values, while the free space structure constants decrease, in the same energy range, by less than a factor of 10.

Additional tests [Wil97, Zah98] have shown that playing with the height of the repulsive potentials, we can increase ulteriorly the energy window for which no eigensolutions for the Schrödinger equations associated with the repulsive potentials

reference system are found. Repulsive potentials up to $8Ry$ have been used, and an eigenvalue-free region of up to $E_{bot} = 3Ry$ is obtained. Thus good screening can be achieved not just for occupied, but also for unoccupied states provided that their energy is not too high.

The screened structure constants can thus be neglected already after few shells. Normally for e.g. Cu or Ni it is sufficient to consider the coupling up to the 2nd shell; an exception is for instance Fe, where in order to describe the long range magnetic interactions shells up to the 5th have to be considered in the TB-cluster. Some tests on the importance of the size of the cluster used to calculate the screened structure constants can be found in the Ph.D. thesis of K. Wildberger [Wil97] and in the work of R. Zeller [Zel97].

4.3 Dyson equation for the real system

We tackle now the problem of the solution of the Dyson equation (3.43) which connects the "perturbed" (or real system) structure constants with the one of the reference system. For a periodic arrangement of perturbations, Eq. (3.43), contrary to Eq. (4.15), involves an infinite sum over n, where n is the atom index spanning the whole space. To solve Eq. (3.43), as we have seen in section 4.1, we exploit the periodicity of the system and introduce Fourier transforms for the structure constants; we obtain thus the Dyson equation (4.5) which has to be solved in the reciprocal space.

The up-to-date version of the SKKR program is able to treat whatsoever 2- or 3-dimensional periodic lattices. In the case of a *bulk* crystal (see Fig. (4.4*a*)), the primitive cell which contains the basis atoms, is repeated in all 3 dimensions by lattice vector translations. For simple crystal structures (Bravais lattices) like *fcc* (face centered cubic), *bcc* (base centered cubic) or *sc* (simple cubic), the "basis" contains only one atom. In the case of complex lattices, like for instance zinc-blende, diamond or perovskite structures, the atom index is separated in a *cell* index and a *basis* index; since in the Fourier transforms (4.3) and (4.4) the sums are only over the cell periodicity, "basis" index will thus remain explicit in the Dyson equation (4.5) (for the notation used in the case of complex lattices I refer to the work of A. Settels [Set96]). More generally a "supercell" containing a certain number of atoms in the basis can be repeated in the 3 dimensions; by this type of *supercell geometry* we can simulate for instance ordered alloys or periodic multilayer systems. If the cell is repeated only in two dimensions, as in Fig. (4.4*b*), the perturbation has to

be be restricted to a *slab* of space embedded in the repulsive reference system. It is also possible to simulate the presence of semi-infinite perturbations on the sides of the slab, by the "Surface Green's Functions" [TDK+97] which will be calculated with the help of the space decimation technique [SSR85]; this space construction is in the following refered to as *half-space geometry.*

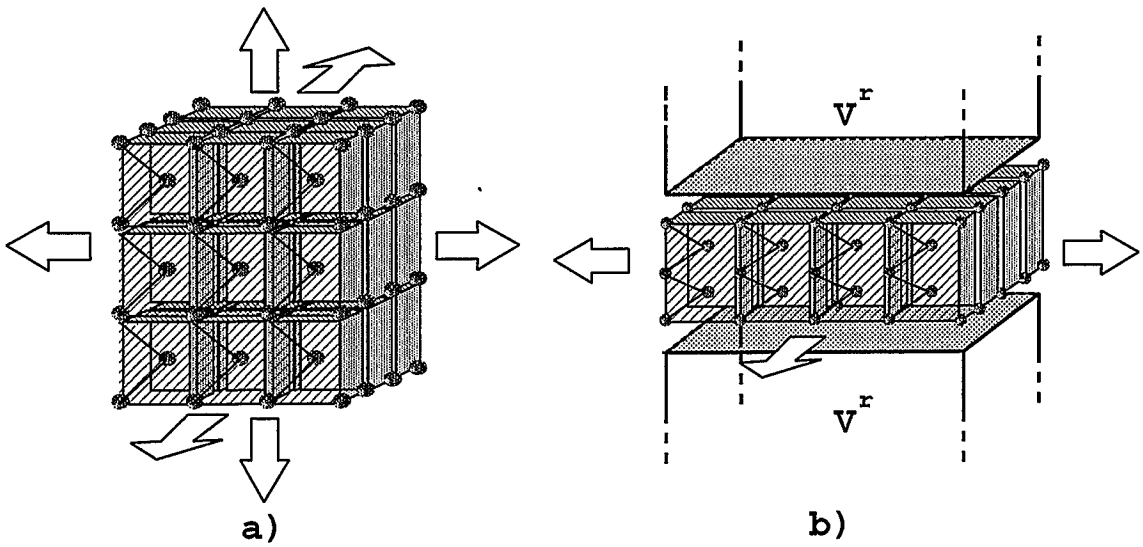

Figure 4.4: Bulk geometry, Fig. *a*, and slab geometry, Fig. *b*

In practice the calculation of 2D or 3D periodic systems differ only in the set-up of the Dyson equation (3.43) and in the calculation of the Coulomb term which together with the exchange-correlation term has to be added to the potential in Eq. (2.39). The single-site part of the calculations, i.e. the calculation of the regular and irregular solutions and of the t-matrices is, as we saw in the previous chapter, independent on the geometrical arrangement of the scatterer potentials.

Since in the next two chapters I present results for "planar defects", I will discuss in the next section the formalism adopted in order to solve Eq. (3.43) for layered systems. For bulk systems the formula are quite the same, except that everything has to be read again in a 3 dimensional notation; the layer-index becomes more generally a basis-index while the wave-vector introduced by the Fourier transform refers to the 3D instead of the 2D-Brillouin zone [Set96, Zah98]. Afterwards I describe the half-space geometry approach; for the description of the decimation technique I remand to the Ph.D. thesis of K. Wildberger [Wil97].

4.4 Layered systems and N-scaling

In this section I present the formulation for layered systems, or "planar" defects, used to simulate surfaces and interfaces. For slab calculations only the 2-Dimensional periodicity in the surface plane is retained while the periodicity perpendicular to it is broken. Moreover I limit the discussion to the case of a simple planar Bravais lattice, where all the atoms in the same plane are equivalent, and the basis atom index characterizes univocally the layers. For such a "planar" system the "screened" KKR method represents a very efficient and N-scaling (where N is the number of layers in the system) method for the solution of the Dyson equation (3.43)

In the case of a layered system (as sketched in Fig. (4.5)) the lattice vector $\mathbf{R}^n$ which characterizes the atom n, is separated in two vectors [Lan96], i.e.

$$\mathbf{R}^n = \mathbf{R}_i + \boldsymbol{\chi}_\nu \qquad (4.17)$$

where $\mathbf{R}_i$ characterize the i-th layer and $\boldsymbol{\chi}_\nu$ is the lattice vector of the two-dimensional Bravais lattice of the i-th layer; the atoms are in this way unambigously defined by the new indices $n \equiv (i, \nu)$.

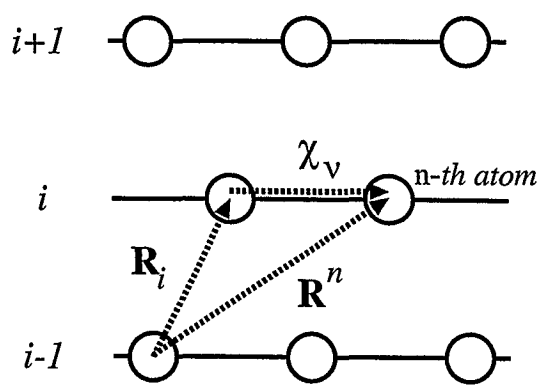

Figure 4.5: Schematic representation of a layered system

With the introduction of this notation, the Dyson equation reads

$$\mathrm{G}^{\,ii'}_{\substack{\nu\nu'\\LL'}}(E) = \mathrm{G}^{r\,ii'}_{\substack{\nu\nu'\\LL'}}(E) + \sum_{i'',\nu'',L'',L'''} \mathrm{G}^{r\,ii''}_{\substack{\nu\nu''\\LL''}}(E)\Delta t^{i''}_{L''L'''}(E)\mathrm{G}^{\,i''i'}_{\substack{\nu''\nu'\\L'''L'}}(E) \qquad (4.18)$$

where the t-matrices, due to the invariance of the system with respect to translations of a 2D lattice vector, are the same for all the atoms in the same plane. Because of this 2D-translational invariance, the structure constants will depend only on the differences between 2D lattice vectors $\boldsymbol{\chi}_\nu - \boldsymbol{\chi}_{\nu'}$,

$$\mathrm{G}^{r\,ii'}_{\substack{\nu\nu'\\LL'}}(E) = \mathrm{G}^{r\,ii'}_{\substack{\nu-\nu'\\LL'}}(E) \quad \text{and} \quad \mathrm{G}^{\,ii'}_{\substack{\nu\nu'\\LL'}}(E) = \mathrm{G}^{\,ii'}_{\substack{\nu-\nu'\\LL'}}(E)\ . \qquad (4.19)$$

Therefore we evaluate 2D Fourier transforms of the structure constants

$$\mathrm{G}^{ii'}_{LL'}(\mathbf{q}_{||}, E) = \sum_{\nu'} e^{-i\mathbf{q}_{||}\cdot(\boldsymbol{\chi}_\nu - \boldsymbol{\chi}_{\nu'})}\mathrm{G}^{\,ii'}_{\substack{\nu-\nu'\\LL'}}(E) \qquad (4.20)$$

$$\mathrm{G}^{r\,ii'}_{LL'}(\mathbf{q}_{||}, E) = \sum_{\nu'} e^{-i\mathbf{q}_{||}\cdot(\boldsymbol{\chi}_\nu - \boldsymbol{\chi}_{\nu'})}\mathrm{G}^{r\,ii'}_{\substack{\nu-\nu'\\LL'}}(E) \qquad (4.21)$$

where $\mathbf{q}_{||}$ is a wave-vector in the 2D Brillouin Zone (2BZ). This leads to the following relation

$$G^{ii'}_{LL'}(\mathbf{q}_{||}, E) = G^{r\,ii'}_{LL'}(\mathbf{q}_{||}, E) + \sum_{i''L''L'''} G^{r\,ii''}_{LL''}(\mathbf{q}_{||}, E)\Delta t^{i''}_{L''L'''}(E) G^{i''i'}_{L'''L'}(\mathbf{q}_{||}, E) \quad (4.22)$$

which resembles the form of the Dyson equation of a linear chain of atoms. When the Green's functions $G^{ii'}_{LL'}(\mathbf{q}_{||}, E)$ are known, we have to back-transform $G^{ii'}_{LL'}(\mathbf{q}_{||}, E)$ in order to obtain $G^{\,i\,i'}_{\nu\,\nu'\,L\,L'}(E)$; this means that we obtain an integral over the 2D-Brillouin zone

$$G^{\,i\,i'}_{\nu\,\nu'\,L\,L'}(E) = \frac{1}{A_{2BZ}} \int_{A_{2BZ}} d\mathbf{q}_{||} e^{i\mathbf{q}_{||}\cdot(\boldsymbol{\chi}_\nu - \boldsymbol{\chi}_{\nu'})} G^{ii'}_{LL'}(\mathbf{q}_{||}, E) \quad (4.23)$$

where A_{2BZ} is the area of the 2D Brillouin Zone. In practice we will solve the Dyson equation (4.22) only for $\mathbf{q}_{||}$ vectors spanning the irreducible wedge of the 2D Brillouin zone (2IBZ). The choice of the set of $\mathbf{q}_{||}$ vector in the 2IBZ is achieved by "special point" methods [Cun74, MP76, Mac78]. If we indicate with $\mathbf{D}_j$ the set of symmetry operation which are valid for the surface geometry under consideration, we obtain the "perturbed" Green's function for a general $\mathbf{q}_{||}$ vector in the whole BZ by the application of the corresponding symmetry operation $\{\mathbf{D}_j\}$ as

$$G^{ii'}_{LL'}(\mathbf{D}_j\mathbf{q}_{||}, E) = e^{(\mathbf{D}_j - \mathbf{E})\mathbf{q}_{||}\cdot(\mathbf{R}_i - \mathbf{R}_{i'})} \sum_{L''L'''} D^T_{LL''} G^{ii'}_{L''L'''}(\mathbf{q}_{||}, E) D_{L'''L'} \quad (4.24)$$

where $\mathbf{q}_{||} \in$ 2IBZ, $\mathbf{E}$ is the identity operation and $D_{LL''}$ are the components of $\mathbf{D}_j$ in the angular momentum expansion

$$D_{LL'} = \int d\hat{\mathbf{r}} Y_L(\hat{\mathbf{r}}) Y_{L'}(\mathbf{D}\hat{\mathbf{r}}) \quad (4.25)$$

For a more in-depth presentation of the symmetry operations which appear in the case of "planar" defects, I refer to the Ph.D thesis of P. Lang [Lan96].

In the following, I will show that we can solve the Dyson equation (4.22) by an algorithm showing N-scaling behaviour as a function of the number of layers N in the system. As discussed at the beginning of this session, in order to simulate a "planar" defect the system is approached by setting up a slab geometry in which the perturbation perpendicular to the surface plane is restricted to a slab of material, composed of a finite number of layers. In Fig. (4.6) an example of such a slab geomety is sketched for the case of unsupported thin film, in which 4 layers of materials are sandwiched between 2 vacuum layers on each side, everything being embedded into semi-infinite half spaces of repulsive potentials.

As we have seen in section 4.2, the exponential decay of the reference structure constants allows us to solve Eq. (4.15) only inside a finite (and small, usually some tens of atoms) cluster of atomic sites. As sketched in Fig. (4.6), the cluster spans therefore over very few layers; this means that only layers relatively close to each other will be coupled and the reference structure constants $G^{r\,ii'}_{LL'}(\mathbf{q}_{||}, E)$ will be different from zero only for elements close to the diagonal (e.g. $|i-i'| \leq 2$ for a 19 atoms cluster and a *fcc* (001) plane). This kind of matrices for which only a few diagonal line adjacent to the main diagonal contain elements different from zero are called "band diagonal matrices" [PTVF86].

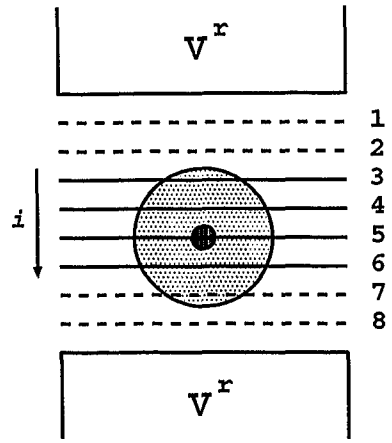

Figure 4.6: Example of slab geometry; the full lines are the substrate layers and the dashed line are vacuum layers

If we now rewrite the Dyson equation (4.22), as in Eq. (4.14), in terms of the scattering path operator $\tau_{\Delta\,LL'}^{ii'}$ we obtain,

$$G^{ii'}_{LL'}(\mathbf{q}_{||}, E) = \sum_{L''L'''} (\Delta t^{-1})^{i}_{LL''} \tau_{\Delta\,L''L'''}^{ii'} (\Delta t^{-1})^{i'}_{L'''L'} - (\Delta t^{-1})^{i}_{LL'} \tag{4.26}$$

with τ_Δ given by

$$\tau_{\Delta\,LL'}^{ii'} = \mathrm{M}^{-1} = [((\Delta \hat{t}^{-1}) - \hat{\mathrm{G}}^{r})^{-1}]^{ii'}_{LL'} \tag{4.27}$$

Since in the evaluation of the charge density we are interested only in the on-site elements ($n = n'$) of the Green's function $\mathcal{G}$ defined in (3.39), we have to solve Eq. (4.26) only for the diagonal elements $i = i'$. This means that only the diagonal elements of the scattering-path operator $\hat{\tau}_\Delta$ have to be calculated, i.e. only the diagonal elements of the inverse of the matrix M defined in (4.27). The matrix M is the sum of a diagonal matrix $(\Delta \hat{t}^{-1})$ and a band diagonal matrix $\hat{\mathrm{G}}^{r}$, and therefore it also shows a band diagonal form.

We introduce now the concept of "Principal Layer" (PL); the principal layer contains a number of adjacent layers N_P which we have to group together in order to fulfill the following requirements;

- The matrix M has to be divisible by N_P, i.e. $N_P * n = N$ with n an integer number.

- The matrix M has to be tridiagonal in the PL indices $P_i = 1, 2, .., n$, or equivalently each principal layer couples only with its nearest-neighbors , i.e. $M_{P_1,P_2} = 0$ if $|P_1 - P_2| > 1$

Efficient algorithms [God91, HM97, PTVF86] exist for the inversion of a tridiagonal matrix; moreover the computational effort for the calculation of only the diagonal elements scales, for such tridiagonal matrices, linearly with the number of layers N in the system (O(N)-scaling). Since most of the computational effort for the calculation of the charge density goes into the solution of the Dyson Equation (4.26), the whole calculation will retain the O(N)-scaling behavior.

In Appendix A I will present the algorithm for the calculation of the diagonal and off-diagonal elements of the inverse matrix of M, in case of the slab geometry; the details for the diagonal elements calculation can be also found in [Wil97]. I remand for the similar derivation in case of supercell geometry to the work of P. Zahn [Zah98]. The off-diagonal element of M^{-1}, In case of impurity calculation, the Green's function $G^{nn'}$ for a cluster of atoms C provides the information of the unperturbed host in which the impurity is embedded. In this case, all the elements $G^{ii'}$ with $i, i' \in C$ have to be calculated.

4.5 The half-space geometry: surface Green's functions

In the previous section we have seen how, by using the slab geometry, we can simulate a planar system (e.g. a surface). The same kind of systems can be simulated by a supercell calculation, repeating the slab also in the 3rd dimension; the system is periodic in all 3 dimensions and the Dyson equation for the perturbed system will be solved for all the **k**-vectors in the 3D Brillouin Zone. This is the same geometry used in slab calculations e.g. by the Full Potential Linearized Augmented-Plane-Wave (FLAPW) method [JMA78, KPF79]. In some cases the use of a supercell geometry is preferable to the use of the slab geometry, since the system behaves more stable during the self-consistency iterations; in the case of high-Miller surfaces, for instance, the convergence of ferromagnetic surfaces (like Fe(221)) presented serious difficulty by using the slab code, while convergence as achieved rather easily by using the supercell geometry. Unfortunatly both slab and supercell geometries are not able to simulate real semi-infinite geometries; a finite slab always shows Quantum Well States (QWS), due to the finite size of the substrates involved in the calculations. In the case of ferromagnetic materials, this finite size effects are very pronounced; as

in the case of the Fe/Co interface presented in the next chapter, in these cases the slab geometry is not suited since the presence of vacuum layers introduces a strong perturbation in the system.

With the traditional KKR program, the description of half-infinite planar systems have been achieved by a simple trick [Lan96]. Considering the bulk crystal as the unperturbed system, two half-crystals can be created by removing some monolayers in the crystal, or equivalently by perturbing it with some vacuum layers. The decoupling of the two surfaces by the work function barrier is achieved already by few vacuum layers (4 or 5), due to the exponential decay of the states with energy below E_F. Replacing the vacuum layers with some material, the calculation of the electronic properties of an arbitrary arrangement of layers can be achieved. This approach, however has the following limitations:

- The two half-spaces have to be the same, since they are obtained from the same host crystal.
- The spacing between the layers is also determined by the host crystal; the system is thus not allowed to relax, and the layers are fixed in their "ideal" positions.

In the following I will describe how, by the introduction of the "Surface Green's function", we can evaluate the perturbation on a slab introduced into two semi-infinite half-crystals, using the "screened" description of the method presented earlier. This half-space geometry will remove both the limitations connected to the traditional half-crystal technique. The two half-spaces can be different since they will be calculated separately from each other; moreover the structure constants are calculated locally for each atoms, and the interlayer distances can be different.

Let us divide the space in three regions; an Interface region, which describes the genuine slab including the perturbed layers at the two-half-spaces and the two semi-infinite systems on both sides of the Interface. The half-spaces we denote (following the notation presented by K. Wildberger [Wil97]), as Left (L) and Right (R) half-spaces. The index P, spanning the infinite matrix M defined in Eq. (4.27), is the principal layer index, introduced in the previous section. Since the coupling between principal layers is restricted to nearest-neighbour, and since the number of principal layer in the interface region is $n \geq 1$ the two half-spaces (L and R) are not coupled directly, i.e. $M_{L,R} = M_{R,L} = 0$.

In the case of a slab calculation, the scattering-path operator is only the inverse of the $M_{I,I}$ matrix; for an infinite system, instead, it is given by the interface elements

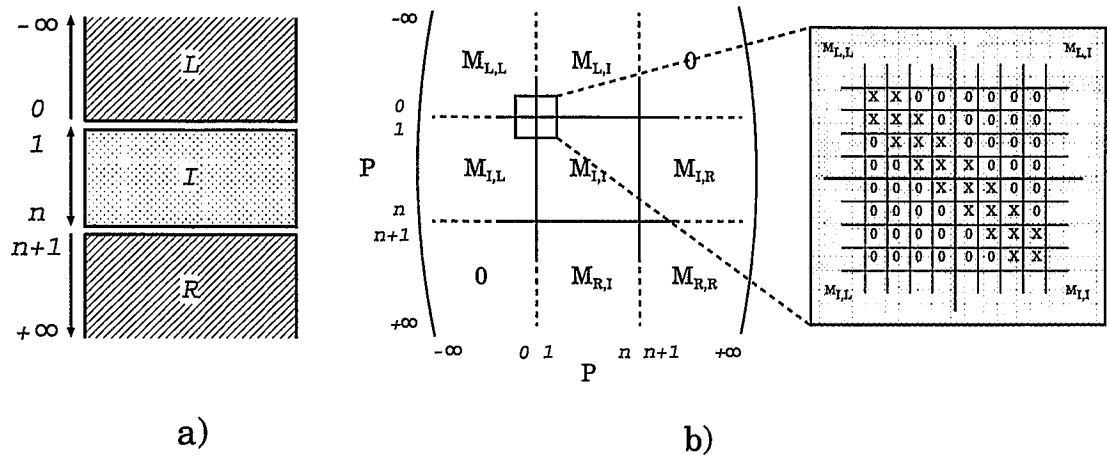

Figure 4.7: *a*) Schematic representation of the space, I is the Interface region, L and R are respectively the Left and Right half-spaces; *b*) The block form of the matrix M.

of the inverse of the infinite matrix M, i.e. $\tau_{I,I} = (M^{-1})|_{I,I}$, given by the equation

$$\begin{pmatrix} M_{L,L} & M_{L,I} & 0 \\ M_{I,L} & M_{I,I} & M_{I,R} \\ 0 & M_{R,I} & M_{R,R} \end{pmatrix} \cdot \begin{pmatrix} \tau_{L,L} & \tau_{L,I} & \tau_{L,R} \\ \tau_{I,L} & \tau_{I,I} & \tau_{I,R} \\ \tau_{R,L} & \tau_{R,I} & \tau_{R,R} \end{pmatrix} = \hat{I} \tag{4.28}$$

Since we are interested only in the operator $\tau_{I,I}$, we consider only the multiplication of M with the middle column of τ and impose the equivalence with the middle column of the identity operator $\hat{I}$; we thus obtain

$$\begin{cases} M_{L,L}\,\tau_{L,I} + M_{L,I}\,\tau_{I,I} = & 0 \\ M_{I,L}\,\tau_{L,I} + M_{I,I}\,\tau_{I,I} + M_{I,R}\,\tau_{R,I} = & 1 \\ M_{R,I}\,\tau_{I,I} + M_{R,R}\,\tau_{R,I} = & 0 \end{cases} \tag{4.29}$$

which solved in respect of $\tau_{I,I}$ reads

$$\tau_{I,I} = [M_{I,I} - M_{I,L}(M_{L,L})^{-1}M_{L,I} - M_{I,R}(M_{R,R})^{-1}M_{R,I}]^{-1} \tag{4.30}$$

The matrix M is tridiagonal with respect to the new principal layer indices; this implies (as sketched in the zoomed region in Fig. (4.7) *b*) that the Left (or Right) half-space and the Interface couple only through the corner blocks $M_{0,1}$ and $M_{1,0}$ (or $M_{n,n+1}$ and $M_{n+1,n}$). In the products in Eq. (4.30), all the elements will vanish exept two, i.e. $M_{I,L}|_{1,0}[(M_{L,L})^{-1}]_{0,0}M_{L,I}|_{0,1}$ and $M_{I,R}|_{n,n+1}[(M_{R,R})^{-1}]_{n+1,n+1}M_{R,I}|_{n+1,n}$.

Writing the explicit dependencies of the scattering-path operator τ, Eq. (4.30) reads,

$$\begin{aligned}\left[(\tau_{I,I}(\mathbf{q}_{||};E))^{-1}\right]_{pq} = [(\Delta t^p)^{-1}(E) - \mathrm{G}^r_{00}(\mathbf{q}_{||};E)]\delta_{p,q} - \\ -\mathrm{G}^r_{01}(\mathbf{q}_{||};E)\delta_{p,q-1} - \mathrm{G}^r_{10}(\mathbf{q}_{||};E)\delta_{p,q+1} - \\ -\mathrm{G}^r_{10}(\mathbf{q}_{||};E)[(M_{L,L})^{-1}]_{0,0}\mathrm{G}^r_{01}(\mathbf{q}_{||};E)\delta_{p,1}\delta_{q,1} - \\ -\mathrm{G}^r_{01}(\mathbf{q}_{||};E)[(M_{R,R})^{-1}]_{n+1,n+1}\mathrm{G}^r_{10}(\mathbf{q}_{||};E)\delta_{p,n}\delta_{q,n} \qquad (4.31)\end{aligned}$$

The first three terms in the right side of the above equation are the diagonal and upper and lower diagonal elements of the matrix $M_{I,I}$. In the case of a slab calculation, where the perturbation is limited to the interface region I, M is composed only of these first three terms. The other two terms represent the influence on the interface region due to the presence of the two half-spaces; the matrix elements $[(M_{L,L})^{-1}]_{0,0}$ and $[(M_{R,R})^{-1}]_{n+1,n+1}$ are in the literatur known as "*Surface Green's functions*". In order to calculate them we have to invert the semi-infinite matrices $M_{L,L}$ and $M_{R,R}$; this is achieved by the use of *decimation technique*; for a detalied explanation of the decimation technique I remand to the Ph.D. thesis of K. Wildberger [Wil97]. From the discussion presented so far it is evident that the left and right half-spaces are treated separately; this allow us to impose on the system two different half-crystals. Due to this, for instance, a real surface could be simulated replacing one of the two half-crystal by a semi-infinite vacuum space. If on the other hand the two half-spaces are choosen to be equal, we need to calculate only one of the two surface Green's functions, and derive the other exploiting the symmetry properties which hold for the matrix M; for layered systems this symmetries have been discussed by P. Lang [Lan96]. We will, in the case of two equivalent half-crystals, proceed as follows ;

- At first we have to calculate the t-matrices of the bulk materials, i.e. $\hat{t}_{bulk}$, which we want to place on the two sides of the interface region.
- The replacement of the reference system with the two half-crystals is achieved inserting the perturbation $\Delta\hat{t}_{bulk} = \hat{t}_{bulk} - \hat{t}^r$ in all the diagonal elements of the semi-infinite matrices $M_{L,L}$ and $M_{R,R}$.
- We calculate then, by using decimation techniques, the surface Green's functions given by the elements $[(M_{L,L})^{-1}]_{0,0}$ and $[(M_{R,R})^{-1}]_{n+1,n+1}$.
- We insert them in Eq. (4.31) and then invert the matrix M. This step is performed using the same O(N) algorithm used in the case of a slab calculation (see Appendix A), since the matrix M retains its tridiagonal form.

The presence of a bulk crystal on the sides of the slab will introduce some conceptual difference in the solution of the self-consistency procedure. In first place, for the half-space geometry the Fermi energy will be fixed by the bulk crystal, in contrast to a slab geometry or supercell geometry where the Fermi energy is allowed to adjust in order to enforce charge neutrality in the slab. To achieve charge neutrality in the interface region we have therefore to adopt a different approach. If we indicate with Q the charge in excess in the slab in the $i-th$ iteration, the Coulomb term which has to be added in order to construct the new potential that will enter in the next iteration, will be calculated for a system composed of the slab and of two additional layers ("ghost" layers) in which we place two equal charges $q = -\frac{Q}{2}$. This "ghost" layers are usually placed on the sides of the slab, and at distances equal to the interlayer distance between first-neighbours layers. This approach turned out to be very effective, and good charge neutrality are achieved after self-consistency.

Moreover the principal layer, in the case of half-space geometry, has to fulfill an additional requirement. Since the matrices $M_{L,L}$ and $M_{R,R}$ of the half-spaces will be constructed by basically repeating the three blocks G^r_{01}, G^r_{10} and $[(\Delta t_{bulk})^{-1} - G^r_{00}]$ along the three diagonal, it is of fundamental importance that they reproduce the correct periodicity of the system. In the case, for instance, of layered system with a planar unit cell, the stacking of the atoms in the cell will, through the Fourier transform given by Eq. (4.21), enter in the calculation of the wave-vector dependent reference structure constants $G^{r\,ii'}_{LL'}(\mathbf{q}_{||}, E)$ where i is the layer index. Let us suppose, for example, that the planar unit cell is composed of 2 different atoms; the elements of the first upper diagonal $G^{r\,i(i+1)}_{LL'}$ will have an ABAB$\cdots$ stacking, where the element A and B appear respectively when two atoms in the plane or in different planes are coupled. The size of the principle layer has then to take into account this "stacking", since the reference system in the two half-spaces will be constructed by repeating these elements all over the space. In other words all the periodicity has to be contained in the blocks characterized by the principal layer index. If we indicate with N_P the number of layers in each PL and with n_s the number of different elements defining the stacking in the reference structure constants, this means that N_P has to be a multiple of n_s.

4.6 Surface energies

The surface energy is one of the most fundamental electronic property of a metallic surface; its determination is of great importance in the undertanding of a wide range

of surface phenomena like faceting, roughening and crystal growth. In the last two decades much effort has been made to develop *ab-initio* methods suited for the evaluation of the physical properties of surfaces. They basically use slab, as the Full potential-Linearized Augmented Plane Waves (FLAPW) method [BPD89, HB98], or supercell geometries like the Full Potential LMTO method [MHS92] or deal directly with the electronic states in a semi-infinite crystal like the LMTO-Green's functions method developed by Skriver *et al.* [SR91, SR92]. By means of this last method, it was possible to present the first systematic calculations of surface energies [SR92, VRSK98], and very recently of step and kinks energies [VSK99].

Several tests performed with the "screened" KKR program [Wil97] in the slab geometry have shown that total energies of bulk systems could be achieved with good accuracy. The total energy of an atom sitting in the middle layer of Cu and Fe (001) slabs compares very well with the bulk values obtained by traditional KKR band-structure codes; similar agreement is found for a semi-infinite bulk calculation. In both case differences of the order of 1 mRy are expected since the results were obtained by different Brillouin Zone integrations, 3-dimensional for the traditional band-structure code and 2-dimensional for the SKKR code in the slab and half-space geometry.

Cu bulk	**Total energy (in Ry)**	s	p	d	f
Tight Binding (19 TB cluster)	−3275.918671	0.67814	0.71505	9.54535	0.06145
Tight Binding (79 TB cluster)	−3275.917978	0.67693	0.71415	9.54726	0.06165
Band Structure	−3275.917983	0.67698	0.71421	9.54711	0.06166

Table 4.1: Cu bulk total energy; comparison between the "traditional" band-structure method and the SKKR method. The s, p, d and f charges are also listed.

In table (4.1) I present similar tests, but for a Cu crystal calculated with the SKKR program in the bulk geometry. For all the results in this section a Cu lattice constant of $6.83\,a.u.$ (atomic units) has been used, and angular momenta up to $l_{Max} = 3$ have been included in the expansion of the wave functions. As is evident from table (4.1), when we increase the size of the TB cluster inside which we calculate the "screened" structure constant from 19 to 79 repulsive potentials, the agreement

between the two calculations improves sensibly. This is fully consistent with the idea that if the size of the TB cluster would be taken infinitely big, no approximation would be introduced, because of the exactness of the "screening" transformation. For simplicity for both bulk and surface calculations the small TB-cluster of 19 atoms will be used; the accuracy on the calculated total energies will be thus of the order of $1\,mRy$. Moreover since both slab and semi-infinite systems presented always, reached self-consistency, very good charge neutrality (of the order of 10^{-4} or even better), we didn't include the correction to the single-particle energies by Lloyd's formula as it is usually done for impurities calculations [DWZD89].

In the following, I present test calculations for the surface energy of the three low-index *fcc* Cu surfaces, i.e. (001), (110) and (111) by means of both slab and half-space geometries. For the (001) plane the dependence of the surface energy on the size of the "surface" region will be explicitly discussed. Afterwards I will compare the present results with existent surface energy calculations performed by means of the LMTO-GF method [VRSK98].

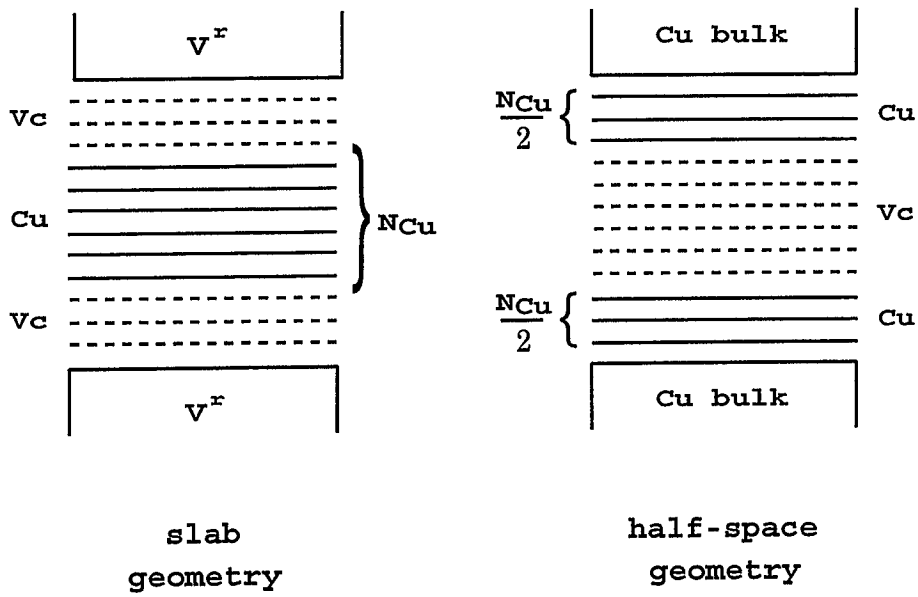

Figure 4.8: Slab and half-space geometry; N_{Cu} is the number of layers considered to simulate the "surface" regions.

The surface energy is defined as the surface excess free energy per unit area of a particular crystal facet, or equivalently as one half of the energy needed to cut an infinite crystal along one plane into two separated semi-infinite pieces. We can thus calculate the surface energy as follows. If we indicate with N_{Cu}, see Fig. (4.8),

the number of Cu layers in the "surface" region which enter in the self-consistency process, the surface energy E_s is given by

$$E_s = \frac{1}{2}(E_{Tot} - N_{Cu}E_{Cu}^{bulk}) \tag{4.32}$$

where E_{Tot} is the sum of the total energies of all the atoms (Cu and Vacuum atoms) in the cell , and E_{Cu}^{bulk} is the total energy of bulk Cu. This "reference" bulk total energy is somehow arbitrary, but it turns out that it has to be choosen carefully in order to have consistent results for the two different geometries. For the half-space geometry E_{Cu}^{bulk} is the total energy of the bulk Cu imposed from the two half-spaces at the boundaries of the interface region; it will be thus the same for all the calculations performed in the half-space geometry. In the case of slab calculations, E_{Cu}^{bulk} is the total energy of "more bulk like" Cu atom sitting in the middle layer of the Cu substrate, and it will be different for each slab calculations, i.e. different N_{Cu} and surface orientation.

Cu (001) surface energies (in eV/atom)		
N_{Cu}	Half-space	Slab
6	0.924	1.032
8	0.934	0.899
10	0.935	0.940
12	0.933	0.932
14	0.933	0.931
16	0.932	0.937

Table 4.2: Comparison between the Cu (001) surface energies calculated by slab and half-space geometries.

In table (4.2) I present the comparison beween the total energies of the *fcc* (001) Cu surface calculated by slab and half-space geometries as a function of the number of Cu layers N_{Cu}. In the half-space geometry the surface energy is converged up to some meV already with rather few Cu layers, i.e. $N_{Cu} = 8$. For the slab geometry, because of finite-size effects present in the Cu substrate, more layers are required to achieve the same accuracy, i.e. $N_{Cu} = 12 - 14$. The correct choice of E_{Cu}^{bulk}, as described above, is of fundamental importance to get consistent results between the two geometries; if the E_{Cu}^{bulk} used in the half-space geometry is used as the reference bulk energy also for all slab calculations, we observe systematic differences of the order of tens of meV in the surface energies. The results in table (4.2) suggest

that accurate surface energies can be obtained with both methods. The half-space geometry shows a faster and more stable convergence behaviour. However also the slab geometry allows an accurate calculation of the surface energy, on condition that we consider the number of layers in the substrate high enough to reach a good bulk total energy in the middle of the substrate itself.

	$A_{2\text{IBZ}}$ $[(\frac{2\pi}{a})^2]$	N. of $\mathbf{q}_{\|\|}$ points	N_{Cu}	**Surface energy (in eV/atom)**		
				Half-space	Slab	LMTO
Cu (001)	$\frac{1}{8} \cdot 2$	55	14	0.933	0.931	0.906
Cu (110)	$\frac{1}{4} \cdot \sqrt{2}$	100	18	1.378	1.381	1.323
Cu (111)	$\frac{1}{12} \cdot \frac{4}{\sqrt{3}}$	40	12	0.714	0.708	0.707

Table 4.3: Surface energies for the low-index Cu surfaces; for each plane the area of the irreducible part of the 2D Brillouin zone $A_{2\text{IBZ}}$, the number of $\mathbf{q}_{||}$ points for the contour energies, and the number N_{Cu} of Cu layers in the surface region are provided. In the last column I include the surface energies obtained by L. Vitos *et al.* [VRSK98].

With this condition in mind, we can thus set up the systems used to calculate the surface energies for the three low-index Cu surfaces. In table (4.3), these surface energies are listed together with the parameters used in the calculations. The number of Cu layers N_{Cu} and $\mathbf{q}_{||}$ points considered in the calculations vary for the three orientations, because of the different interlayer spacings and the different area of the irreducible part of the 2D Brillouin Zones. In the last colum I include the results obtained by L. Vitos *et al.* by means of the LMTO-Green's function method [VRSK98]. The SKKR surfaces energies follow the correct trend and can be quantitatively compared with the LMTO results; the small differences (of the order of tens of meV) have to be expected since the calculations were performed for different lattice constants, i.e. the GGA value $a_{\text{latt}} = 6.92\, a.u.$ for the LMTO results and the LDA value $a_{\text{latt}} = 6.83\, a.u.$ in the present work. If we express the surface energy in eV/atom, as it is done in tables (4.2) and (4.3), the trend for the surface energies as a function of the roughness of the surface plane can be qualitatively understood in terms of the broken bonds model; this model states that the main contribution to the surface energies comes from the broken bonds at the semi-infinite surface. The number of these broken bonds N_b increase when the surface becomes more open (more rough), i.e. $N_b = 3$ for *fcc* (111), $N_b = 4$ for *fcc* (001) and $N_b = 5$ for *fcc*

(110). The same trend can be observed for the surface energies, proving the qualitative validity of this model. For instance, by taken the calculative value of $0.93\,eV$ for the Cu(001) surface, one would expect from the model the value $\frac{3}{4} \cdot 0.93 = 0.70\,eV$ for the (111) and $\frac{5}{4}\,0.93 = 1.17\,eV$ for the (110) surface which is in reasonable agreement with the above results. (For this model it is important to give the surface energy in units of energy per atom, and not energy per area).

Finally, I have to remark that for all the results presented in table (4.3) the layers are fixed in their "ideal" position, i.e. inter-layers relaxations are neglected. Relaxations at metal surfaces can show a very different behaviour from metal to metal, even if general features can be found like the inward relaxation for the top layer which is common to almost all the studied metal surfaces [JMJ86] (exceptions are, for instance, the outward relaxations found for Pd(001) and Rh(001) [MHS92]). These relaxations, which were found to increase with the roughness of the surface plane, are believed to influence the surface energy normally only to a few per cent.

Chapter 5

Fe/Co interfaces and dilute alloys

The study of the hyperfine interactions in solids recieved considerable attention in the last decades both from the experiment and theory, since they provide unique microscopic information about the structural as well as magnetic properties of surfaces, interfaces and dilute alloys [Kra83, Sch88, RDF+97, BAZD87, AAB+90]. They arise from the interaction between a nuclear moment, which can be the magnetic dipole or the electric quadrupole moment, and the electromagnetic field due to the electrons, and lead to an energy splitting of the nuclear levels.

There are two main types of experimental techniques able to measure the hyperfine interactions. The first one makes use of the resonance effect and works in the "energy domain" measuring directly the energy splittings induced by the hyperfine interactions, like Mössbauer effect and Nuclear Magnetic Resonance (NMR) experiments. The second type works in the "time domain" measuring the precession frequency of the nuclear spins related to the energy splittings of the γ radiation emitted by the radioactive nuclea, like Perturbed Angular Correlation (PAC) spectroscopy.

Since the informations which are supplied by these experiments are often very difficult to interpret and far from transparent, reliable theoretical calculations are very much needed in order to provide a theoretical basis for the understanding of the experimental findings. *Ab initio* calculations have shown in the past to be well suited for this scope, and have succeeded to reproduce, and explain, qualitatively and often also quantitatively experiments on dilute ferromagnetic alloys [BAZD87, AAB+90, KSP+00, MSN+98], *hcp* metals [BSD88] and defects in semiconductors [Set96, Set99]. In this chapter we are interested in the hyperfine interactions arising between the magnetic nuclear dipole moment and the magnetic field due to the electrons, i.e. the so called *hyperfine fields*. The hyperfine fields (*hff*) are

a fingerprint of the magnetic environment in which the nucleus of the probe atom under consideration is embedded.

A new burst for the experimental point of view has been given when by means of Molecular Beam Epitaxy (MBE) it was succeded to stabilize Co in the exotic *bcc* structure grown on (110) GaAs [Pri85], while in nature it retains the *hcp* structure up to $T = 425°K$ before becoming *fcc* and subsequently melting. Due to this discover many experimental studies on FeCo alloys and Fe/Co multilayers were performed in order to characterize the magnetic properties of this new phase of Co.

This chapter, that will deal mainly with the study of such Fe-Co systems, will be divided in two parts. The first part was motivated by a recent Time Differential Perturbed Angular Correlation (TDPAC) spectroscopic study proposed by Swinnen *et al.* [SMD+97], which studied the hyperfine fields induced on Cd probe atoms at the *bcc* Fe/Co (110) interface; by using the Stearns' model the magnetic moment profile at the Fe/Co interface is deduced from the measured hyperfine fields. I will compare the magnetic moment profile at the (001) and (110) *bcc* Fe/Co interface calculated by means of the SKKR program and will also perform calculations for Cd impurities at the (110) Fe/Co interface in order to compare directly with the measured hyperfine fields. The second part of the chapter is devoted to the understanding of the origin of the hyperfine fields in the Fe/Co systems; the hyperfine fields at the Fe/Co interface and for Fe/Co alloys is discussed and compared with the findings of Mössbauer and NMR experiments. Common features as well strong disagreements with experiments are found.

5.1 Hyperfine fields

Before presenting the physical system under interest let us give a brief description of the quantity which will be mainly discussed in the next sessions, i.e. the *hyperfine field* (*hff*). The hyperfine field arises from the interaction between the magnetic dipole moment and the magnetic field induced by the electrons at the nuclear position. The main contributions to the hyperfine field, as obtained by the non-relativistic Schrödinger theory, is the so called Fermi contact term [Fer30] given by the expression

$$H_{hf} = \frac{8\pi}{3} m(0) \tag{5.1}$$

where $m(0)$ is the value of the magnetization density $m(\mathbf{r})$ at the nuclear position, i.e. $\mathbf{r} = 0$, given by

$$m(0) = \int^{E_F} [n^{\uparrow}(0,E) - n^{\downarrow}(0,E)]dE \tag{5.2}$$

and $n^{\uparrow\downarrow}(0,E)$ is the local density of states for spin-up (down) electrons at this position. Only the s orbitals, which have a non-vanishing density of states at the nuclear position, contribute to the contact term in Eq. (5.1). Since the *hff* is driven by the behaviour of the wave functions close to the nucleus, relativistic effects are very important already for elements with small nuclear charge. The correct relativistic expression for the hyperfine field has been originally derived by Breit [Bre30], and more recently rederived by Blügel *et al.* [BAZD87]; starting from the Dirac equation, the original expression can be uniquely splitted in three parts which are the relativistic generalizations of the contact, dipolar and orbital contributions to the hyperfine field. The results for the hyperfine fields presented in the following sections, unless explicitly stated, are derived in the Scalar Relativistic Approximation (SRA). Since spin-orbit coupling is neglected in this approximation, the orbital term vanishes; moreover dipolar terms are usually small and they vanish in case of cubic symmetry in the system. In the SRA we are thus left again mainly with the contact term, or more precisely with the relativistic expression of it, given by the Breit's formula

$$H_{hf}^{Breit} = \frac{8\pi}{3} m_{\tau} \tag{5.3}$$

where, comparing to the non relativistic limit, the effective magnetization density m_{τ} near the nucleus is obtained as an average over a small region around the nucleus whose diameter is the Thomson radius $r_T = \frac{Ze^2}{mc^2}$.

There are two main contributions to this contact term; they arise from the intraatomic spin polarization of the s orbitals induced by the d orbitals in the same site and the interatomic polarization induced by the d orbitals of the neighbouring site; the first process acts on both core and valence s orbitals, while the second term influences only the valence s orbitals, which have sufficient spatial extent. It was shown in the literature by means of impurity calculations in Fe and Ni hosts [AAB+90, BAZD87] that the core contribution is mainly proportional to the total magnetic moment of the probe atoms, while the valence contribution has a more complicated behaviour. Moreover since *sp* impurities are non-magnetic in metals, the contribution to the *hff* from the core orbitals vanishes and only the valence contribution remains, i.e. only *sd* interatomic polarization is efficient; the total *hff*

has thus mainly a "transferred" character due to the magnetic environment in which the non-magnetic probe atom is embedded.

While the LDA has proved to account very well for the ground state properties of most elements in the periodic table, it is well known from the literature to fail in reproducing the *hff* of pure transition metals like Fe, Co or Ni [Jan79]. The introduction of relativistic effects, i.e. orbital and dipolar contribution to the *hff*, not only did not succeed to explain the discrepancy between theory and experiments but even increased it [ESG88, GE96]. This discrepancy is nowadays generally believed to arise from the poor treatment of the core polarization mechanism [BAZD87]. The only way to overcome this problem would be to consider non-local functionals; one of the methods which seems more promising in this respect is the Optimized Effective Potential (OEP) method which has shown recently to improve remarkably the hyperfine fields of bulk Fe, Co and Ni [AK99, Kot98].

In the first part of this chapter the attention will be driven mainly on the *hff* induced on a Cd probe atom embedded in a ferromagnetic Fe/Co interface environment. Since Cd is non-magnetic, only the valence *s* orbitals will contribute to the *hff* which is not therefore influenced by this "core polarization" problem. On the other hand for 5*sp* and 6*sp* impurities in Fe the relaxation of neighboring Fe atoms is expected to induce some changes especially for impurities at the end of the series [KSP+00]. Since Cd is at the beginning of the 5*sp* series, the *hff* are found to be modestly influenced by the relaxation of the Fe neighbors. The second part of this chapter is dedicated to the study of the Fe and Co hyperfine fields at the Fe/Co interface; the *hff* of Fe will be systematically underestimated due to the above failure of the LDA for the correct description of the core polarization, while for Co the *hff* will compare rather well with the experiments.

5.2 Cd hyperfine fields at the Fe/Co interface

In this section I present the results for the Fe/Co (001) and (110) interfaces. After a brief discussion of the magnetic moment profile obtained by the *ab initio* SKKR calculations, I will compare our results with the magnetic moment profile presented by Swinnen *et al.* [SMD+97] from the interpretation of their hyperfine field measurements. As already discussed in the literature by [ŠV98, NJS99], no oscillatory behavior neither on the Fe nor on the Co side of the interface is observed in the *ab initio* calculations, while very large oscillations for both Fe and Co atoms at the interface are claimed in the work of Swinnen. Afterwards, in order to compare di-

rectly with the measured hyperfine fields, I will present the results of Cd impurities at the (001) and (110) Fe/Co interfaces, and compare the calculated *hff* with the measured ones.

5.2.1 The (001) and (110) *bcc* Fe/Co interface

To model the (001) and (110) Fe/Co interface we consider respectively a Co slab being embedded between two, left and right, halfcrystals of *bcc* Fe; the electronic structure of bulk Fe at the two sides of the slab is imposed by means of the surface Green's function technique described in section 4.5. A TB cluster of 89 atoms has been choosen which leads to $N_c = 4$ layers in each PL for the (001) interface and $N_c = 3$ for the (110) (see section 4.4). In order to remove as much as possible finite size effects in the Co slab, up to 11 Co monolayers where considered; since the total number of layers in the system has to be a multiple of N_c, I placed respectively 5 and 4 Fe layers on the two sides of the (001) slab and 5 Fe layers on both sides the (110) Co slab, which leads to a total of 20 and 21 monolayers for the (001) and (110) Fe/Co interfaces. The *bcc* structure has a 2D-BZ area of $(\frac{2\pi}{a})^2$ in the (001) direction, and of $\sqrt{2} \cdot (\frac{2\pi}{a})^2$ in the (110); moreover in the (110) the irreducible part is $\frac{1}{4}$ of the whole BZ, as opposed to $\frac{1}{8}$ in the case of (001) direction. To reach convergence with respect to the number of $\mathbf{q}_{||}$ points used in the selfconsistency cycles, 45 and 121 $\mathbf{q}_{||}$-points for the contour energies, and 465 and 1130 $\mathbf{q}_{||}$-points near the real axis were used respectively for the (001) and (110) directions; 31 energy points in the complex contour have been used and 5 Matsubara poles returning to the real axis at the Fermi energy. The atoms in the system are arranged in the *bcc* structure with the theoretical lattice constant of Fe $a_{latt}^{theor} = 5.205\, a.u.$; moreover for the (110) interface I performed calculations also for the experimental equilibrium Fe lattice constant $a_{latt}^{exp} = 5.406 a.u.$. No lattice relaxations were included, i.e. the Co monolayers were fixed at the Fe bulk distances.

The resulting profile of the local moments at the (100) and (110) interfaces are shown in Fig. (5.1); for both orientations the Co moments are practically constant up to the interface, while the Fe moments monotonically increase reaching the value of $2.42\,\mu_B$ at the (001) interface layer, and $2.29\,\mu_B$ at the (110) interface. The results are in good agreement with earlier calculations [ŠV98, NJS99]; the somewhat larger values obtained by these authors are a consequence of the experimental Fe lattice constant used in these calculations.

For an understanding of the moments at the interface it is important to recall the behaviour of bulk Co and Fe and FeCo alloys. Bulk Co is for all three phases

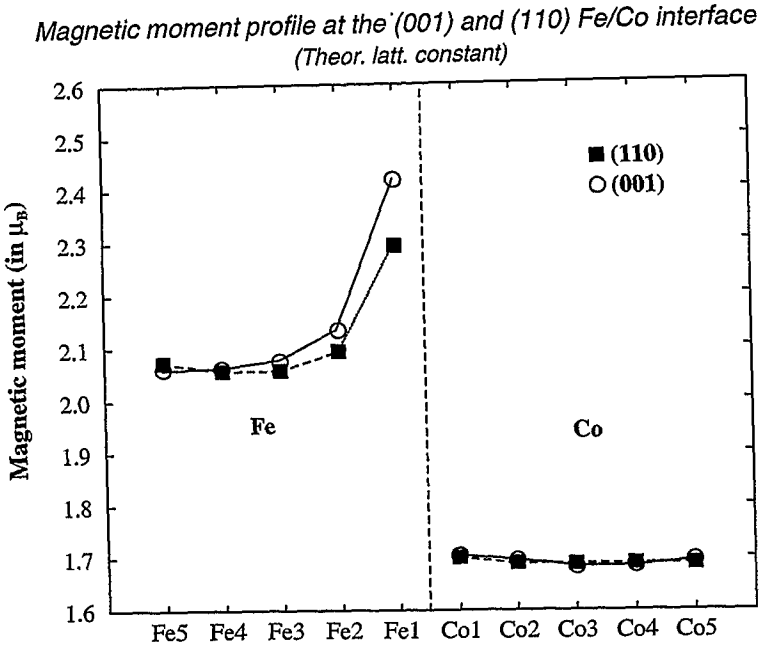

Figure 5.1: Magnetic moment profile at the (001) (empty circles) and (110) (filled squares) Fe/Co interface.

(*hcp*, *fcc* and *bcc*) a strong ferromagnet characterized by a filled majority band and a moment of about 1.7 μ_B, being insensitive to structural and environmental changes. On the other hand, due to the larger extent of the wave function resulting in stronger hybridisation and bandbroadening, *bcc* Fe is a weak ferromagnet with about $0.4-0.5$ unoccupied *d*-states in the majority band, leading to a strong sensitivity of the Fe moment to environmental changes. This can be clearly seen in *ab-initio* calculations for disordered $Fe_{1-x}Co_x$ alloys [DZAE91]. With increasing Co concentration the average alloy moment increases and attains a maximum at about 25% Co, despite the fact that the Co moment, being about 1.7 μ_B independently of the concetration, is much smaller than the Fe moments. Calculations for the dilute limit of a single Co impurity in Fe show, that around each Co impurity the neighbouring Fe moments increase in a region of at least five Fe shells [DSB+89] so that for each Co atom the total alloy moment increases by about 1 μ_B. All these *ab-initio* calculations are in good agreement with the experimental information from magnetisation measurements and neutron scattering.

In analogy to the alloy, the behaviour at the Fe/Co interface is characterized by the filling of the local majority *d*-states of Fe being driven by the decrease of hybridization and the resulting band narrowing. The differences between the (001) and (110) interface can be directly understood from the different coordination of an

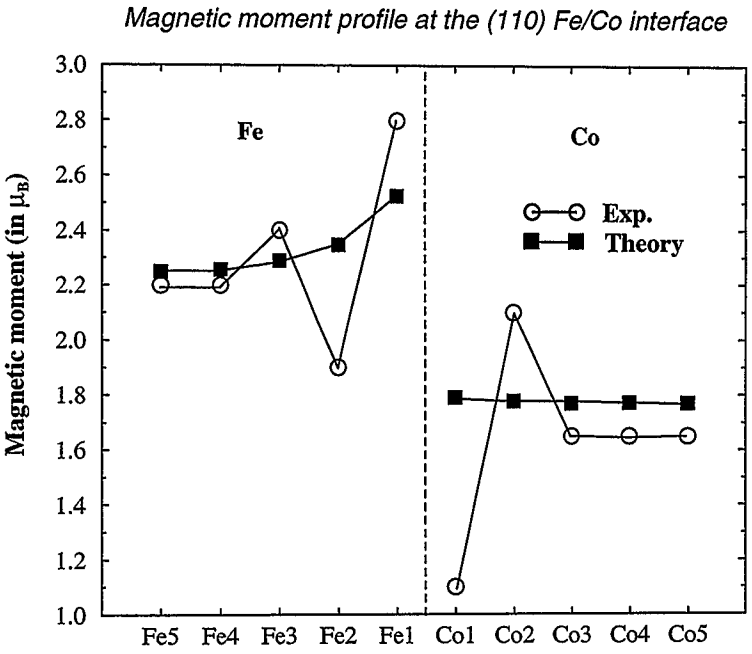

Figure 5.2: Comparison between the theoretical (filled squares) and experimental (empty circles) magnetic moment profiles at the (110) Fe/Co interface.

Fe atom in the first Fe layer, having 4 *nn* and 1 *nnn* Co atoms at the (001) interface, but only 2 *nn* and 2 *nnn* Co atoms in the (110) case.

It is time now to compare the calculated magnetic moments of the (110) Fe/Co interface with the one claimed by Swinnen *et al.* [SMD+97]. Since is well known that using the LDA Fe lattice constant the magnetic moment of Fe is underestimated, in order to compare with the experiment I present in Fig. (5.2) the magnetic moment profile for the *bcc* (110) Fe/Co interface obtained by using the *experimental* Fe lattice constant, i.e. $a_{latt} = 5.406 a.u.$; due to the increase in volume by moving from the LDA to the exp. lattice constant, the Fe magnetic moment increases up to $2.25\mu_B$ for the "bulk" like layers as compared to $2.07\mu_B$ for $a_{latt} = 5.205\, a.u.$, while the Fe interface layer has a moment of $2.52\mu_B$ as opposed to $2.29\mu_B$, which correspond to an overall increase of 10%. For Co layers the change is less pronounced, and the magnetic profile is found to be almost constantly shifted by $0.1\mu_B$ for all the layers in the Co slab, i.e. less than 6%.

As evident from Fig. (5.2), no oscillatory behaviour is found neither for the Fe and the Co layers approaching the interface. It is well known that oscillations of the Fe moments around the bulk value exist for the Fe surface as a function of the distance from the surface layer; nevertheless these oscillations are screened if Fe is coated with a metal[MEJS95]. Some oscillations remain in the case of coating with

Ti, Mn and V, which actually couple antiferromagnetically with the Fe substrate; they are due to the spin-dependent screening of the perturbation caused by the presence of the neighboring coating material, and in the case of an extended interface they are very small and rather long-ranged.

Which could be the origin of this large discrepancy between the theoretical and experimental picture?. First of all the magnetic profile of the Fe/Co interface is not measured directly, but rather deduced from TDPAC experiments of the *hff* of Cd probe atoms at the Fe/Co interface. Using the Stearns' model [Ste73], which gives a very simplified, i.e. wrong, dependence of the *hff* on the magnetic environment, the magnetic profile is deduced from the measured *hff*. I will not comment on details of the validity of this model, but rather try to compare directly the measured and calculated *hff* of the Cd probe atoms in the next section. What one can say here, is that one of the main assumptions for the fitting procedure is that the contribution from the *hff* field is coming mainly from the magnetic environment of the *1st shell* around the probe atom; as will be discussed in the next this assumption is not valid for the *bcc* structure, since the next nearest neighbors contribute as much and some times more than the nearest neighbors to the valence polarization and therefore to the total *hff*. The oscillatory behaviour of the magnetic profile proposed by Swinnen *et al.* and assigned to a Fe/Co sharp interface, has no theoretical justification, and is actually in conflict with the behaviour known from the Fe/Co alloy.

5.2.2 Cd impurities at the (001) and the (110) Fe/Co interface

In order to compare directly with the measured Cd *hff*, I performed impurity calculations for Cd substitutional defects placed in different layers near the Fe/Co interface region (see Fig. (5.3)). The Cd impurity and a cluster of 27 potentials around the impurity (up to the *3rd* shell) are allowed to readjust self-consistently until convergence is reached. In the next pictures I used the following notation; I indicated with Fe-n (Co-n) the $n-th$ Fe (Co) layer away from the interface, i.e. Fe1 is the interface layer, Fe2 is the second layer from the interface etc., and the same holds for

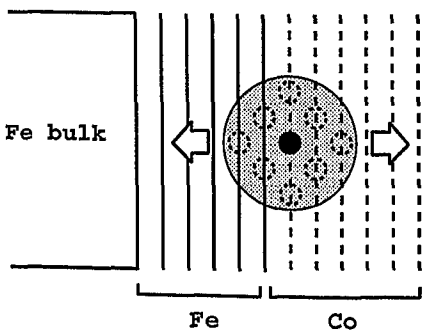

Figure 5.3: Cd impurity at the Fe/Co interface. The arrows indicate that the Cd atom can be positioned in different layers.

the Co layers.

(i) Calculated Cd *hff* at the Fe/Co (001) and (110) interface

In Fig. (5.4) the results for the Cd hyperfine fields at the (001) and (110) Fe/Co interfaces are shown; both the curves are calculated with the LDA Fe lattice constant, i.e. $a_{latt}^{theor} = 5.205\, a.u.$.

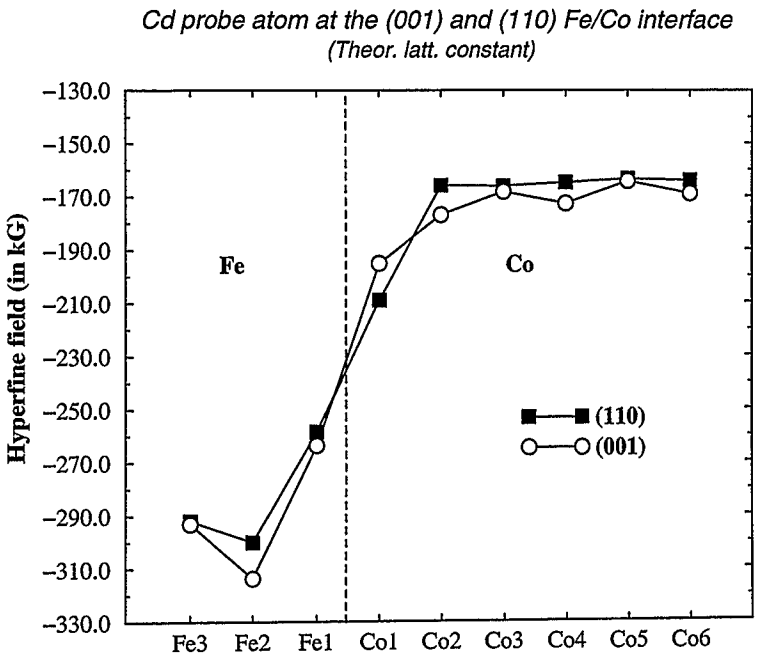

Figure 5.4: Cd *hff* at the (001) (empty circles) and (110) (filled squares) Fe/Co interface.

Since Cd is a non-magnetic impurity the *hff* is determined by the valence electrons, and since no orbital contributions are considered, it arises from the *s*-polarization of the Cd atom due to the spin-polarized *d*-orbitals of the neighboring Fe and Co atoms; the core contribution is small and amounts to about $-7\,kG$ in the Fe bulk layers and decreases to less than $-1\,kG$ as soon as the Cd is placed at a Co substitutional site. The Cd hyperfine has therefore mainly a "transferred" character; it is high where the neighboring atoms have large magnetic moments, i.e. in Fe, and decreases by almost a factor of 2 when Cd is placed in a Co environment. The Cd hyperfine field is negative as expected from the calculation of Cd impurities in Fe and Ni hosts [AAB+90]. Since the dependence of the *hff* is restricted to the very close environment, i.e. the first two neighboring shells mainly, a Cd atom in the Co2 layer shows already the same *hff* as a Cd impurity in bulk Co. The small oscil-

lation in the case of the (001) direction, are due to finite size effects in the (001) Co slab which lead to small oscillations (barely visible in Fig. (5.1)) in the magnetic moment profile, and therefore in the induced *hff*. From the *hff* of Cd in a bulk Fe environment, which is assumed with good approximation already in the Fe3 layer, the *hff* decreases (in absolute value) in two steps towards the Cd value in bulk Co.

Even if the general trend is similar for the two interface orientations, some differences are found, due to the different Fe magnetic moments to which the Cd atom is exposed in the Fe2, Fe1 and Co1 layers. It is important to note here that the larger *hff* of Cd in the Co1 layer found for the (110) with respect to the (001) orientation is somehow counterintuitive. In fact if one assumes that the "transferred" *hff* are driven by only the NN atoms around the Cd, one would expect a larger *hff* for the (001) orientation than for the (110) one, for two reasons. In first place the magnetic moments at the Fe1 interface layer is larger for the (001) direction (see Fig. (5.1)) and so should be also the transferred *hff* to the Cd. The second reason has to do with the different number of NN Fe which a Cd in Co1 has in the (001) and (110) orientation; in the (001) case there are 4 NN Fe in the Fe1 layer and 4 NN Co in the Co2, while in the (110) case only two Fe NN in the Fe1, and 4 NN Co in the Co1 plus 2 NN Co in the Co2 layers are present (the number of NN and NNN around an atom as a function of the layer number is depicted in Fig. (5.5))

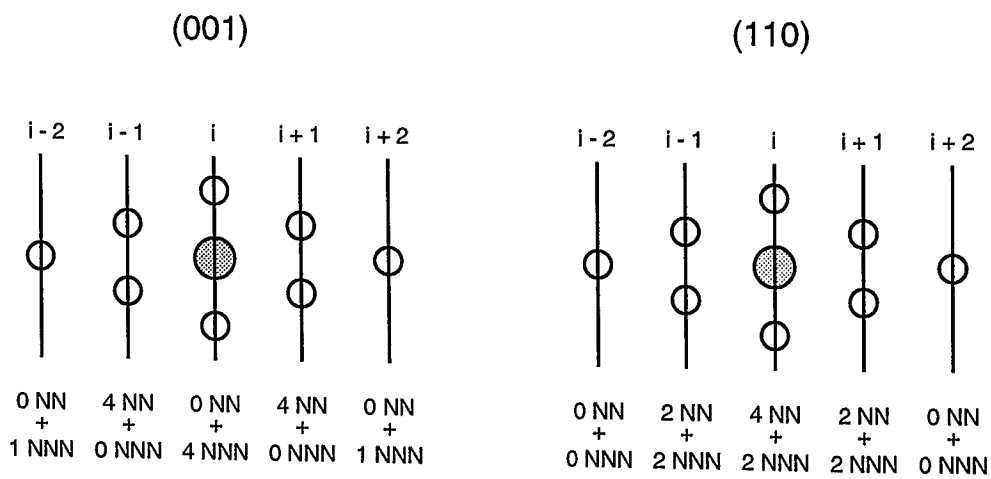

Figure 5.5: NN and NNN sites at the (001) and (110) *bcc* as a function of the layer number.

The count of the Fe NN is therefore in favour of the (001) surface, and a larger induced Cd *hff* in the Co1 layer should be found for the (001) Fe/Co interface; as evident Fig. (5.4) this is clearly not the case. For Cd in Fe1 and Fe2 layers things

are complicated by the fact that the Fe layers exhibit different magnetic moments approaching the interface. This discrepancy could be avoided if also the next nearest neighbors would influence the "transferred" *hff* by the same degree as the nearest neighbors.

(ii) The role of the First and Second NN Fe atoms

In order to investigate this, I present in Fig. (5.6), calculations of Cd impurities in a Co bulk matrix but with different numbers of Fe impurities in the $1st$ and $2nd$ shell; as for the Cd at the Fe/Co interface, perturbed potentials up to the $3rd$ shell are included.

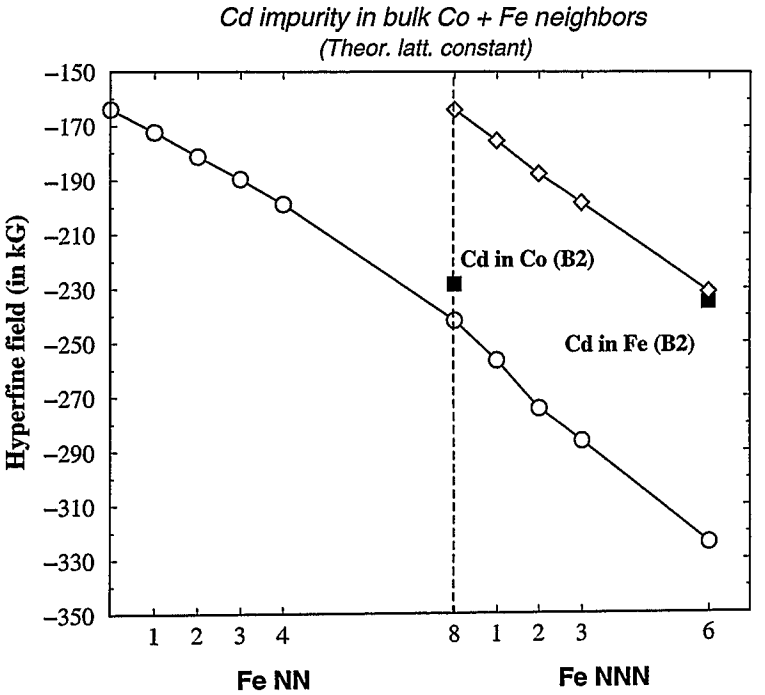

Figure 5.6: Cd *hff* in Co bulk matrix as a function of the progressive filling of the first two shells with Fe atoms.

The *hff* of Cd is plotted as a function of the number of Fe atoms in the first two shells, i.e. replacing one after the other the Co atoms in the first and second shell shells by Fe atoms; each point in Fig. (5.6) has been obtained by means of a self-consistent calculation, i.e. all the potentials for each configurations readjust until convergence is reached. The initial value refers to a single Cd in bulk *bcc* Co, i.e. $H_{hf} \equiv -165\,kG$. We then start to fill the $1st$ shell around the Cd impurity with Fe atoms. Replacing one by one the 8 Co NN atoms with Fe, we find out that

the "transferred" *hff* scales almost additively with the number of neighboring Fe atoms and reaches the value of $H_{hf} \equiv -242\,kG$ for the filled shell; the "additivity" characteristic of the *hff* was already proposed in the literature [AAB+90, EWG+87]. This value is still far away from what is expected from a Cd impurity in bulk *bcc* Fe, which from Fig. (5.4) should be around $H_{hf} \equiv -290\,kG$. Only starting by replacing Co in the *2nd* shell with Fe atoms the Cd *hff* increases further and reaches a value of $H_{hf} \equiv -320\,kG$. This value is higher than expected for Cd in bulk Fe, but this comes as no surprise; the reason is that the two shells of Fe around the Cd atom are still embedded in the Co environment, and therefore they have higher moments than in a real bulk calculations. Some additional contributions may come from additional Fe atoms in the third shell around the Cd, but these are one order of magnitude smaller then the ones arising from the first two shells, and they turn out to be more then compensated by the reduction in the *hff* due to decrease of the Fe moments in the first two shells. The *2nd* shell therefore induces a polarization on the Cd *s*-orbitals which has not only the same magnitude as the *1st* shell, but is even larger. In the *bcc* structure the two shells are at very similar distance from the central atoms, i.e. $r^{1st} = 0.866 a_{latt}$ vs. $r^{2nd} = 1 a_{latt}$; as we will find again in the next chapter the larger contribution from the *2nd* shell seems to be a characteristic of the *bcc* structure, and will appear also in the case of Fe or Co *hff* in Fe/Co dilute alloys. With this "two shells" model the larger induced *hff* for a Cd atom sitting in the Co1 layer at the (001) Fe/Co interface can be qualitatively explained, since the contribution from the Fe1 layer is given by 2 Fe NN + 2 Fe NNN in the (110) as opposed to the 4 Fe NN in the (001) interface, and 2 Fe NNN contribute, as evident from Fig. (5.6), more than 2 Fe NN.

One could argue that the contribution from the *2nd* shell should depend on the filling of the *1st* shell by Fe atoms, since the Fe moments should depend on the number of Fe atoms in the neighborhood. To check whether this is the case, I report in Fig. (5.6) (by open diamond symbols) the Cd *hff* obtained by filling only the *2nd* shell with Fe atoms, but this time leaving the *1st* shell unfilled. The total contribution from the *2nd* shell is now smaller than before, i.e. $-67\,kG$, as opposed to $-82\,kG$ found in the case of filled *1st* shell; again, taking into account that only 6 NNN exist in comparison with the 8 NN, an Fe atom in the *2nd* shell contributes more than one in the *1st* shell.

In order to further verify this picture, I performed also Cd impurity calculations in substitutional position in Fe/Co alloy in the B2 structure, well known in the literature to be the stable ordered phase for Fe_xCo_{1-x} alloys with $x = 0.5$; in the B2 structure, as depicted in Fig. (5.7), Fe and Co atoms are arranged in two simple

cubic sublattices displaced from each other by half the cube diagonal. In the B2 structure an Fe (Co) atom is surrounded by 8 Co (Fe) in the $1st$ shell, and 6 + 12 Fe (Co) atoms in the $2nd$ and $3rd$ shells; a Cd probe atom in a substitutional Co position would therefore have the same surrounding (up to the $3rd$ shell) as the Cd with 8 Fe NN in bulk Co with $H_{hf} \equiv -242\,kG$.

The *hff* of Cd in a substitutional Fe position on the other hand should be comparable to the *hff* of the Cd with 6 Fe NNN (and no Fe NN) of $H_{hf} \equiv -231\,kG$, even if in this case the $3rd$ shell is differently filled; this should not influence much the results since the contribution of the $3rd$ shell is one order of magnitude less than the one one of the first two shells. The two hyperfine fields of Cd in Fe and Co substitutional positions in Fe/Co B2 (indicated as *Cd in Co (B2)* and *Cd in Fe (B2)* ordered alloy are shown in Fig. (5.4*b*) as filled squares. As predicted from the calculations for the dilute alloys the two *hff* have very similar values; if the $1st$ shell would have a much larger contribution than the $2nd$ one, then the *hff* value for Cd in Co (B2) would be much larger (in absolute value) that the one of Cd in Fe (B2), and clearly from (5.6) this does not occur.

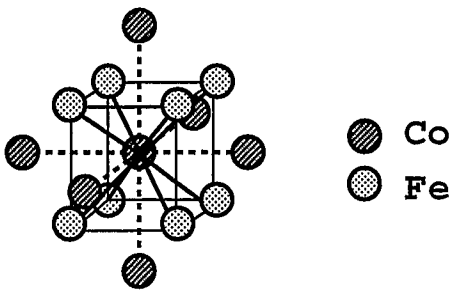

Figure 5.7: B2 structure assumed by the Fe/Co ordered alloy in the 50%-50% concentration regime.

Before proceeding to the comparison with the measured *hff*, in Fig. (5.8) I show the comparison between the Cd *hff* at the (110) Fe/Co interface for the theoretical and the experimental lattice constant of Fe. Because of the increase in the volume of the cell, the Fe moments, as discussed in the previous section, increase by about 10%; the Cd *hff* in bulk Fe instead increases of up to 30% of its value near the Fe bulk environment. The small changes in the Co moments leave the "transferred" *hff* unchanged, and Cd in Co "bulk" environment attains practically the same *hff* for both lattice constants. We can interpret this results also as a good estimation on how relaxations of the Fe and Co atoms around the Cd impurity would influence the calculated Cd *hff*. Relaxation of the Fe shells around heavy *sp* impurities, as extensively explained in ref. [KSP$^+$00, CH00], are always outwards and only relevant for the first two shells; for earlier *sp*-impurities the *hff* are increased due to lattice relaxations, as shown in Fig. (5.8). Since, moving from the theoretical to the experimental lattice constant, not only the first neighbors but all the atoms are more distant to each other, the volume increase is larger than for the relaxed structures presented in ref. [KSP$^+$00]; relaxation effects are therefore believed to

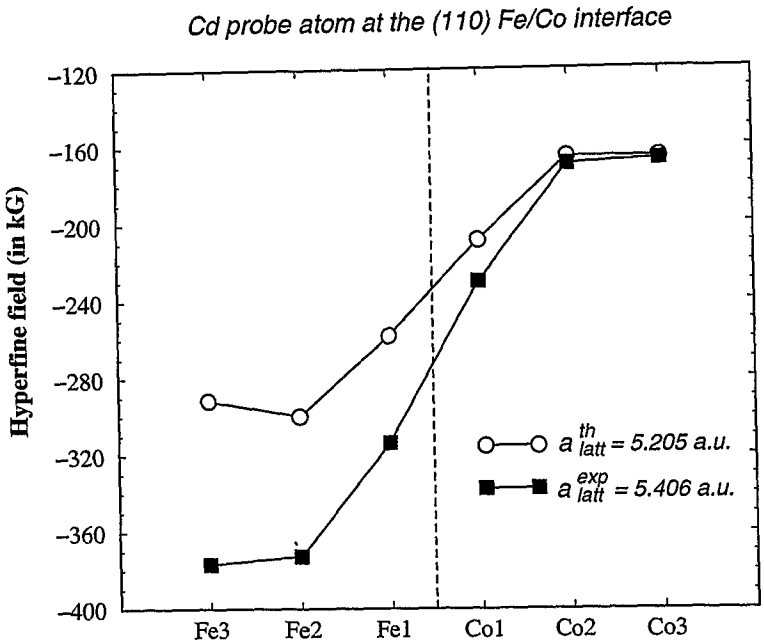

Figure 5.8: Comparison between the Cd *hff* at the (110) Fe/Co interface using the theoretical $a_{latt} = 5.205\, a.u.$ (empty circles) and experimental $a_{latt} = 5.406\, a.u.$ (filled squares) Fe lattice constant.

lead to *hff* values in between the two curves presented in Fig. (5.7).

(iii) Comparison with the Experiment

We can now compare with the measurements performed by Swinnen *et al.* [SMD+97]. In table 5.1 a summary of the Cd *hff* measured by the TDPAC experiment is presented. The Cd probe atoms were implanted into the Fe/Co multilayer structure and therefore are supposed to supply information for both the bulk Fe and Co region as well as for the interface region. Two main peaks in the Cd *hff* are observed and attributed to Cd in *bcc* Fe and Co bulk environment, with respectively $H_{hf} = -381\, kG$ and $H_{hf} = -161\, kG$. Two sharp (with nearly no dispersion in the frequency) satellites near each peak are also resolved and they are assigned to probe atoms either in Fe or in Co layers in plateaus near a *sharp interface*; their hyperfine fields (see table 5.1) are very close to the ones of the two main peaks. In addition to these sharp features, two broad distributions are found and, since their mean field are between the ones for Cd in Fe and Co bulk, they have been assigned to probe atoms in a mixed Fe/Co environment at *diffuse* parts of the interface.

For what concerns the two main peaks, the agreement with our calculations is very good since, from the calculations performed with the experimental lattice con-

TDPAC Exp.	Cd in Fe	Cd in Co
bulk	-381 kG	-161 kG
sharp interface	-387 kG, -398 kG	-156 kG, -172 kG
diffuse interface	-360 kG	-187 kG

Table 5.1: Assignment of the Cd *hff* peak and satellite measured by the TDPAC experiments of Swinnen *et al.* [SMD+97].

stant in Fig. (5.8), the *hff* of the Cd in bulk *bcc* Fe and Cd in bulk *bcc* Co retain respectively $H_{hf} = -377\,kG$ and $H_{hf} - 167\,kG$. In the case of the Cd *hff* in bulk Fe the agreement is somewhat fortuitous, since the high value is induced by a bulk Fe magnetic moment of $2.25\mu_B$ which is actually larger than the experimental moment of $2.2\mu_B$; it is nevertheless instructive to see that within an LDA calculation for the experimental lattice constant the agreement with experiments improves considerably. When one compares the *hff* of Cd probe atoms in Fe or Co layers at the Fe/Co "sharp" interface region on the other hand strong discrepancies are found; the shift from the "bulk" value to the "interface" value is of only several kG's in the experiment while it reaches $70 - 80\,kG$ in the *ab initio* calculations. The broad distribution found in the experiments and interpreted as arising from Cd in an interdiffused Fe/Co interface are on the other hand more shifted from the two bulk values. The main point arising from our calculations is that, being the *hff* driven by the very local environment, the main changes in the *hff* are expected in the first 2 layers on each side of the interface; since the magnetic configuration changes very rapidly from one layer to the other so also change the "transferred" *hff*.

Such abrupt changes in the Cd *hff* on the other hand, would be mitigated by the presence of some interdiffusion at the Fe/Co interface. This is indeed the case, for instance, in the cases depicted in Fig. (5.9). If a Co atom interdiffuses in the adjacent Fe layer, the *hff* of the Cd in the Co layer at the interface would diminishes (in absolute value) by several kG towards the Cd in "bulk" Co value. Satellite features which are several kG separated from the two main peaks, could therefore be attributed to Cd probe atoms in the presence of 3 or 4 interdiffused atoms.

I perfomed also total energy calculations to see whether interdiffusion at the Fe/Co interface is favoured energetically. The calculations predict that an exchange of an Fe-Co pair at the (001) interface layers requires an energy of about $0.1\,eV$ which is sufficiently low so that during epitaxial growth indeed strong interdiffusion is expected to take place. The two broad distributions observed in the experiments,

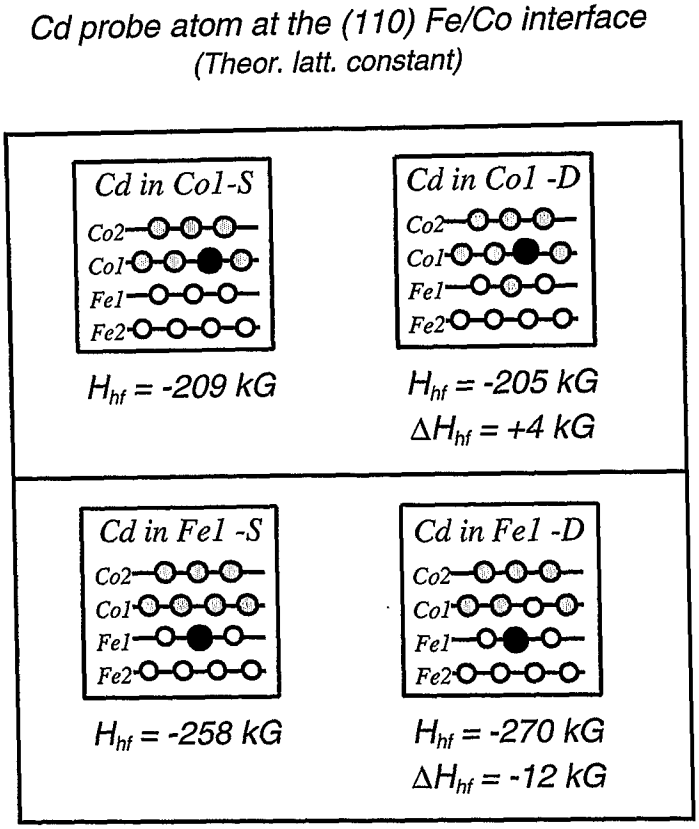

Figure 5.9: Cd *hff* at the sharp (110) Fe/Co interface and in presence of an interdiffused atom.

are therefore consistent with our calculations; they may arise from many slightly different microscopically environment around a Cd probe atom in the Fe1 (Co1) layer with some interdiffused atoms in the adjacent Co1 (Fe1) layer.

As a last test for the accuracy of our results, I investigated whether changing from a spherical (Atomic Sphere Approximation) to a full cell (Full Potential) treatment of the potentials leads to significant differences in the calculated hyperfine fields. In Fig. (5.10) I compare the results of the ASA and the FP calculations for the Cd at the (110) Fe/Co interface using the theoretical lattice constant. As evident from Fig. (5.10) the ASA calculations do not differ much from the FP ones. This means that for a Cd impurity the form of the potential is not crucial for a correct evaluation of the hyperfine fields. This was already observed by Korhonen *et al.* [KSP+00] where for all the elements at the beginning of the $5sp$ and $5sp$ series the FP results where compared with the ASA results of Akai *et al.* [AAB+90]. The ASA results presented in this work contain however what is believed to be the main reason for the improvement of the FP *hff*, i.e. the full charge density, which was not

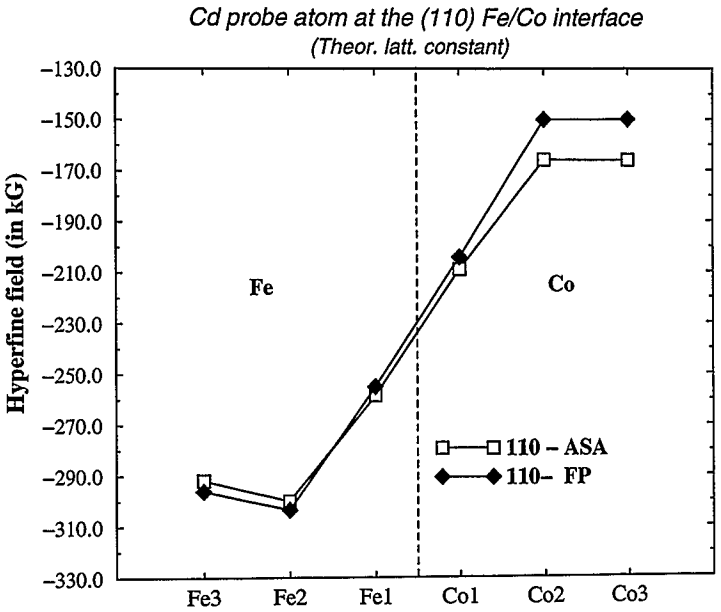

Figure 5.10: Comparison between the ASA and FP calculations for the Cd *hff* at the (110) Fe/Co interface

included in the ASA calculations presented in the work of Akai *et al.* [AAB+90].

(iv) Summary

We can summarize in the following the comparison with the experimental work of Swinnen:

- The calculated and "measured" magnetic moments profiles of the Fe/Co interface are, as discussed in the previous section, in strong disagreement; this discrepancy can be traced back to the "questionable" fitting procedure used in the experiments, which has its basis in the unreliable model for the hyperfine fields proposed by Stearns [Ste73].

- The results for the Cd hyperfine fields away from the interface compare rather well with the values for the Cd in a bulk Fe and bulk Co environment provided the experimental lattice constant is used in the calculations.

- For the ideal interface the Cd *hff* decreases in two more or less equal steps from the bulk Co to the bulk Fe value, in strong constrast to the interpretation of the experiments. The changes can be understood from the coordination changes of the number of NN and NNN.

- Since no well defined Cd *hff* for the Fe1 and Co1 positions are found in the experiment we conclude that the investigated interfaces are strongly interdiffused
- This is in line with the two broad distributions associated with Cd probe atoms at diffused interface found in the experiment, which can be simulated by means of many microscopically different environments with several Fe or Co interdiffused atoms.

5.3 Hyperfine fields in Fe/Co systems

This section aims to study the behaviour of the Fe and Co *hff* at the Fe/Co interface and in dilute and ordered FeCo alloys. As opposed to the case of a non-magnetic material, like Cd, the *hff* induced on a magnetic atom, e.g. Fe and Co, result from the interplay between two competing polarization mechanisms. Due to the spin polarized *d*-orbitals which lead to the local magnetic moment of Fe and Co, a "local' polarization is induced in the nuclear region to the *s*-orbitals. In addition to this local contribution, a "transferred" *hff* is induced, similary as it happens for the non-magnetic atoms, from the magnetic environment in which the atom is embedded. As explained extensively by Akai *et al.* [AAB+90] and Blügel *et al.* [BAZD87] for magnetic impurities in Fe and Ni hosts, the core contribution to the *hff* scales with the local moment with a negative proportionality constant; the valence *hff* has both a "local" and "transferred" contributions, the first scaling also with the local moment (but this time with a positive proportionality constant) and the latter being negative, i.e. opposite to the moments of the neighbors, for all the transition metal impurities studied.

Having in mind the above picture, Fe and Co are expected to show different behaviours regarding their total *hff* at the Fe/Co interface or more generally in Fe-Co systems. This becomes clear analyzing the magnetic moment profile at the Fe/Co interface plotted in Fig. (5.1). Since Fe is a "weak" ferromagnet, its magnetic moment is very sensitive to the environmnent and so is expected to be the "local" valence and core contributions to the *hff*. Instead the magnetic moment of Co is saturated, and remain constant moving towards the Co1 interface layer; therefore only the "transferred" polarization acting on the valence *s* orbitals induces the changes in the total Co *hff*. This peculiarity of Co will allow us to interprete the changes in the *hff* as arising only from the magnetic environment in which the Co atom is embedded in a very similar way as it was previously done in the case of the Cd atom.

This is indeed the case, as can be seen in Fig. (5.11), where the *hff* of Co and Cd impurities at the (001) and (110) Fe/Co interface are shown. For both orientations, the *hff* of the Cd and Co probe atoms show a similar trend, moving from the Co to the Fe side of the interface.

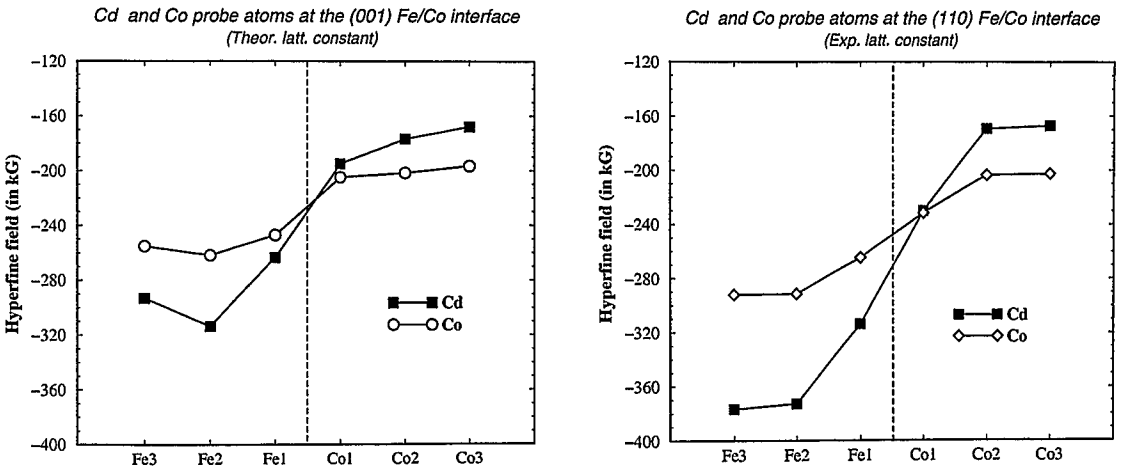

Figure 5.11: Comparison between the *hff* of Co and Cd impurity atoms at the (001) (left figure) and (110) (right figure) Fe/Co interface.

Since the (001) and (110) Fe/Co interfaces of Fig. (5.11) have been calculated respectively using the theoretical and experimental Fe lattice constants, we can observe how the *hff* at the Cd and Co atoms change with respect to the increase in the magnetic character of the neighboring atoms induced by the volume increase. On the Fe side a sensible increase for both Co and Cd *hff* is observed due to the larger magnetic moments of the surrounding Fe atoms, while less changes are found for the *hff* in the Co side due to the "saturated" Co magnetic moments. Due the large sensitivity to environmental changes induced by the large extent of the Cd valence *s*-orbitals with respect to the Co ones, the increase of the Cd *hff* is twice as much the one of the Co *hff*.

I will discuss in the following the *hff* profile at the Fe/Co interface and Fe-Co dilute alloys and investigate its origin; at the end of the section I will compare the results with the available Fe and Co *hff* measured by Mössbauer and Nuclear Magnetic Resonance (NMR) experiments.

Fe and Co *hff* at the Fe/Co interface

Let us examine now the *hff* profile at the (001) and (110) Fe/Co interface shown in Fig. (5.12) and Fig. (5.13), where the total as well the valence and core contributions

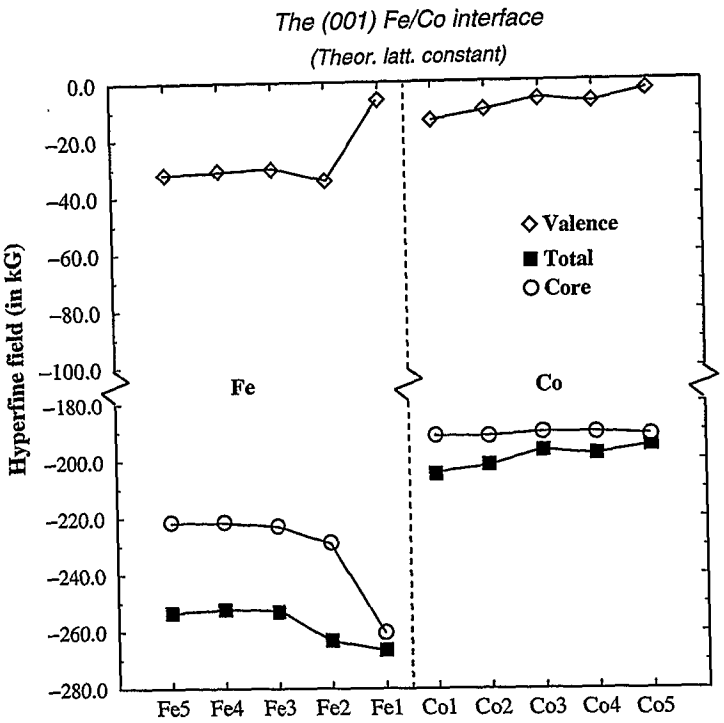

Figure 5.12: *Hff* profile at the Fe/Co (001) interface (LDA lattice constant); the squares are the total *hff*, circles and diamonds indicate respectively the core and valence contributions.

to the *hff* are shown; for both orientations the theoretical Fe lattice constant $a_{latt} = 5.205\, a.u.$ was used.

Let us discuss at first the behaviour of the Co *hff*. The core contribution to the *hff*, for both directions, remains constant approaching the interface with Fe to about $\sim -190\, kG$. Also the "local" contribution to the valence *hff* is constant and of positive sign, and, as we discussed previously, the changes in the Co valence *hff* are driven only by the negative *hff* induced by the neighboring atoms; this "transferred" *hff* increases (in absolute value) approaching the Co1 interface layer and is of the same order of magnitude for both the interface orientations. Since Co and Cd behave very much in the same way regarding their *hff*'s, it comes as now surprise that also the Co *hff* at the Co interface layer (Co1) is larger (in absolute value) in the (110) than in the (001) orientation, and as I will discuss in the next section it has its justification, similarly for the Cd, in the role of the second neighbors in the "transferred" polarization to the Co *s*-valence orbitals. The small oscillations observed for the (001) interface in the Co side are similar to the oscillations found for the Cd impurity and have the same justification in the small oscillation in the Co magnetic moments due finite size effects acting in the Co slab.

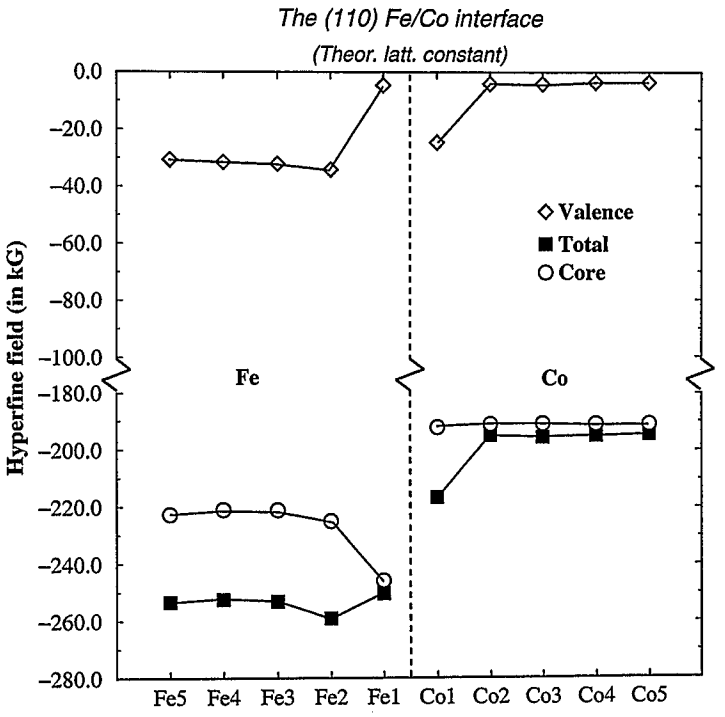

Figure 5.13: *Hff* profile at the Fe/Co (110) interface (LDA lattice constant); the squares are the total *hff*, circles and diamonds indicate respectively the core and valence contributions.

For what concerns the Fe *hff* at the Fe/Co interface, the interplay between both the core and valence contribution leads to the different behaviour of the Fe *hff* for the (001) and (110) interface orientations. The core contribution to the Fe *hff* follows (with a negative multiplicative constant) the total Fe magnetic moment and therefore increases approaching the interface region; since the (001) interface present a larger Fe1 magnetic moment than the (110), the core contribution is also larger. The valence contribution decreases from the value assumed in the "bulk" region, i.e. $\sim -30\,kG$, to almost zero at the Fe1 interface layer, and no sensible differences are observed for the two orientations. The total Fe *hff* at the (001) Fe1 interface layer is larger (in absolute value), i.e. $-266\,kG$, than the bulk Fe *hff* of $-253\,kG$, while it is slightly smaller, i.e. $-250\,kG$ for the (110) orientation; for the (001) interface the enhancement in the core polarization is able then to balance the drop in the valence contribution, while this does not happen for the (110) interface. When the valence *hff* at the Fe or Co layers is zero implies that the local positive and the negative transferred valence contributions are of the same size, and balance each other.

In Fig. (5.14) I show the calculated *hff* at the (110) Fe/Co interface choosing the experimental Fe lattice constant, i.e. $a_{latt} = 5.406 a.u.$; moreover I present the *hff* of

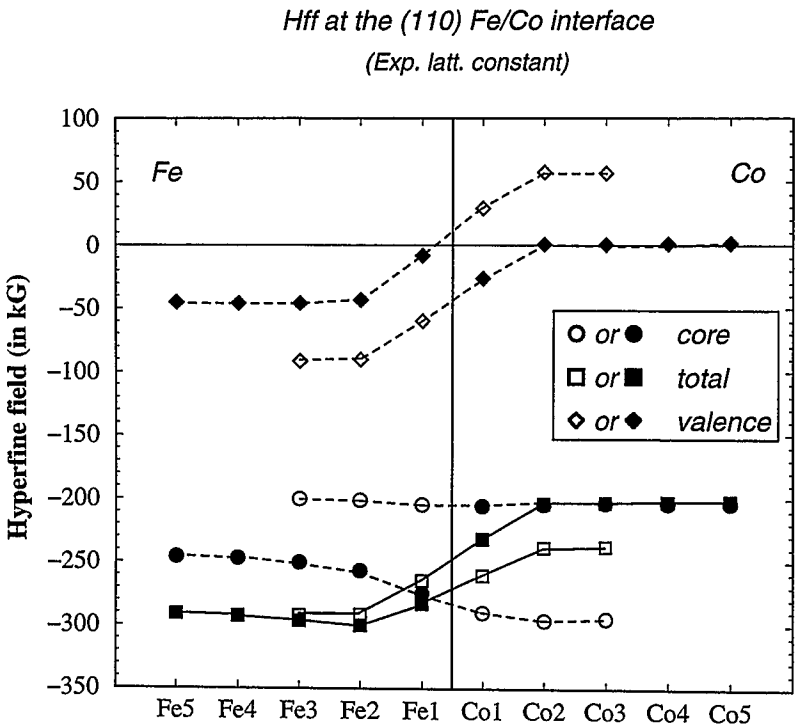

Figure 5.14: *Hff* profile at the Fe/Co (110) interface (Exp.lattice constant). The filled symbols are relative to the Fe (Co) *hff* in the Fe (Co) side of the interface, while open symbols are relative to Fe (Co) impurities that diffuse in the Co (Fe) side; as for figures (5.12) and (5.12) the squares are the total *hff* circles and diamonds indicate respectively the core and valence contributions.

Co (Fe) atoms which diffuse into the opposite Fe (Co) side of the interface. For what concerns the Fe *hff* at the Fe side of the interface, the enhanced Fe moments obtained by using the experimental lattice constant raises the negative core contribution of about i.e. $-30\,kG$; also the valence contribution is enhanced of about $-15kG$ in Fe layers away from the interface region. Also for the Co *hff* a small increase is detected of about $-10\,kG$ in the core contribution, while the valence contribution changes of only $2-3\,kG$.

The *hff* of a Co impurity which diffuses into the Fe layers at the Fe/Co interface, is, as already discussed for the Fig. (5.11), varying in a similar way as observed for the Cd impurity, since the Co moment is unchanged. *How are the hff of an Fe impurity changing when it diffuses into the Co side of the Fe/Co interface?*. As shown in Fig. (5.14), the core contribution has a further increase when an Fe atom moves into the Co slab, and reaches the maximum negative value already at the Co2 layer; this is obviously due to the increase of the Fe magnetic moment which

is for an Fe impurity in bulk *bcc Co* of about $M = 2.72\mu_B$, sensibly larger than the one of the Fe1 interface layer of $M = 2.52\mu_B$, or than the Fe in bulk Fe value, i.e. $M = 2.25\mu_B$. The valence contribution, on the other hand continues to decrease and actually becomes positive when the Fe atom diffuses into the Co slab and it reaches, in the Co2 layer, a value of $+57\,kG$, more than compensating the negative enhancement of the core contribution. The total Fe *hff* is found thus to decrease to $\sim -238\,kG$ into the bulk Co environment.

From Fig. (5.14), the valence contribution to the Fe *hff* is found to follow, up to a more or less constant shift, the valence contribution of the Co *hff*; this is indeed surprising since, as opposed to the Co *hff*, the valence contribution is now ruled by two different polarization mechanisms,"local" and "transferred" ones.

A qualitative explanation of the valence contribution to the *hff* at the Fe/Co interface is sketched in Fig. (5.15) and summarized in the following. The local contribution to the valence *hff* is, as well known in the literature [AAB+90], proportional and of the same sign to the local magnetic moment; the transferred contribution is negative (for the transition metals). For what concerns the Co valence *hff*, the two contributions should thus be of comparable intensity in order to cancel each other in the bulk Co environment, i.e. $H_{loc}(Co) \sim -H_{tr}(Co)$. Since the magnetic moment of Co remains constant throughout the interface, the local contribution to the valence *hff* is also constant; moving into the Fe layers, the variation in the total valence Co *hff* ($H_{tot}(Co)$) are therefore only due to the variations of the transferred *hff*. For the Fe the situation is complicated by the simultaneous changes in its magnetic moment. Let us suppose that the "transferred" *hff* ($H_{tr}(Fe)$) is, for the same magnetic environment, the same for the Fe and Co atoms; this is equivalent to assume that the wave functions of the two elements are polarized in he same way by the external magnetic moment. Thus since an Fe atom in Co environment does not induce a larger magnetic moment on the neighboring Co atoms, $H_{tr}(Fe)$ should have a similar value as $H_{tr}(Co)$ in the

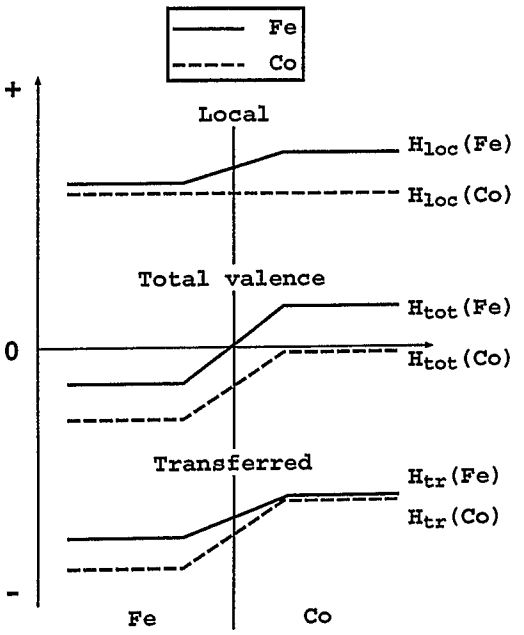

Figure 5.15: Scheme for the valence contribution to the *hff* in the Fe/Co interface.

bulk Co environment (right side of the picture). Instead $H_{tr}(Fe)$ should assume a smaller negative values than $H_{tr}(Co)$ moving towards the bulk Fe environment; the reason is that a Co atom induces a larger moment in the neighboring Fe atoms than an Fe atom itself and consequently the *hff* transferred from the neighboring atoms is also larger. The local contribution to the valence Fe *hff* ($H_{loc}(Fe)$), is expected to be larger than $H_{loc}(Co)$, because of the larger magnetic moment. Moreover it increases to higher positive values when the Fe atom moves into the Co side; this, again, is due to the progressive enhancement of the magnetic moment of the Fe atom ($2.72\mu_B$ in Co2 as opposed to $2.42\mu_B$ in the Fe1 layer and $2.25\mu_B$ in the "bulk" Fe3 layer). These local and transferred polarizations therefore induce a total variation on the valence Fe *hff* ($H_{tot}(Fe)$) which is again of the same order of magnitude as the one observed for the Co atom, i.e. $H_{tot}(Co)$, moving throughout the Fe/Co interface.

Dilute and ordered (B2) FeCo alloys

In order to understand the origin of the *hff* in the Fe/Co interfaces, I present, similarly as it was done for the Cd impurity, in Fig. (5.16) and (5.18) the *hff* of a Co (Fe) impurity atom in Co (Fe) matrix, as a function of the number of Fe (Co) atoms in the first two shells, i.e. replacing the Co (Fe) atoms with Fe (Co) ones.

Firstly let us discuss **the Co** *hff* in Fig. (5.16). The core contribution to the Co *hff*, as already observed in the case of the Fe/Co interface, remains constant to $\sim -190kG$ with respect to the number of Fe atoms in the $1st$ and/or $2nd$ shell. The valence contribution increases due to the larger total magnetic moment in the surrounding shells as a function of the number of Fe atoms; the filling of the $1st$ shell with 8 Fe NN induce a negative contribution to the *hff* of about $-30kG$, while 6 NNN Fe in the $2nd$ alone induces more than $-50kG$. Therefore, as observed for the Cd impurity atom, the $2nd$ shell induces a larger polarization to the local s orbitals than the $1st$ shell; actually almost 2/3 of the transferred *hff* to the Co atom is due to Fe neighbors in the $2nd$ shell. This unusual larger contribution of the $2nd$ shell with respect to the $1st$ one seems therefore to be a characteristic of the *bcc* structure for which the calculations were performed In the case of NiFe alloys [GE96] similar impurities calculations have shown an oscillatory behaviour of the induced *hff* to the central atom as a function of the shell number, with the contribution from the $1st$ shell being the largest one.

To check whether this unexpected large contribution from the $2nd$ shell is not a fictitious feature induced by some of the approximations adopted in our calculations, I present in Fig. (5.17) additional calculations of the *hff* induced on a Co atom as a

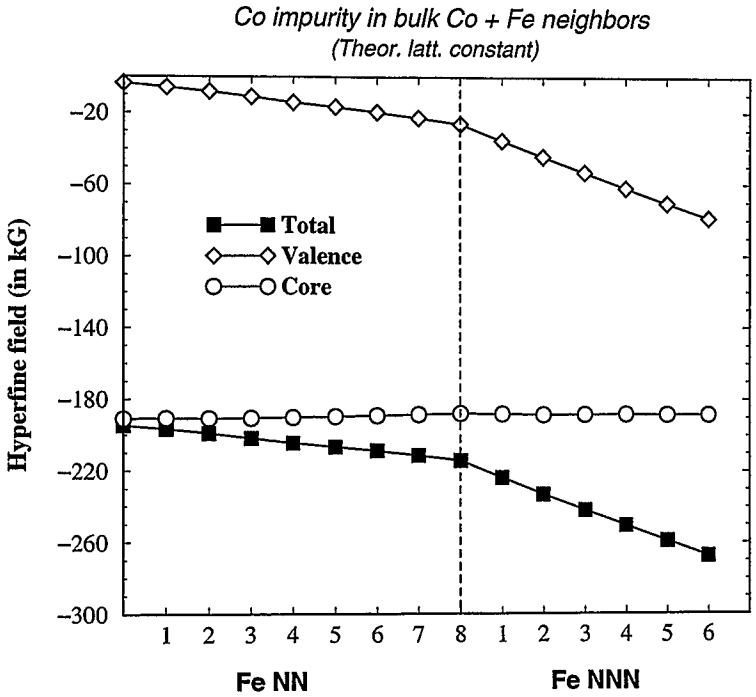

Figure 5.16: Co *hff* in bulk Co as a function of the number Fe atoms in the 1*st* (NN) and 2*nd* shell (NNN): the total (filled squares), core (open circles) and valence (open diamonds) contributions to the *hff* are shown.

function of the neighboring Fe atoms. In Fig. (5.17) I compare the total *hff* obtained by the filling of the 2*nd* shell with Fe atoms while keeping the 1*st* shell filled with Co (open circles); the total *hff* curve presented in Fig. (5.16) is also plotted for reference (filled squares). Similar to what we found for the Cd atom (see Fig. (5.6)), the induced *hff* per atom by the 2*nd* shell is smaller in the case of an empty (i.e. filled with Co atoms) 1*st* shell than for the filled (i.e. filled with Fe atoms) 1*st* shell; the contribution from the 2*nd* shell is again larger than the contribution of the 1*st* one. Another important feature which arises from the above calculations is that the contribution from the 2*nd* shell does not change sign depending of the filling of the 1*st* one; on this point I will come back later when the comparison with the experiments is carried out. In Fig. (5.17) I also show calculations for Co atom in the FeCo ordered B2 alloy (the one depicted in Fig. (5.7)). The B2 crystal was simulated by a cluster of 89 Fe and Co atoms (up to the 7*th* shell) in the B2 geometry embedded in a Co *bcc* environment. This calculations have a twofold goal; to check whether the adoption of a larger perturbed cluster could influence the picture of the *hff* discussed above, and to test the dependence of the induced *hff* on the matrix in which the first two shells are embedded in. The replacement of the NNN Co

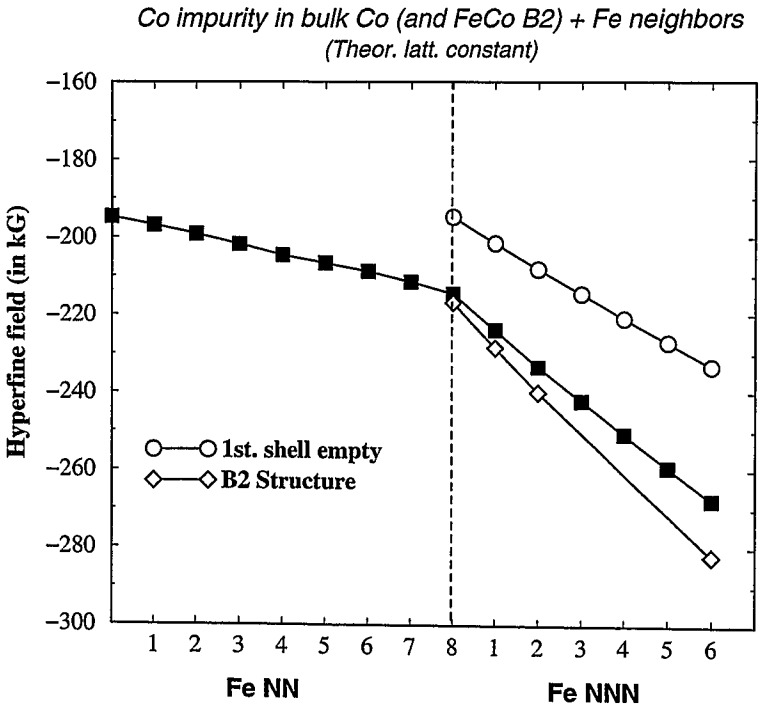

Figure 5.17: Total Co *hff* in bulk Co as a function of the number of Fe atoms in the $2nd$ shell in different configurations: Co in bulk Co with the $1st$ shell filled with Fe atoms (filled squares), Co in bulk Co $1st$ shell filled with Co atoms (empty circles), Co in FeCo B2 ordered alloy (open diamonds).

atoms with Fe atoms induces to the central Co atom an *hff* (open diamonds) which increase (in absolute value) even more rapidly as a function of the number of NNN Fe atoms as the two other cases depicted in Fig. (5.17).

The *hff* of an **Fe atom**, Fig. (5.18), has a more structured behaviour as a function of the number of the surrounding Co atoms. The presence of 8 Co NN atoms enhances the Fe core *hff* from $-222\,kG$ to $-288\,kG$, while the filling of the $2nd$ shell leaves the core contribution almost unchanged. The valence Fe *hff*, as observed also for the Fe/Co interface, becomes less and less negative and equal to zero after the filling of the $1st$ shell with Co atoms; with the additional filling of the $2nd$ shell the valence part reaches a positive value of $45\,kG$. Therefore the total *hff* increases until the $1st$ shell is filled, and afterwards decreases since the valence positive contribution is not anymore balanced by the negative core polarization. The maximum core contribution is assumed when an Fe atom has 8 Co NN, since this is the configuration with the largest Fe magnetic moment. We find again that the second shell plays a crucial role for the changes in the *hff* of the Fe central atom. Since the magnetic moment does not increase further after the filling of the $1st$ shell,

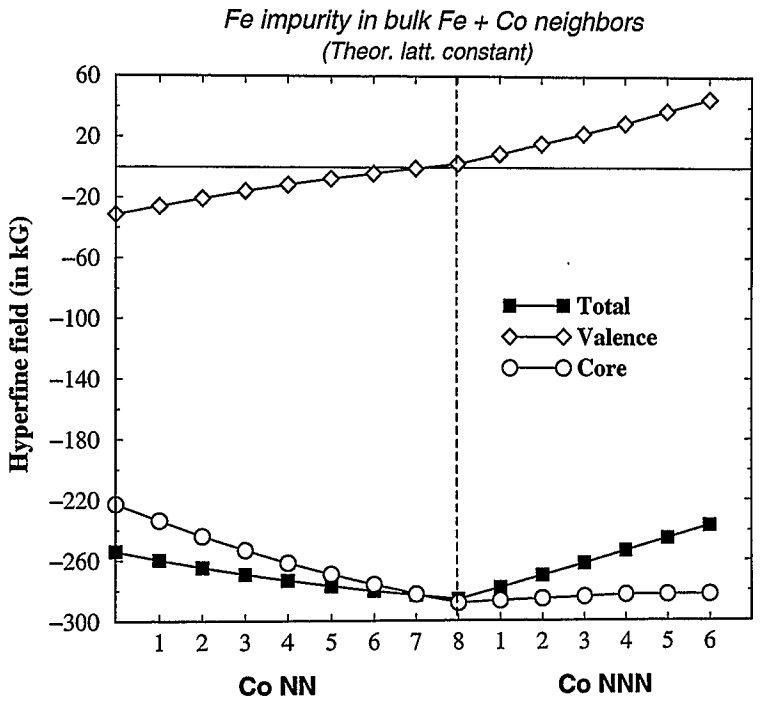

Figure 5.18: Fe *hff* as a function of the number of Co atoms in the 1*st* (NN) and 2*nd* shell (NNN): the total (filled squares), core (open circles) and valence (open diamonds) contributions to the *hff* are shown.

the variation in the Fe valence *hff* as a function of the filling of the 2*nd* shell is due only to the decrease in the transferred *hff* from the neighboring atoms.

We can now comment on the accuracy of the calculated Fe and Co *hff*. As already discussed previously the main source of error is the Local Density approximation on the exchange-correlation functionals. This leads to an underestimation, as we will realize in the next section comparing with the experimental values, of the core polarization mechanism, and therefore of the total *hff* for both Fe and Co atoms. Nevertheless this LDA "problem" turns out to be critical only for Fe, while for Co rather good agreement, at least for *bcc* bulk Co, is found with the experimental data.

It is worth-while to cite here the investigation presented by Battocletti *et al.* [BEA96] to see whether gradient correction to the LDA improves the core polarization mechanism; even if in some cases the use of the GGA enhances the core *hff* towards the experimental value, this was not found to be valid in general. The introduction of non-local functionals, on the other hand, have shown recently to improve remarkably the hyperfine fields of bulk Fe, Co and Ni [AK99, Kot98].

To answer the question whether the use of the experimental lattice constant would induce a different polarization mechanism from the first two shells, the calcu-

lation for the Co *hff* presented in Fig. (5.16) as a function of Fe neighbors is repeated in Fig. (5.19) using the experimental Fe lattice constant, i.e. $a_{latt} = 5.406 a.u.$.

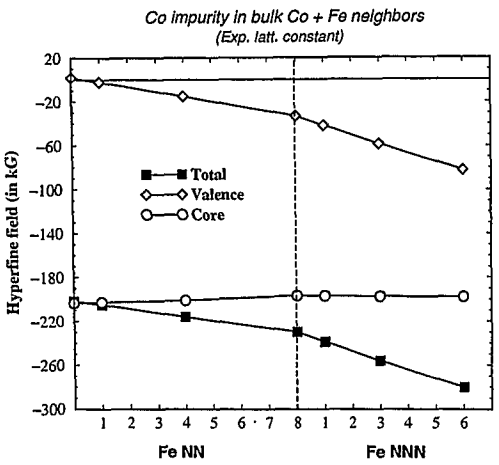

Figure 5.19: The same as Fig. (5.16) but using the experimental Fe lattice constant.

The induced *hff* are only slightly larger (more negative) due to the larger magnetic moments assumed by the Fe atoms induced by the larger volume, while the overall trend is unchanged.

Another possible source of errors is the SRA approximation used to calculate the hyperfine fields; in this approximation only the s orbitals give contribution to the *hff* via the Breit relativistic expression of the Fermi contact term [Fer30, Bre30], while the spin-orbit coupling is neglected. But, wherever an orbital moment exists, as is the case of Fe and Co elements, the d (or more general non-s) contribution to the *hff* is not anymore negligible. The inclusion of relativistic effects [ESG88, ESG89] have shown that indeed for Fe and Co a non-s contribution due to both orbital and dipolar terms exists, but, being of positive sign, it even enhances the disagreement with the experiments.

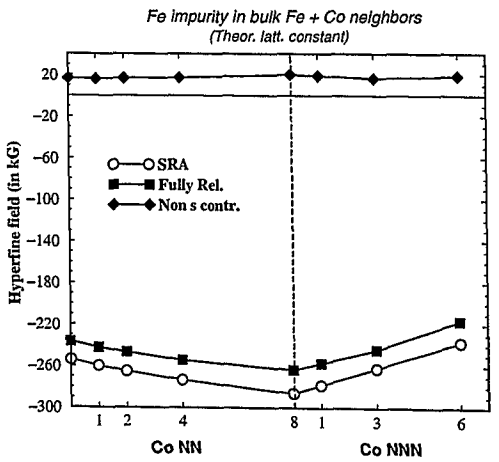

Figure 5.20: Comparison between SRA and fully relativistic calculations for the Fe *hff* in bulk Fe as a function of the number of Co atoms in the neighboring shells: the non-s contribution is explicitly plotted (filled diamonds).

Since the atoms in $1st$ and $2nd$ shells face from different angles the central impurity atom it was not clear a priori whether a shell-dependent non-s polarization mechanism could be induced to the central Co atom. To check this possibility in Fig. (5.20), the calculation for the Fe *hff* as a function of the Co neighbors (presented in Fig. (5.18)) is repeated by means of fully relativistic calculation [Non]; the SRA results (open circles) are compared with the fully rela-

tivistic ones (filled squares), and the non-s contribution to the valence *hff* is explicitly plotted (filled diamonds). The value of $\sim 20\,kG$ for the non-s contribution remains constant with respect to the number of Fe atoms in the $1st$ and $2nd$ shells, and is in agreement with the value found for bulk Fe [GE96], thus leaving the above discussions unchanged. This could have been guessed also by comparing the very similar values for the non-s contributions to the Fe *hff* in the case of bulk Fe [GE96], i.e. $H_{ns} = 14.6\,kG$, and Fe in the FeCo B2 ordered alloy [EWJP90], i.e. $H_{ns} = 17.4\,kG$, obtained by means of fully relativistic codes.

Comparison with the Mössbauer and NMR experiments

We can proceed now to compare the calculated Fe and Co *hff* with data available in the literature for Fe-Co bulk alloys. Rather many experiments were devoted in the past to the study of the Fe/Co alloys, which present, due to the co-existence of ferromagnetically "weak" (Fe) and "strong" (Co) elements, a very special magnetic behaviour as can be seen from the Slater-Pauling curve [DZAE91]. Disordered and ordered Fe_xCo_{1-x} alloys as a function of the concentration x, were investigated by means of heat capacity measurement [AEP59], ^{59}Co NMR experiments [Rub68, MSYN76] and ^{57}Fe Mössbauer experiments [HFP89], as well as studied by means of ab-initio methods [EWJP90].

For what concerns the comparison with other theoretical investigations, the *hff* of *bcc* bulk Fe and Co agree well with other SRA and Fully Relativistic results [Jan79, EWJP90, GE96]. Our results of Co atoms in *bcc* bulk Fe is also consistent with other theoretical studies [AAB+90], while no other theoretical investigation was found in the literature for Fe atoms in *bcc* bulk Co. Also the results for Fe and Co *hff* in the ordered B2 structure, at least regarding the s contribution to the total *hff*, are consistent with calculations performed by means of the fully relativistic LMTO code [EWJP90].

In table 5.2 and 5.3, the calculated and measured induced *hff* on Co and Fe atoms in different environments are summarized. The results listed in table 5.2 and 5.3 were obtained using the theoretical Fe lattice constant; the results obtained using the Fe experimental lattice constant, when present, are indicated between brackets.

We start comparing the results for the Co dilute alloys and bulk systems presented in table 5.2. As anticipated before, the value for the *bcc* bulk Co *hff* agrees well with the experimental values which was obtained by several groups [HBG+91, DJML93], by means of ^{59}Co NMR experiments. This *hff* for the *bcc* phase of Co can be unambigously assigned in the experimental investigations, since for the other two

	KKR results	Experiments (3)
Co in Co *bcc* bulk	-194 kG (-201 kG)	-198 kG
Co in Fe/Co B2 struct. (1)	-214 kG (-230 kG)	-289 kG
Co in Fe/Co B2 struct. (2)	-217 kG	
Co in Fe/Co B2 struct. (3)	-205 kG	
Co in Fe *bcc* bulk	-256 kG (-292 kG)	-287 kG

Table 5.2: Comparison between the calculated and measured *hff* of Co in different Fe-Co environment: the three different calculations for the B2 structure are explained in the text. The experimental results were taken from [DJML93, HBG+91] for the Co in *bcc* bulk Co, from [HFP89, JWP96] for the Co in FeCo B2 alloy, and from [Rub68] for the Co in *bcc* bulk Fe.

phases present in nature, i.e. *fcc* and *hcp*, the Co *hff* are respectively $H_{hf}^{fcc} = 219\,kG$ and $H_{hf}^{fcc} = 222\,kG$. Also the *hff* of a Co impurity in *bcc* bulk Fe agrees well with the experiments, especially if the experimental *bcc* Fe lattice constant is used, due to the better (larger) Fe magnetic moment. A large discrepancy is found instead for the value of Co in the FeCo B2 ordered alloy; on this point I will come back at the end of this section.

	KKR results	Experiments (3)
Fe in Fe *bcc* bulk	-253 kG (-291 kG)	-339 kG
Fe in Fe/Co B2 struct. (1)	-286 kG	-343 kG
Fe in Fe/Co B2 struct. (2)	-275 kG	
Fe in Fe/Co B2 struct. (3)	-271 kG	
Fe in Co *bcc* bulk	-229 kG (-238 kG)	-312 kG

Table 5.3: Comparison between the calculated and measured *hff* of Fe in different Fe-Co environment: the three different calculations for the B2 structure are explained in the text. The experimental results were taken from [Kra83] for the Fe in *bcc* bulk Fe, from [Ful91] for the Fe in FeCo B2 alloy, and from [DSR+94] for the Fe in *bcc* bulk Co.

For what concerns the Fe *hff*, all the values presented in table 5.3 are, as expected, underestimated; this is due to the well known failure of the LDA to reproduce correctly the *s*-core-polarization. Despite of this error the qualitative trend is reproduced correctly; the Fe *hff* has its maximum for the FeCo B2 ordered alloy,

since the magnetic moment and therefore the core contribution has its maximum for this structure (see also Fig. (5.18)). With the further increase of Co atoms in the surroundings of the Fe atom, the positive valence contribution is not anymore balanced by the core contribution and therefore the smallest *hff* is found for an Fe atom in *bcc* bulk Co environment. If the choice of the experimental Fe lattice constant improves considerably the agreement for the bulk Co and Co in bulk Fe *hff*, the difference between the bulk Fe and Fe in bulk Co *hff* agrees better with the experiments for the LDA Fe lattice constant. Once we are aware of the "error" which the LDA induces on the *hff*, we can conclude that a part for the value of Co in FeCo B2 ordered alloy, the *hff* presented in table 5.2 and 5.3 agrees reasonably well with the experiments.

Let us compare now more in detail the results for the Co *hff* in Fe-Co sytems with recent measurement obtained by ^{59}Co NMR experiments on FeCo alloys [JWP96, WJP+97]. In the work of Jay *et al.* [JWP96], the Co *hff* in $Fe_{1-x}Co_x$ alloys in the Co rich regime, i.e. $x = 0.5, 0.6$ and 0.6, have been measured; the ^{59}Co spectra were taken both as cast at $T = 800°C$, and after several weeks of annealing at lower temperature, ranging from $T = 400°C$ to $T = 550°C$ depending on the Co concentration. For the $50\% - 50\%$ alloy, the initial broad distribution observed in the spectra transforms into a well defined peak after annealing, which is assigned to Co atoms in FeCo B2 structure, with $H_{hf} = -289\,kG$. This is not reproduced in our theoretical calculations, and is indeed very puzzling since the other two *hff* values for Co in bulk Co and Co in bulk Fe in the *bcc* structure agrees very well with the experiments. For Co we have seen that the variation of the *hff* are only due to the transferred contribution coming from the different magnetic environments, since the local contribution due to the local magnetic moment is constant. In order to rule out possible errors in the calculations of the B2 structure, in table 5.2 and 5.3 are presented three different systems from which one could deduce the *hff* value of Co (Fe) in the FeCo B2 structure: (1) Co (Fe) in bulk Co (Fe) with 8 Fe (Co) NN atoms (see Fig. 5.16), (2) Co (Fe) as central atom in a 89 FeCo B2 cluster embedded in bulk Co (see Fig. 5.17), (3) a Co (Fe) atoms in the FeCo B2 bulk crystal. All the *hff* agree well with each other and also with other theoretical calculations performed by Ebert *et al* [EWJP90]. What about the large contribution obtained from the $2nd$ shell? Since the $2nd$ shell, as shown in Fig. (5.16) induces alone around $-60\,kG$ to the central Co *hff*, then the *hff* value of a Co atom in bulk Fe environment would reach, starting from the experimental Co in FeCo B2 value of $-289kG$, the value around $-350kG$ which is far beyond the experimental value of $-287kG$.

Now we can compare the physical picture arising from our calculations with the

one deduced from the FeCo bulk alloys measurements [JWP96]. In the $Fe_{.3}Co_{.7}$ alloy after annealing (ordering), several satellites are observed in the ^{59}Co spectra and assigned to Co atoms in different ordered environments; since the satellites are equally spaced and departing from the B2 peak at $-289\,kG$, they are assigned to Co in FeCo B2 structure with progressively missing Fe NN, i.e. Co plus 8 Fe NN (B2), Co plus 7 Fe NN, Co plus 6 Fe NN etc. Assuming the linear dependence of the Co *hff* with respect to the number of Fe atoms in the surrounding two shells (the contribution from higher shell is very small), a model is deduced from the satellite peaks observed in the different FeCo alloys spectra. We can summarize the model proposed by Jay *et al.* [JWP96] in the following:

1 Each Fe substituted for Co in the $1st$ shell (NN) adds about $-11\,kG$

2 The effect of Fe substituted for Co in the $2nd$ shell (NNN) depends on the number of Fe atoms in the $1st$ shell and varies from $+5\,kG/(\mathrm{Fe}NNN)$ in configurations 8 Co NN, to $-7\,kG/(\mathrm{Fe}NNN)$ in configurations with 8 FeNN.

The statement (1) is explicitly in disagreement with our theoretical findings, e.g. see Fig. (5.17), since we observe a sensibly smaller *hff* contribution from the $1st$ shell, i.e. -3 to $-4\,kG/(\mathrm{Fe}NN)$. Moreover also the statement (2) is in disagreement with the results presented in Fig. (5.17); the contribution from the $2nd$ shell, when filled with Fe, indeed presents some changes depending whether the $1st$ shell is filled with Fe or with Co atoms, but these changes are small and the contributions from the $2nd$ shell remains negative and no change in sign is observed. On the other hand while the model proposed by Jay *et al.* is able to explain the large value measured for the Co in the FeCo B2 alloy, it fails to reproduce the limit of a Co atom surrounded by Fe atoms, i.e. Co in bulk Fe, predicting an *hff* of $-320\,kG$ which is $32\,kG$ off the measured value of $-287\,kG$ [Kra83]. It is however surprising that if such a clear discrepancy with the experiments is found for the Co *hff* in FeCo B2 alloy, the calculated Fe *hff* instead is qualitatively correct for B2 structure, being predicted to show the larger (more negative) *hff* in comparison to the two other configurations presented in table 5.3, i.e. Fe in bulk Fe and Fe in bulk Co.

The same authors also studied the Co *hff* in Fe/Co multilayers by means of similar NMR experiments, and the peaks in the ^{59} Co spectra reinterpreted in light of the model proposed above for bulk alloys. It is beyond the scope of this work to compare in detail also with the results of Fe/Co multilayers, since the strong interdiffusion expected in the system makes the comparison between the idealized sharp interface and the real interdiffused one very difficult.

Summary

To conclude we can summarize the comparison for the Fe and Co *hff* in Fe-Co alloys between theory and experiment, where good agreement as well strong discrepancies are found.

- A very good agreement is found for the *hff* values of Co in *bcc* bulk Co, as well in *bcc* bulk Fe. One should however keep in mind that for *bcc* bulk Co a non-s contribution arises due to the orbital moment which is larger than for Fe, i.e. $H_{ns} = +50\,kG$ [GE96], which overcompensate the increase in the s valence contribution of $-20\,kG$, and leads to a somewhat worse agreement with the experiments.

- A qualitative agreement is also found for the Fe *hff*; the increase of the Fe *hff* from the Fe in *bcc* bulk Fe enviroment to the Fe in FeCo B2 ordered alloy, and the subsequent decrease towards the Fe in *bcc* bulk Co is correctly described and explained by the interplay between the core contribution and the valence contribution to the total *hff*. The absolute value of the Fe *hff* are nevertheless systematically underestimated due to the failure of the LDA in reproducing the s core polarization mechanism.

- The main discrepancy is relative to the *hff* of Co atoms in the FeCo B2 ordered alloy; in all the calculations performed to simulate the B2 structure, the Co *hff* was several tens of kG's away from the value found in the experiments.

- From the measured spectra, a model is deduced regarding the origin of the Co *hff* as a function of the Fe atoms in the $1st$ and $2nd$ shells; the larger contribution is assigned to the $1st$ shell while the $2nd$ shell contributes with both positive or negative sign depending on the filling of the $1st$ shell. This is also in strong disagreement with the picture arising from our calculations. For the *bcc* structure, a large contribution from the $2nd$ shell in observed, significantly larger than the one of the $1st$ shell; moreover no change in the sign is predicted from the atoms of the $2nd$ shell of atoms as a function of the filling of the $1st$ shell.

At the present time, it is not clear whether the inclusion of non-local contributions to the exchange-correlation functionals, e.g. by means of the OEP method, could improve the comparison between theory and experiments regarding the Co *hff* in the FeCo B2 ordered alloy; since these kind of calculations are still in an early stage [AK99, Kot98] this question remains at present unanswered.

Chapter 6

Vicinal surfaces and magnetic rows

In this chapter I present calculations of vicinal surfaces and $4d$ monoatomic rows on Ag vicinal surfaces. The magnetic moments of the monoatomic rows are discussed and compared with the results existent in the literature for finite-length chains, adatoms, and monolayers of $4d$ elements on the Ag(100) surface; moreover at the end of the chapter I discuss the stability of the antiferro- vs. ferro-magnetic solutions by means of total energy calculations. Due to the extreme computational demand of the calculations, the following results can be considered as a first challenging test for the N-scaling behaviour of the SKKR method.

6.1 High Miller index surfaces

In this section I give a brief description of the notation used in the literature to characterize the "high Miller index" surfaces, known also as *vicinal surfaces.* Since in the next sections I will present results for *fcc* Ag substrates, I limit the discussion to the *fcc* crystals. In the following I adopt the notation proposed by Van Hove and Somorjai [HS80], and refer to this article for a detailed discussion of *fcc* high-index surfaces.

Low Energy Electron Diffraction (LEED) studies reveal that, if a crystal is cut along a high index plane, the obtained faces exhibit an ordered array of periodic steps of mono-atomic height that separate atomic terraces. I have sketched in Fig. (6.1) the simple case of a 1-dimensional surface with Miller indices (h, k) of a 2-dimensional crystal; the stepped surface shows terraces of low Miller indices (h_t, k_t), and mono-atomic-height step faces which can also be characterized by low Miller indices (h_s, k_s). Each low-index piece of a surface we shall call "microfacet".

If we consider the more difficult case of a 3-dimensional crystal, an arbitrary

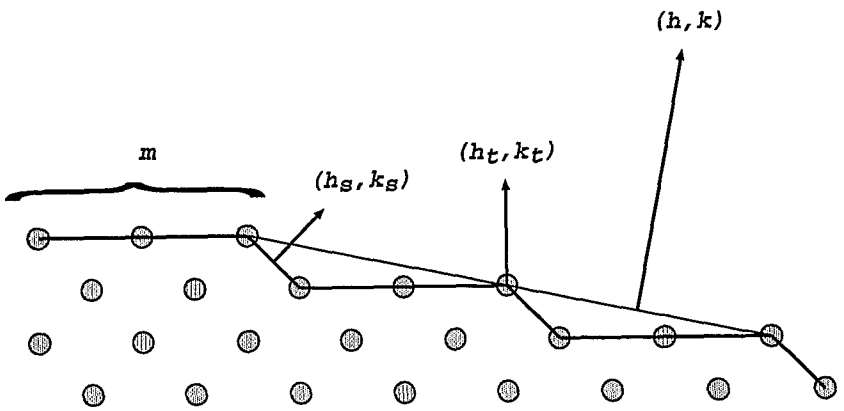

Figure 6.1: Schematic picture of a vicinal surface (h,k) in 2 dimension; the vectors represent, in the microfacet notations, the Miller indices of the vicinal plane, of the terrace and of the step atoms.

surface can be decomposed uniquely in terms of three microfacets. The vicinal surfaces present often kinks at the step edges (*kinked surface*) or additional step structures at the terraces (*stepped stepped surface*). If we restrict ourself to the vicinal surfaces with Miller indices (hkl) that have a common step orientation $(h_s k_s l_s)$, but variably-sized terraces of fixed orientation $(h_t k_t l_t)$, we can write the following microfacets decomposition

$$(h,k,l) = m_t \times (h_t,k_t,l_t) + (h_s,k_s,l_s) \tag{6.1}$$

where m_t represents the size of the terrace. Moreover if we restrict the study to surfaces with Miller indices (hkl) which have no kinks, either two of the three indices are equal or one of them has to vanish.

Keeping these rules in mind, I present in table 6.1 the classes of high Miller index surfaces for an *fcc* crystal, with terraces oriented in one of the low Miller index directions, i.e. (100), (110) and (111), together with their microfacet decomposition; the classes listed in table 6.1 present normal stepped surfaces without kinks and without stepped terraces.

This microfacet decomposition of the vicinal surfaces provides us of a new nomenclature, which becomes very usefull if we want to point the attention to the faceting of the steps atoms. For instance the *fcc* (331) vicinal surface, which belong to the class of vicinal surfaces with Miller indices $(m,m,m-2)$ with (111) terrace orientation, can be decomposed in microfacets and characterized by the "step notation" $3(111) \times (111)$ where 3 is the number of atom in the terrace, the first set of low Miller indices characterizes the terrace orientation and the second characterizes the faceting of the step edges. In table 6.1 the step notation for the different classes of vicinal surfaces is also given.

(hkl)	Microfacet decomposition	Step notation
fcc (100) terrace		
$(2m-1,1,1)$	$2m \times (100) + 1 \times (\bar{1}11)$	$m(100) \times (111)$
$(m+1,1,0)$	$m \times (100) + 1 \times (110)$	$(m+1)(100) \times (110)$
fcc (110) terrace		
$(2m-1,2m-1,1)$	$2m \times (110) + 1 \times (\bar{1}\bar{1}1)$	$m(110) \times (111)$
$(m+1,m,0)$	$m \times (110) + 1 \times (100)$	$(m+1)(110) \times (100)$
fcc (111) terrace		
$(m,m,m-2)$	$(m-1) \times (111) + 1 \times (11\bar{1})$	$m(111) \times (111)$
$(m+2,m,m)$	$m \times (111) + 2 \times (100)$	$(m+1)(111) \times (100)$

Table 6.1: Classes of vicinal surfaces for an *fcc* crystal; for each vicinal surface family the microfacet decomposition and the step notation is given.

The concept of "vicinal surface" will be used in the next sections as follows. Let us consider in Fig. (6.2*a*) a slab of material composed of N layers tilted in an high Miller index direction and being embedded in some vacuum layers; the surface layer turns out to be composed by an ordered array of monoatomic rows which point along a direction perpendicular to the picture's plane. A "vicinal" slab represents therefore the most natural template for the study of infinite 1-dimensional structures.

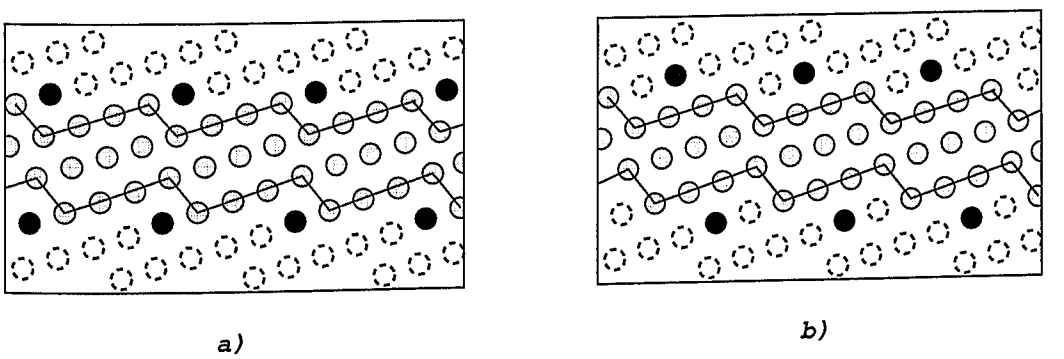

Figure 6.2: *a*) Monoatomic rows at the step edge position ; *b*) Monoatomic rows at a terrace position.

If we place an overlayer on a high Miller index substrate, we "decorate" each step edge of the substrate with an infinite monoatomic row. Inserting some additional vacuum layers (see Fig. (6.2*b*)), between the substrate and the overlayer we can move the rows away from the step edges towards the center of the terraces; moreover if we place on the substrate a number of overlayers equal to the number of atomic rows

in the terraces, we obtain a full stepped monolayer coverage of the substrate. We can therefore study the properties of the monoatomic rows at different step edges simply by changing the substrate orientation, i.e. choosing one of the classes listed in table 6.1; the choice of the particular vicinal surface, which by means of Eq. 6.1 coincides with the choice of the size of the terraces, will be driven by two practical necessities.

- In first place, the number of atomic rows m_t which compose the terraces should be sufficiently large to sufficiently suppress the step-step interactions, which can lead to some inaccuracy in the calculated electronic and magnetic properties at the step edges.

- Secondly m_t has to be suffiently small because the computational effort in the calculation increases with the width of the terraces. This becomes evident when one looks at the shape of the matrix M introduced in section 4.4 for these systems; since the interlayer distance between the "vicinal layers" decreases proportional to $\frac{1}{m_t}$ (while the angle between the vicinal orientation and the terrace orientation decreases with the width of the terraces) the reference structure constants will couple a larger number of layers, increasing the number N_P of layers in each Principal Layer (PL). The number N_P depends on the orientation but also on the size of the TB-cluster so that a generalized formula connecting N_P with the class of vicinal surfaces is not possible. For example if the TB-clusters are considered up to the second neighbour shell (19 atoms), $N_P = 8$ for an *fcc* (410) vicinal surface, and $N_P = 10$ for an *fcc* (510) vicinal surface having one atomic row more in the terrace; the required computing time for the calculation of the diagonal elements of M^{-1}, needed in the self-consistency procedure, increases as N_P^2.

6.2 Step edges on the *fcc* (100) terrace: Cu and Ag step energies

Since we are mainly interested in *fcc* subtrates which present terraces with (100) orientation, let us discuss in more detail the morphology of the *fcc* (100) terrace. As shown in Fig. (6.3), on the *fcc* (100) terrace two different kinds of step edges exist; I indicate them, following the "step notation" introduced in the previous section, as (100) × (111) and (100) × (110). The (100) × (111) step is close-packed, i.e. the atoms in the step edge are nearest neighbours (NN), with (111) faceting, while the

(100) × (110) is an open step, i.e. the step atoms are second neighbours (NNN), with (110) faceting. The two classes of vicinal surfaces which cut the crystal along these step edges, are the $(2m-1,1,1)$ and the $(m+1,1,0)$ one, with respectively m and $(m+1)$ atoms wide terraces.

The coordination number n_c is different for the two step edges. An atom sitting in the close-packed (100) × (111) step has 4 NN in the substrate layer below and 3 NN at the terrace positions, i.e. $n_c^{(111)} = 7$, while at the open (100) × (110) step, it has 4 NN in the substrate layer but only 2 NN in the terrace, i.e. $n_c^{(110)} = 6$.

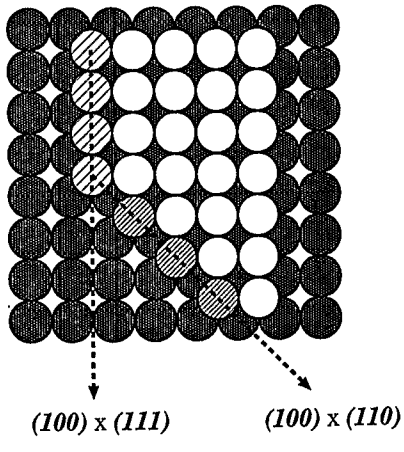

Figure 6.3: Step edges on the (001) surface

Using a simple broken bonds model, we obtain that in order to create the (100)×(111) step we have to break 5 of the 12 bonds in the first shell, while for the (100) × (110) step 6 bonds have to be broken; the (100)× (111) step should therefore be more stable than the (100) × (110). This is indeed in agreement with the experimental observations that (111)-faceted steps are preferentially formed in thermal equilibrium [TAK94].

The stability of the steps is thus related to the excess step energies. Since, as we saw in section 4.6, reliable surface energies can be calculated by means of the SKKR method, and since the calculation of the step energies can be traced back to the calculation of the surface energies of the relative vicinal surfaces, I present in the following the calculation of the (100)×(111) and (100) × (110) step energies for Cu and Ag *fcc* crystals. As discussed by Vitos *et al.* [VSK99], the energy per atom of a step edge on a certain terrace, can be calculated from the following equation

$$E_{\text{step}} = \lim_{m_t \to \infty} [E_{\text{surf}}^{\text{vicinal}} - (m_t - 1)E_{\text{surf}}^{\text{terrace}}] - f_{\text{step}} E_{\text{surf}}^{\text{terrace}} \tag{6.2}$$

where $E_{\text{surf}}^{\text{vicinal}}$ is the surface energy per atom of the high Miller index surface which cuts the crystal along the desired step edges, and $E_{\text{surf}}^{\text{terrace}}$ is the surface energy of the surface with the same low Miller indices as the terrace. This formula is obtained by simple arguments comparing the different unit areas that the high and low index surfaces present in the plane. The factor f_{step} in Eq. (6.2) corrects the fact that the step may not arise at a right angle from the terrace. The limit $\lim_{m_t \to \infty}$ in the above equation indicates that the considered vicinal surface has to contain a number m_t

of atoms in the terrace sufficiently large in order to suppress step-step interactions. For the case under interest, I have choosen the *fcc*(711) and *fcc*(410) (see Fig. (6.4)) vicinal surfaces, which present terraces of 4 atomic rows, i.e. $m_t = 4$; f_{step} has for these two steps the values $f_{(100)\times(111)} = \frac{1}{2}$ and $f_{(100)\times(110)} = 1$. These two vicinal surfaces will be discussed in more detail in the next section.

Cu Step energies (in eV/atom)		
Step type	SKKR	LMTO-GF (Vitos *et al.*)
(100) × (111)	0.228	0.200
(100) × (110)	0.436	0.363

Ag Step energies (in eV/atom)			
Step type	SKKR	LMTO-GF (Vitos *et al.*)	PSEUDOPOT. (Yu *et al.*)
(100) × (111)	0.160	0.158	0.130
(100) × (110)	0.288	0.231	0.156

Table 6.2: Cu and Ag step energies for (100) × (111) and (100) × (110) step edges; for comparison with the literature, the results obtained by means of the LMTO-GF and pseudopotential methods are included [VSK99, YS97]. In order to simulate the two step edges, the *fcc* (711) and (410) vicinal surfaces have been used; the terraces, 4 atomic rows wide, are sufficiently large to suppress possible step-step interactions.

In table 6.2 I show the results for the Cu and Ag step energies comparing with two sets of *ab initio* calculations existent in the literature, obtained by means of the LMTO-GF method [VSK99] and by means of the pseudopotential technique [YS97]. The SKKR and the LMTO-GF step energies were obtained, as for the related surface energies in section 4.6, for the experimental and GGA lattice constants respectively; for the Ag step energies both the KKR and LMTO results differ sensibly, especially for the open step, from the pseudopotential results, since these last results were obtained allowing the step atoms to relax from their ideal positions. As mentioned by Vitos *et al.* [VSK99], the relaxation at step edges are believed to influence more considerably the step energies than the surface energies, and changes up to $20-25\%$ have to be expected. Another important point to mention, is that the present results were obtained by means of non relativistic calculations while the results of Vitos *et al.* were obtained using the scalar-relativistic approximation. Therefore the agreement

between the SKKR and the LMTO-GF step energies is slightly better in the case of Cu substrates than for the Ag substrates; for heavier elements relativistic effects become more and more important, and they have to be included in order to obtain accurate total energies.

In order to check whether step-step interactions are present for the choosen vicinal surfaces, convergence tests with respect to the numbers m_t of rows in the terrace have been performed. Calculations for the *fcc* (410) and *fcc* (510) Ag vicinal surfaces with 4 and 5 atomic rows yield practically identical results for the Ag (100) $\times$ (110) step energies, i.e. $E^{110}_{step} = 0.288eV/\text{atom}$ for the (410) and $E^{110}_{step} = 0.285eV/\text{atom}$ for the (510) vicinal surfaces. Thus the results for the step energies presented in table 6.2 are converged with respect to the terrace width.

6.3 The *fcc* (711) and (410) vicinal surfaces

In this section I discuss in more detail the results for the Ag (711) and (410) vicinal slabs used to derive the step energies presented in the previous section; similar slabs but with a thinner Ag substrate will be used for the monoatomic rows calculations. The lattice constant of Ag was choosen to be the experimental one, $a_{latt} = 7.78\,a.u.$. Because of the very small interlayer distance, many more layers were considered in comparison to the low Miller index surfaces, in order to reach a good Ag bulk in the middle of the slab. The slabs are composed of 40 layers, 28 Ag layers in the substrate and 6 vacuum layers at each side of the substrate. The vicinal slabs present very open surfaces; as a consequence of that, the area of the 2D-Brillouin zone is smaller than in the case of low-index surfaces. However at the same time the asymmetry between the periodicity along and perpendicular to the row direction leads to a reduction of the symmetry in real and reciprocal space; for instance in the case of the two vicinal surfaces under consideration, only the mirror symmetry with respect to a plane perpendicular to the row axis and the inversion symmetry hold and therefore the irreducible part of the BZ in only $\frac{1}{4}$ of the whole 2D-BZ (compared to $\frac{1}{8}$ for the (100) surface).

In order to predict roughly the number of $q_{||}$-points needed for an accurate sampling of the Brillouin zone, one can compare with the case of the low index surfaces. For a correct BZ sampling the choosen $\mathbf{q}_{||}$-point mesh has to be fine enough to integrate correctly the peak structures that the Green's functions present especially near the real energy axis. If we compare the $\mathbf{q}_{||}$-point density for the high and low index Brillouin zones, in the case of high-index surfaces with Miller indices (hkl)

The Ag(711) slab

A_{2D-BZ} (unit of $[\frac{2\pi}{a}]^2$)	N. of symm.	N of $q_{\|\|}$ pts (in the contour)	N_P	d_z (unit of a_{latt})
$\simeq 0.5601$	4	43	8	$\simeq 0.1400$

Layer N.	s	p	d	f	sum	Total energy (in Ry)
Vc+6	0.0022	0.0017	0.0004	0.0000	0.0045	-0.00194
Vc+5	0.0031	0.0021	0.0005	0.0001	0.0060	-0.00248
Vc+4	0.0448	0.0387	0.0181	0.0085	0.1102	-0.06110
Vc+3	0.1157	0.0867	0.0379	0.0175	0.2579	-0.13320
Vc+2	0.1191	0.0864	0.0380	0.0175	0.2612	-0.13492
Vc+1	0.1630	0.1158	0.0506	0.0225	0.3521	-0.17412
Ag S	0.6187	0.3310	9.6827	0.0434	10.6759	-10390.09356
Ag S-1	0.6215	0.3941	9.6776	0.0503	10.7436	-10390.14788
Ag S-2	0.6149	0.3953	9.6729	0.0503	10.7336	-10390.15397
Ag S-3	0.6280	0.5163	9.6611	0.0638	10.8693	-10390.24268
Ag S-4	0.6292	0.6191	9.6669	0.0776	10.9929	-10390.32241
Ag S-5	0.6326	0.6197	9.6649	0.0780	10.9953	-10390.32361
Ag S-6	0.6379	0.6206	9.6619	0.0780	10.9986	-10390.32614
Ag S-7	0.6396	0.6156	9.6639	0.0789	10.9981	-10390.33067
Ag S-8	0.6355	0.6242	9.6594	0.0787	10.9980	-10390.33532
Ag S-9	0.6390	0.6241	9.6586	0.0787	11.0005	-10390.33482
Ag S-10	0.6402	0.6209	9.6603	0.0787	11.0002	-10390.33378
Ag S-11	0.6429	0.6167	9.6617	0.0787	11.0001	-10390.33249
Ag S-12	0.6431	0.6168	9.6618	0.0787	11.0006	-10390.33193
Ag S-13	0.6422	0.6185	9.6609	0.0787	11.0004	-10390.33237
Ag bulk	0.6409	0.6189	9.6613	0.0787	11.0000	-10390.33206

Table 6.3: The *fcc* Ag (711) vicinal slab. In the upper table the area of the 2D BZ, the number of symmetries used in the reciprocal space, the number of $q_{||}$ pts. used for contour energies, the number N_P of layer in each PL and the interlayer distance are listed. In the lower table the *s p d f* and total charges together with the total energies are listed for the upper half of the slab and for the bulk *fcc* Ag crystal.

The Ag(410) slab

A_{2D-BZ} (unit of $[\frac{2\pi}{a}]^2$)	N. of symm.	N of $q_{\|\|}$ pts (in the contour)	N_P	d_z (unit of a_{latt})
$\simeq 0.4851$	4	43	8	$\simeq 0.1212$

Layer N.	s	p	d	f	sum	Total energy (in Ry)
Vc+6	0.0029	0.0021	0.0005	0.0001	0.0057	-0.00233
Vc+5	0.0210	0.0185	0.0087	0.0041	0.0525	-0.02853
Vc+4	0.0782	0.0614	0.0273	0.0128	0.1799	-0.09301
Vc+3	0.1135	0.0870	0.0381	0.0175	0.2563	-0.13113
Vc+2	0.1235	0.0899	0.0390	0.0177	0.2702	-0.13645
Vc+1	0.2022	0.1400	0.0611	0.0271	0.4305	-0.20288
Ag S	0.5973	0.2802	9.6855	0.0373	10.6004	-10390.05756
Ag S-1	0.6209	0.3957	9.6785	0.0501	10.7454	-10390.14274
Ag S-2	0.6180	0.3973	9.6722	0.0503	10.7380	-10390.15692
Ag S-3	0.6230	0.4591	9.6619	0.0570	10.8011	-10390.20354
Ag S-4	0.6271	0.5731	9.6608	0.0704	10.9316	-10390.28241
Ag S-5	0.6308	0.6170	9.6680	0.0776	10.9936	-10390.32172
Ag S-6	0.6358	0.6199	9.6632	0.0780	10.9971	-10390.32416
Ag S-7	0.6407	0.6148	9.6645	0.0782	10.9983	-10390.32609
Ag S-8	0.6389	0.6182	9.6630	0.0786	10.9988	-10390.33027
Ag S-9	0.6359	0.6249	9.6587	0.0788	10.9985	-10390.33415
Ag S-10	0.6392	0.6222	9.6599	0.0786	11.0001	-10390.33500
Ag S-11	0.6401	0.6215	9.6596	0.0787	11.0000	-10390.33361
Ag S-12	0.6429	0.6180	9.6611	0.0787	11.0007	-10390.33330
Ag S-13	0.6438	0.6167	9.6608	0.0789	11.0003	-10390.33203
Ag bulk	0.6409	0.6189	9.6613	0.0787	11.0000	-10390.33206

Table 6.4: The *fcc* Ag (410) vicinal slab. In the upper table the area of the 2D BZ, the number of symmetries used in the reciprocal space, the number of $q_{||}$ pts. used for contour energies, the number N_P of layer in each PL and the interlayer distance are listed. In the lower table the *s p d f* and total charges together with the total energies are listed for the upper half of the slab and for the bulk *fcc* Ag crystal.

vicinal to the (100) direction, the following relation holds,

$$\frac{n_{q_{||}}^{(100)}}{A_{2BZ}^{(100)} \,/\, N_{\text{symm}}^{(100)}} = \frac{n_{q_{||}}^{(hkl)}}{A_{2BZ}^{(hkl)} \,/\, N_{\text{symm}}^{(hkl)}}$$

which offers a good estimation of the number of $q_{||}$-points necessary to use in the self-consistency procedure, where N_{symm} and A_{2BZ} and $n_{q_{||}}$ are respectively the number of symmetries, the area of the 2D-BZ and the number of $q_{||}$ points in the irreducible part of the 2D-BZ.

I list in tables 6.3 and 6.4 for the *fcc* (711) and *fcc* (410) vicinal surfaces, together with the above parameters, the size of the Principal Layer N_P, the value of the interlayer distance d_z, the l decomposed, i.e. s, p, d and f, charges inside the Wigner-Seitz sphere together with the total charges and in the last row the results for a bulk Ag calculation performed by means of the SKKR program for 3D periodic systems. For the calculation of the *screened* structure constants, a TB-cluster which couples up to the $2nd$ shell (19 atoms) was considered. In the last column I report also the total energies per atom for the different Ag and Vacuum layers in the slab. The number of Ag layers which compose the substrates had to be suffiently large since, as discussed in section 4.6, a good bulk total energy in the middle layer of the substrate is the necessary condition for an accurate determination of the surface energies. As already discussed in the literature [Fei95, SS96] it turns out that, for the 4 atoms wide terraces, vicinal surfaces substrates with up to $6-7$ "low Miller index " layers have to be considered, which correspond to $24-28$ vicinal layers; for such slab thicknesses the total energies of the middle layers in the Ag substrate, as shown in tables 6.3 and 6.4, agree with the bulk values up to several tenths of mRy.

6.4 Magnetic $4d$ monoatomic rows

In the last decades many efforts have been devoted to the understanding of the effects of spatial confinement on the magnetic properties of ultrathin transition metal films [HOMW98]. Among all materials, the one which are on the borderline of magnetism are the more interesting to study, since they exhibit the largest and more unexpected changes regarding their magnetic properties. The $4d$ and $5d$ elements are perhaps the best candidates for such studies; nonmagnetic as bulk metals they were predicted to be magnetic as 2-dimensional monolayers, e.g. Tc, Ru, Rh, Os, Ir overlayers on the Ag(001) or Au(001) surfaces [Blü92a, Blü92b, WF92]. On the most extreme side of spatial confinement, i.e. as adatoms on surfaces, they indeed were predicted to

show on the Ag and Cu substrates large magnetic moments, which are of the same order of magnitude as the ones observed for $3d$ impurities [LSW+94] in the bulk.

While in the past many experimental methods have been used to observe ferromagnetism of monolayers, rather few of them have the necessary sensitivity to detect the magnetic moments of "surface impurities". Motivated by the unexpected theoretical foundings presented by Lang *et al.* [LSW+94], Bergmann and coworkers performed by means of the weak localization method several measurements for adatoms and clusters up to the monolayer regime of $4d$ elements on Ag anf Au substrates [SB96, BSLB96, BB97]. They succeded to detect a magnetic moment for Nb impurities on Ag and Mo impurities on Au, in agreement with the theory [LSW+94], whereas no magnetism was observed for the $4d$ monolayers. Even from the theoretical point of view the $4d$ elements showed more than one puzzling behaviour. The magnetic properties of $4d$ nanostructures (chains and clusters) on Ag [WSL+95] showed an oscillatory behaviour as a function of the size of the systems. Turek *et al.* [TKŠ+95] presented a possible explanation for the strong disagreement between theory and experiments for the Ru and Rh monolayers, showing that imperfections in the monolayers plane can reduce and even suppress the magnetic moments; a similar study for imperfect clusters [SHR+99] goes in the opposite direction, predicting in certain situations an increase of the $4d$ magnetic moments in the presence of imperfections.

If, as discussed briefly above, 0-dimension (impurities) and 2-dimensions (monolayers) $4d$ structures on noble metals have recieved considerable attention, very few works so far presented results for 1-dimensional systems, i.e. monoatomic rows. From the theoretical side, because of the computational effort needed to balance the loss of symmetries, this problem has only been tackled with semi-empirical methods rather than from an *ab initio* point of view. By means of tight-binding model Hamiltonians the Magnetic Anisotropy Energy (MAE) of finite length chains of $3d$ elements [DDP98], and the row-row magnetic interactions for Co row on Pd(110) [RIV00] has been reported. Very recently similar results for Rh monoatomic rows on Ag [BHS+00] have been presented. From the experimental point of view, only the modern techniques like Scanning Tunneling Microscopy (STM) [CLE93, Bes96, RHB+93] and Molecular Beam Epitaxy (MBE) together with real-time control of the deposition stage obtained by thermal Energy Atom Scattering (TEAS) [BKMK98, GBB+00a, DCE+00], provided recently the tools for the realization of such 1-dimensional (or quasi 1-dimensional) systems. The particular morphology of the *fcc* (110) surface, composed by close-packed rows of atoms separated by channels, was used as a template to grow linear Cu chains [RHB+93, BHF+94] by

diffusion controlled aggregation at Pd(110) surfaces. Even more suited to grow 1-dimensional structures are the vicinal surfaces (or high Miller index surfaces) which, with their ordered array of steps, present an ideal template for the growth of wire superlattices by means of step decoration [GBB+00a, GBB+00b, DCE+00]. This last works were the first to present the growth of real monoatomic rows; in previous attempts only multiatomic rows were obtained [FKBK99, SSK+97] with widths of the order of few nanometers.

6.4.1 Magnetic 4*d* rows at Ag (100) step edges

In this section I present the results for 4*d* magnetic monoatomic rows on *fcc* (711) and *fcc* (410) Ag vicinal surfaces; the slabs used to simulate the decoration at the two different step edges, the (100) × (111) and the (100) × (110), are shown in Fig. (6.4). These slabs are somewhat thinner than the one used for the calculation of

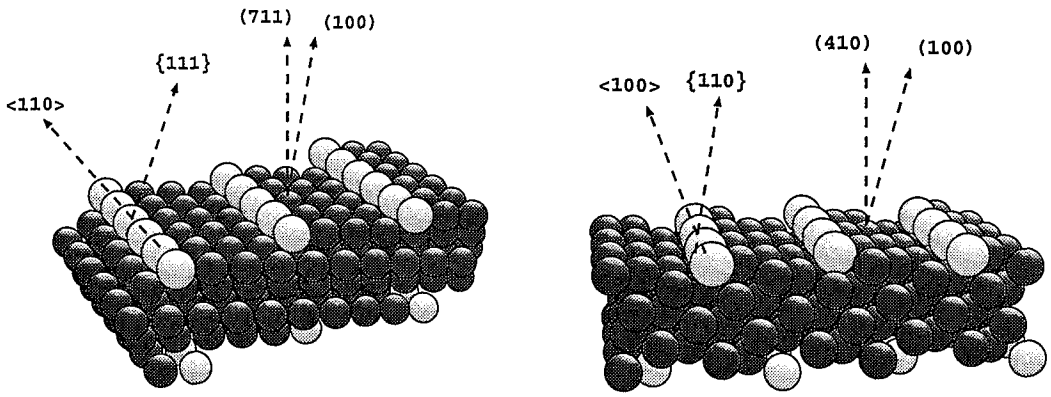

Figure 6.4: The *fcc* (711) and *fcc* (410) slabs which were considered for the magnetic rows calculations; for both the slabs 14 Ag + 6 vacuum layers at each side were considered, i.e. 28 inequivalent atoms.

the step energies; they are typically composed of 4 "low Miller index " planes in the Ag substrate, i.e. 16 Ag vicinal layers. For the limited size of the systems a small row-row interaction between the rows on the two sides of the substrate appear in the systems; test calculations have shown that the magnetic moments changed by no more then few hundredths of μ_B, when up to 4 Ag vicinal layers were added in the substrates; the bigger changes were registered for the Tc and Ru rows, i.e. $\Delta m = \pm 0.05 \mu_B$.

In this section I discuss only the ferromagnetic solutions obtained for the rows; for the elements at the beginning of the transition metal series (3*d*, 4*d* and 5*d*) [HS83] also antiferromagnetic solutions exist, and I will discuss them separately in

section 6.4.3. The magnetic moment profiles for the $4d$ monoatomic rows on the two vicinal *fcc* Ag (711) and (410) substrates are shown in Fig. (6.5 *a*) and Fig. (6.5 *b*). For each step orientation the rows were placed both in step edge and terrace positions; the value for the terrace positions will allow us to simulate the (100) terrace environment and therefore to compare with the results for adatoms, chains and monolayers present in the literature on the Ag(100) surface.

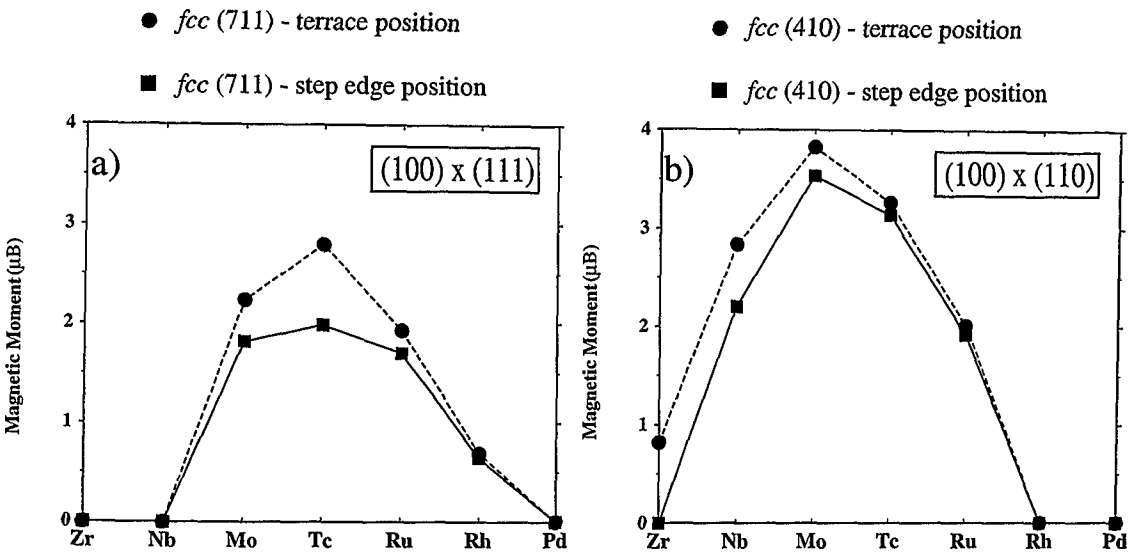

Figure 6.5: Magnetic moments of $4d$ monoatomic rows on the *fcc* Ag (711) (fig.*a*) and *fcc* Ag (410) (fig.*b*) vicinal surfaces used to simulate respectively the close-packed (100) × (111) and open (100) × (110) rows. The rows were placed both in terrace (circles) and step edge (squares) positions of the (001) Ag terraces.

A direct comparison between the magnetic moment profiles for the two different step orientation shows that the magnetic moments for the close-packed rows along the ⟨110⟩ direction (Fig. (6.5*a*)) are smaller than the ones for the open rows along the ⟨100⟩ direction (Fig. (6.5*b*)) for all the elements except Rh. The main reason for this decrease in the magnetic moments is the $4d$-$4d$ hybridization acting between the atoms in each row which is much larger for the close-packed rows than for the open rows, where neighboring row atoms are separated by a 2^{nd} neighbor distance. The role of the $4d$ hybridization was already discussed by Blügel [Blü92a] in the case of $4d$ monolayers on Ag, Au and Pd (001) surfaces and by Willenborg *et al.* [WZD92] in the case of single impurities and dimers in bulk Ag. The *d*-*d* hybridization between the $4d$ orbitals increases the bandwidth, thus broadening the density of states (DOS)

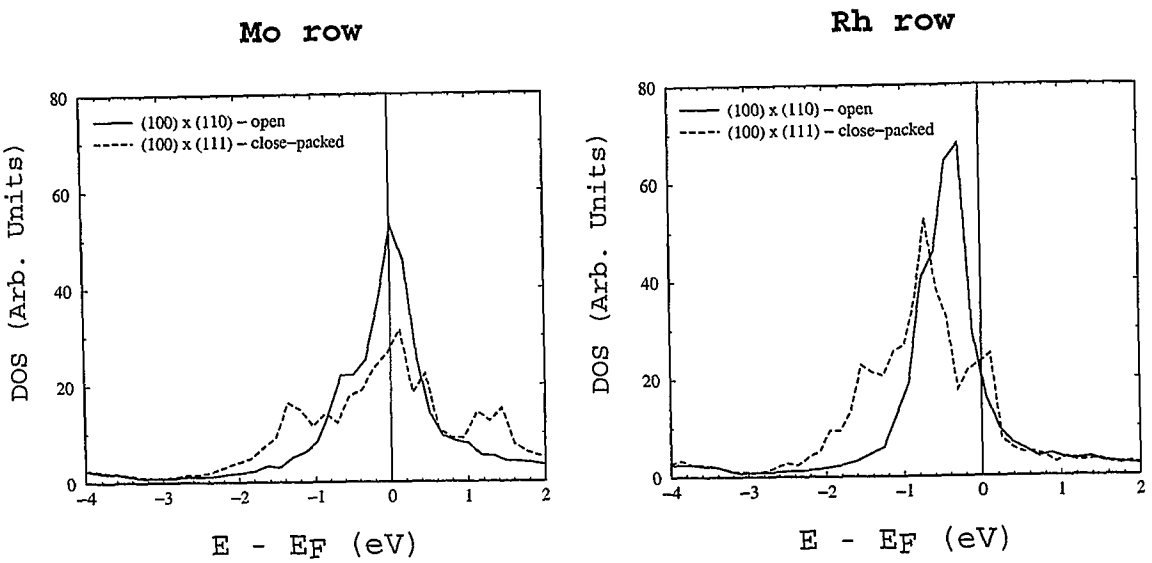

Figure 6.6: Density of States (DOS) for the Mo and Rh magnetic rows at the two step edges (100) × (111) and (100) × (110); the 4*d*-4*d* hybridization mechanism is different for the two elements depending on the position of the virtual bound state peak relatively to the Fermi energy E_F.

obtained e.g. in a paramagnetic calculation.

In Fig. (6.6) I show the paramagnetic DOS for the two representative cases of open and close-packed rows for Mo and Rh, obtained by means of non-spin-polarized calculations. This broadening has two different effects depending on the position of the virtual bound state peak relatively to the Fermi energy E_F; if the peak is very near to the Fermi energy a broadening in the bands causes a reduction of the DOS at the Fermi level (i.e. the Mo case), while if the peak is below E_F it produces an opposite effect and the DOS increases at E_F (i.e. the Rh case). From a simple Stoner description, the condition $n(E_F)I > 1$ (with I the exchange integral) favors the existence of a magnetic moment for those systems which present a high DOS at the Fermi level; the hybridization between the atoms in each row thus reduces the magnetic moments for all the elements up to Ru since the virtual bound state peak is near to the Fermi energy, while it enhances the magnetic moment for Rh. As observed by Blügel [Blü92a] the reduction of the magnetic moments from the single adatoms to the monolayer is accompanied with a progressive shift of the maximum to higher valencies; this is also observed in our case when one compares the results for the open rows with the close-packed ones for which the maxima shift from Mo to Tc (see Fig. (6.5)). This hybridization mechanism is also present for the 3*d* elements

as was shown in [BDZD89] by comparing the results for overlayers on Ag (001) and impurities in bulk Ag; in this case because of the much smaller spatial extent of the $3d$ wave functions only minor changes were observed in the magnetic moments, i.e. only a small systematic shift of the local moment towards higher valencies in the monolayer case. In the particular case of the magnetic rows presented in Fig. (6.5 *a* and *b*) , the strong $4d$-$4d$ hybridization quenches the moments of Zr and Nb and reduces the magnetic moment of Mo up to more than 40%. This reduction become less and less efficient moving to the end of the series and for Rh the opposite trend is observed and a small moment of around $0.6\mu_B$ is predicted.

Since in the open rows the interatomic distance is the one of second neighbor bulk atoms, the hybridization between the $4d$ orbitals is sufficiently weak and the atoms in the row behave, regarding their magnetic properties, practically like isolated adatoms; this is even quantitatively the case as is shown in Fig. (6.7), where the magnetic moments for the $4d$ open rows in the terrace position (Fig. (6.5*b*)) are compared with the one for single $4d$ impurities in the adatom position on the Ag (001) surface [LSW+94].

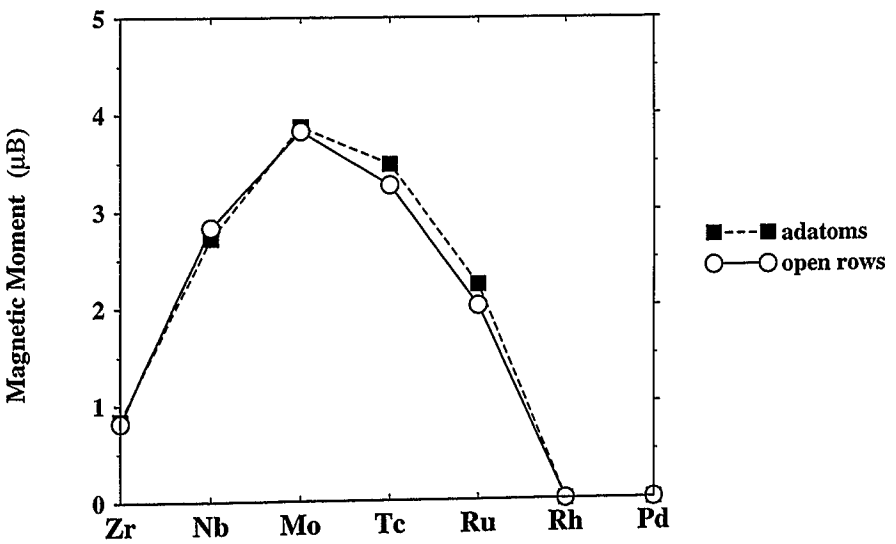

Figure 6.7: Comparison between the $4d$ (100) × (110) open rows in terrace position (open circles) and single $4d$ adatoms (closed squares) [LSW+94] on the (001) terrace.

The results for the $4d$ close-packed rows can be viewed as the 1-dimensional link between 0-dimensional systems represented by the single adatoms and 2-dimensional systems represented by the monolayers. We can thus summarize in Fig. (6.8) the results for these three different systems being adsorbed on the Ag (001) surface, by including the results for the adatom of Lang *et al.* [LSW+94] and the results for the

monolayers obtained by Blügel [Blü92a]. With increasing dimensions the increase

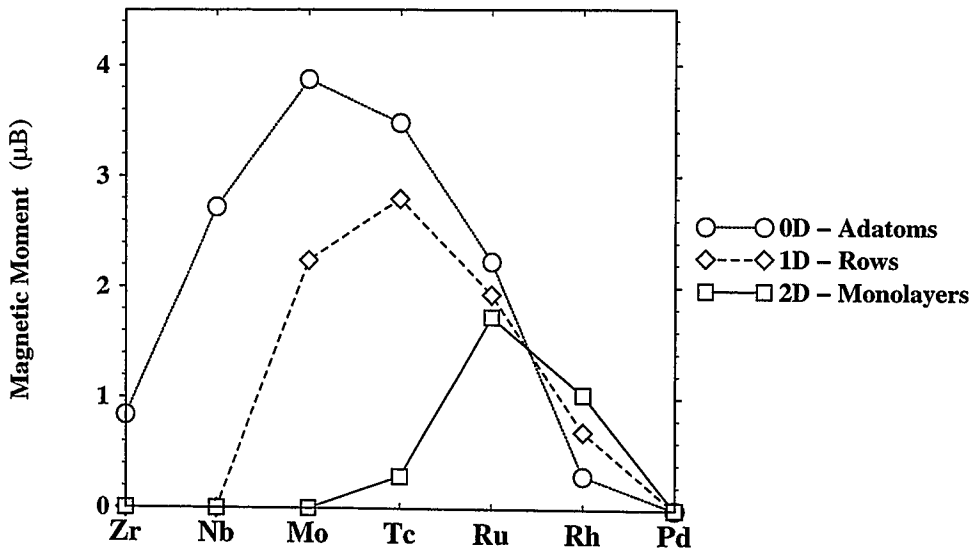

Figure 6.8: Effect of the dimensionality on the magnetic moment profile. Shown are the results for adatoms (circles) [LSW+94], infinite rows (diamonds) and monolayers (squares) [Blü92a], i.e. 0-D, 1-D and 2-D sytems, of the 4*d* series on the Ag(001) surface.

in the 4*d*-4*d* hybridization leads to the progressive decrease of the local moments for the elements at the beginning and center of the series and to a simultaneous shift of the maximum in the moment profile towards higher valencies which is assumed respectively by Mo for the adatoms, by Tc for the adsorbate rows and by Ru for the overlayers. In the limit of 3-dimensional systems, i.e. as bulk crystals, this reduction is strong enough to quench the magnetic moments of all the elements and no ferromagnetism is observed for the whole 4*d* series.

Another evident feature from Fig. (6.5*a*) and (6.5*b*) is that when the magnetic rows are shifted from the middle of the terraces to the step edges, for both the orientations, a decrease of the magnetic moments is observed. This is due to the increase in the hybridization between the extended 4*d* wave functions of the row atoms and the *sp*-like valence electrons of the Ag step atoms. This mechanism was already observed when free 4*d* dimers were compared with dimers adsorbated on the Ag(001) surface [WSL+95]; in that case the hybridization with the Ag substrate was so relevant that the magnetic moments found for the free dimers in the beginning of the 4*d* series (Y,Zr,Nb) were completely quenched and the moments of Mo reduced by a factor of two. Since the magnetic moments are sensitive only to the very local environment and in a very good approximation only to the first atomic shell, i.e. to

the coordination number N_c, the decrease in the magnetic moments can be described by an increase in N_c for the row atoms from the terrace position to the step edge position. As can be easily deduced from Fig.(6.3), a row atom gains respectively 2 Ag neighbors for the open (100) × (110) row and only 1 Ag neighbor for the close-packed (100) × (111) row moving from the terrace to the step edge. Another general feature is that the reduction of the magnetic moments is more enhanced in the beginning of the $4d$ series. This has its justification in the larger spatial extent of the $4d$ orbitals for the elements with lower valencies in the series; in short the earlier elements are more sensitive to the environmental changes than the later elements in the series.

We can now proceede comparing the present results for the infinite rows with the results obtained by Wildberger *et al.* [WSL+95] for small $4d$ chains on the Ag(001) surface, which initiated the present study. In that work, an unusual oscillatory behaviour was predicted for the magnetic moments of finite length $4d$ chains as a function of the chain length; only chains along the ⟨110⟩ direction, i.e. the close-packed one, were investigated and only up to 4 atom chains were studied. The results for the $4d$ close -packed rows at terrace position (open circles in Fig. (6.5*b*)) may thus be viewed as the extension to infinite length of the chains presented by Wildberger *et al.* [WSL+95]. Their prediction of existence of finite moments in the limit of infinite chains is thus verified by the present results.

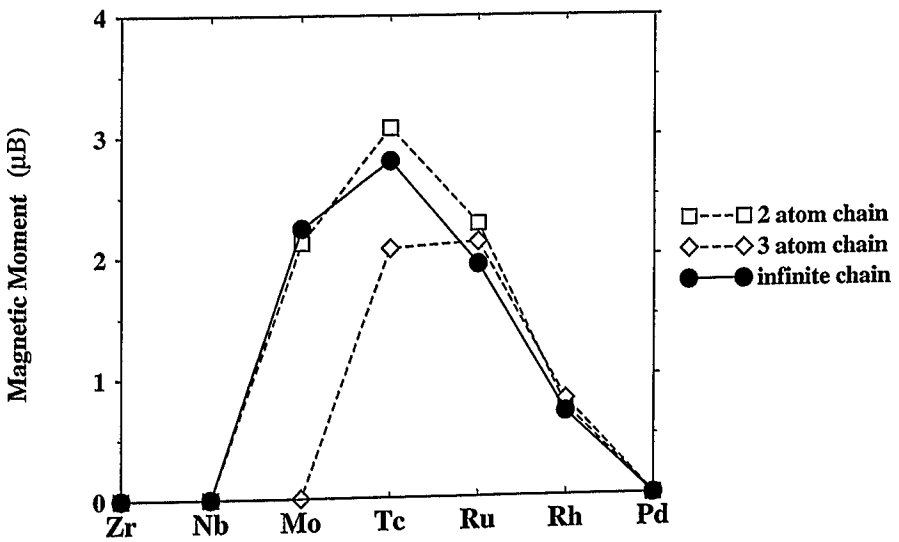

Figure 6.9: Comparison between the magnetic moments of finite-length $4d$ chains [WSL+95] and infinite ones (for closed packed rows, Fig. (6.5*a*) filled circles) on the Ag(001) surface.

In order to compare quantitatively the magnetic moments, I include in Fig.(6.9) the results for the infinite rows together with the profile of the magnetic moments for the 2 atom and 3 atom chains; the magnetic moments presented for the finite length chains is in reality an "average" magnetic moments, since atoms along the chain have different moments depending on the position in the chain (i.e. in the middle or at the end). I do not include the results for the 4 atom chain since their magnetic moments are almost equivalent to the ones of the dimers (see Fig.(3) in reference [WSL+95]). As evident from Fig.(6.9) the magnetic moments for the infinite rows resemble very well the one for the dimers (and thus for the 4 atom chain), and both differ sensibly from the trimers (3 atom chains) for Mo and Tc. Since no results are available for longer chain, i.e. $N > 4$ with N the number of atoms in the chains, it is difficult to say whether a true oscillatory behaviour for the magnetic moments exists as a function of the chain length or if the results for the trimers have to be considered as an "exception". The close agreement between the infinite rows and the 4 atom chains suggest that it is more probable the latter interpretation, and that eventually only minor oscillations are expected to appear for longer chains of atoms. The only work, up to my knowledge, which discuss the magnetic behaviour for finite length chains with $N > 4$, was performed by Dorantes -Davila and Pastor [DDP98], which studied the Magnetic Anisotropy Energy (MAE) for Fe and Co chains by means of a tight-binding Hamiltonian. It is interesting to state here that they observed an unusual tendency for a magnetization perpendicular to the chain direction for some of the 3 atom chains. It seems therefore that the particular length-dependent electronic spectrum of the 3 atom chains leads to the unexpected magnetic behaviours.

6.4.2 Magnetic $4d$ rows at the Ag $(111) \times (111)$ step edge

As discussed above, the magnetic moments of the $4d$ monoatomic rows at different step edges is driven mainly by two effects, i.e. the $4d$-$4d$ hybridization acting between the atoms in each row and the $4d$-sp like hybridization between the row atoms and the Ag substrate atoms, the first hybridization mechanism being driven by the interatomic distance in the row and the second by the coordination number of the row atoms. Since the magnetic moments of the rows are influenced by the very local structural environment, we expect similar magnetic moment profiles for the rows at step edges with similar environment. As shown in Fig. (6.10) the *fcc* (111) terraces presents two step edges, both close-packed and both with coordination number $N_c = 7$, the $(111) \times (111)$ and the $(111) \times (100)$. They should therefore both

exhibit similar magnetic properties as the (100) × (111) step edge which is also close-packed and has a coordination $N_c = 7$; in the following I present the comparison between the magnetic moment profiles of $4d$ rows at the (100) × (111) and at the (111) × (111) steps the last one being depicted in Fig. (6.10).

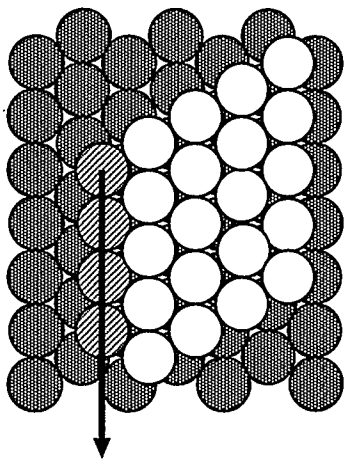

(111) x *(111)*

Figure 6.10: The (111) terrace; only the (111) × (111) step edge is indicated.

From table 6.1, the class of vicinal surface which cuts the *fcc* crystal along the (111) × (111) step edge is characterized by the Miller indices $(hkl) = (m, m, m-2)$. Since terraces composed by 4 atomic rows are sufficiently wide in order to neglect the step-step interactions, I have choosen the vicinal surface with Miller indices $(hkl) = (221)$ (which is the (442) in the above notation, but it is common to remove the costant multiplicative factors from the Miller indices). The *fcc*(221) substrate represents in comparison to the *fcc*(711) and *fcc*(410) surfaces larger interlayer distance, $d_z^{221} \simeq 0.1667 a_{latt}$ vs. $d_z^{711} \simeq 0.1400 a_{latt}$ and $d_z^{410} \simeq 0.1213 a_{latt}$. The calculation were performed using a 19 atom TB-cluster and a number of wave-vectors $n_{\mathbf{q}_{||}} = 43$ in the irreducible part of the 2D Brillouin Zone (for energies in the complex contour). The smaller tilting with respect to the terrace orientation leads to a TB cluster which spans over less layers; therefore the number of layers in each PL is smaller than the one used for the other two vicinal surfaces i.e. $N_P^{221} = 4$ vs. $N_P^{711} = 7$ and $N_P^{410} = 8$ resulting in a smaller computational effort for the solution of the Dyson equation.

As shown in Fig. (6.11), the magnetic profiles obtained placing the $4d$ rows on the two step edges, the (100) × (111) and the (111) × (111) compare very well with each other. The only difference in the local environment for an atom sitting at the two step edges is that the nearest neighbors (NN) are distributed differently in the upper and lower terraces; more precisely for the (100) × (111) 4 NN are on the lower terrace and 3 on the upper terrace (with 2 of these 3 in the row direction), while for the (100) × (111) step edge 3NN are in the lower terrace and 4 in the upper one (with 2 of these 4 in the row direction). This small difference induces for Mo and Tc a difference of around $0.2\mu_B$, and for the other $4d$ elements a difference of less than $0.1\mu_B$ in the magnetic moment profile; this finding completely supports the above description of the dependence of the magnetic moments on the very local

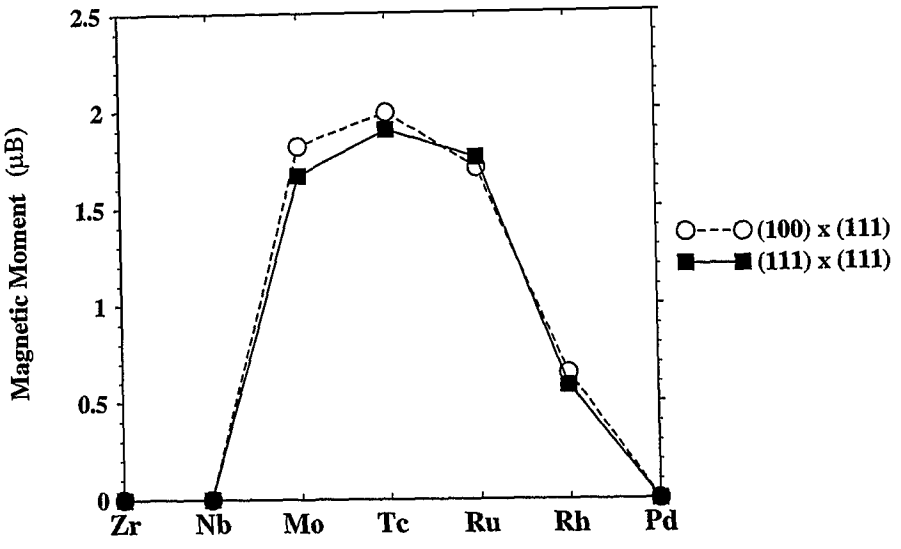

Figure 6.11: Comparison between the magnetic moment profile of the $4d$ rows on the (100) × (111) and (111) × (111) step edges; both step edges show close-packing in the row direction and the same coordination number $N_c = 7$.

environment.

6.4.3 Total energies: ferromagnetic vs. antiferromagnetic solutions.

Up to now I discussed only the ferromagnetic solutions for the $4d$ monoatomic rows at different step edges. But it is well known from general theorems about tight-binding bands [HS83] that there is a tendency towards antiferromagnetism for elements in the middle of transition metal series ($3d$,$4d$ and $5d$). Indeed antiferromagnetic (AFM) solutions were obtained for finite-length $4d$ chains [Wil94, SHR+96] and by means of total energy calculations predicted to be the more stable solutions for Nb and Mo dimers on the Ag(100) terrace.

It is the aim of this section to discuss the antiferromagnetic solutions found for the infinite 1D monoatomic rows and the stability of these AFM solutions vs. the FM and paramagnetic ones. In the case of antiferromagnetic ordering between the atoms in each row it is necessary to double the periodicity along the row direction, i.e. double the number of inequivalent atoms in the systems. Therefore I studied only the case of $4d$ rows at the (100) × (111) Ag step edges, simulated by the *fcc* (711) Ag vicinal surface; the antiferromagnetic order at this step edge is depicted in Fig. (6.12). The computational effort for the study of these systems increases

dramatically since not only the number of atoms doubles, but also the number of layers in each PL increases; using a TB cluster composed of 19 atoms it turns out that 15 atoms in each PL has to be taken into account in order to construct a 4×4 block tridiagonal matrix. The slabs considered for these calculations contains 60 inequivalent atoms, i.e. 30 layers and 2 inequivalent atoms per layers; 14 Ag layers in the substrate were considered and embedded between 6 vacuum layers on each side.

For these systems, the 2D-BZ area has only half of the size as for the case of only one inequivalent atom per layer presented in the previous sections. But in the same time the number of symmetries in reciprocal space decreases and only the inversion symmetry $\mathbf{q}_{||} \longrightarrow -\mathbf{q}_{||}$ remains. For the Brillouin Zone integrations, I considered 25 $\mathbf{q}_{||}$ in the irreducible part of the 2D-BZ for the contour energies and up to 202 $\mathbf{q}_{||}$ points in the vicinity of the Fermi Energy. Because of the extreme computational demand of the present calculations, the parallelized version of the SKKR code [Zel] turned out to be very helpful relieving sensibly the time needed to converge the systems.

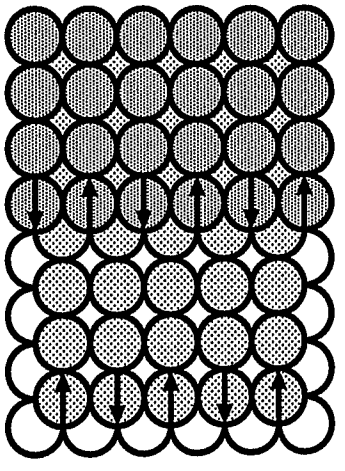

Figure 6.12: Antiferromagnetic coupling in the rows at the (100) × (111) step edge.

In table 6.5, I list the results for the magnetic moments for both ferromagnetic (FM) and antiferromagnetic (AFM) solutions, together with the differences in the total energies between the FM or AFM solutions and the paramagnetic ones, i.e. $\Delta E^{FM} = E^{PARA} - E^{FM}$ and $\Delta E^{AFM} = E^{PARA} - E^{AFM}$; the paramagnetic solutions were obtained by means of non-spin-polarized calculations. AFM solutions with large magnetic moments were found for Mo, $m_{AFM} = \pm 2.72\,\mu_B$, and Tc, $m_{AFM} = \pm 2.06\,\mu_B$, while a smaller magnetic moment has been found for Nb, $m_{AFM} = \pm 0.83\,\mu_B$. From total energy calculations, as shown in table 6.5, the Mo row is predicted to be more stable in the AFM configuration than in the FM one, while for Tc the two solutions (FM and AFM) are almost degenerate in energy. Nb shows no FM solutions while in the AFM case a magnetic moment of $\pm 0.83 \mu_B$ is found. Ru and Rh show only FM solutions. These results are in good agreement with the calculations performed for the $4d$ dimers on the Ag(001) surface [SHR+96]. The only sensible difference is that

Magnetic Moments (μ_B)

	Nb	Mo	Tc	Ru	Rh
Ferro	–	1.85	**1.92**	**1.65**	**0.59**
Antiferro	**±0.83**	**±2.72**	±2.06	–	–

Total energy (mRy)

	Nb	Mo	Tc	Ru	Rh
$\Delta E^F = E^{PARA} - E^{FERRO}$	–	+10.2	**+15.7**	**+7.3**	**+1.5**
$\Delta E^{AF} = E^{PARA} - E^{ANTIFERRO}$	**+0.7**	**+18.8**	+14.3	–	–

Table 6.5: Ferromagnetic (FM) vs. antiferromagnetic (AFM) solutions for the $4d$ monoatomic rows at the (100) × (111) step edge; in the upper table the magnetic moments for the FM and AFM case, and in the lower table the total energies for the FM and AFM solutions relative to the total energies of a constrained paramagnetic calculation are listed. In both tables I emphasized in bold characters the solutions which are predicted to be more stable.

also for the Ru dimer a (metastable) AFM solution is found; since in the case of the Ru row, the FM solutions is only $7.3mRy$ lower than the paramagnetic one, I expect that the Ru AFM solution, if it exists, is almost degenerate with paramagnetic one. However in the calculations we could not find an indication for an AFM solution. In the case of the $4d$ dimers the energy difference between the AFM and the FM solutions, are systematically larger than the one that can be derived from table 6.5 calculating the difference $\Delta E = \Delta E^{FM} - \Delta E^{AFM}$. For example, for a Mo dimers the AFM state is more stable the the FM one, with moment respectively of $m_{AFM} = 3.17\mu_B$ and $m_{FM} = 2.12\mu_B$ [Wil94], and an energy difference of about $50\,mRy$ [SHR+96], For the Mo row a much smaller energy difference ΔE between FM and AFM solutions is obtained, i.e. $\Delta E = 8.6mRy$. The $4d$ monolayers with FM ordering on the Ag(001) surface [Blü92a] showed total energies with similar order of magnitude; the larger magnetic moment was found for Ru, $m = 1.73\mu_B$ with $\Delta E_{FM} = 6.7mRy$ above the paramagnetic solutions. From the above picture it is therefore evident that, for the $4d$ series, moving from the lower coordinated systems (dimers) to the more cordinated ones (rows and monolayers) the magnetic solutions progressively become less stable in comparison to the paramagnetic ones. In the limit of the maximum possible coordination, i.e. as bulk materials, indeed all the elements in the $4d$ series are predicted to be non magnetic.

In the present calculations the atoms were supposed to sit in their ideal posi-

tions, i.e. no atomic relaxations are included in the calculations; the relaxations at the step edges usually try to smooth the step edges, i.e. inward relaxation towards the substrate is expected for the step atoms. The size of the total energy differences ΔE^{FM} and ΔE^{AFM} can be viewed as an indication of the stability of the magnetic solutions versus such environmental changes. If for the surface energies and step energies, changes up to 20 - 25 % have to be expected, the magnetic moments are expected somehow to be less effected by relaxation effects. Recently some calculations for Fe,Co and Ni rows on the Pt (111)$\times$(111) were performed [Bih], and atomic relaxations were taken into account. Inward relaxations of the order of $13 - 14\%$ in the distance between the row atoms and the step atoms occur in the systems, smoothening slightly the step profile; the magnetic moments are influenced even less than these percentage since the $3d$ orbitals are very much localized. For the $4d$ series relaxations are expected to more strongly influence the magnetic moments, since the larger spatial extent of the $4d$ orbitals leads to a higher sensitivity to the structural changes. The relaxation energy do usually not exceed the value of $0.1eV$. We expect therefore that the general trends obtained in the present calculations, in particular the large moments obtained for Mo, Tc and Ru rows as well as trends towards ferro- and antiferromagnetism, will not be changed by the inclusion of lattice relaxations.

Another point which has to be noted, is that in one-dimensional spin chain no phase transition for any finite temperature ($T \neq 0$), i.e. no long range order exists, as proved by different one-dimensional models like the Ising spin chain [Isi25]. Even magnetic anisotropy does not stabilize the magnetic ordering as it happens to occur in two-dimensional systems for not too high temperatures. The FM or AFM solutions presented in this and the previous sections have thus to be interpreted as describing the short range order only; the long range order obtained can be viewed as a fictitious feature due to the mean field treatment of the electron-electron interactions introduced by the DFT-LDA approach. In reality the local moments exist, however the orientations of the local moments are disordered such that only short range order, but not long range order, exists. In principle the interactions between the rows should play a role in stabilizing a magnetic ordered phase at very low temperatures, since these interaction convert the system into a two-dimensional one, being stabilized by anisotropy for sufficiently low temperatures. In this line the appearence of a local magnetic moment for Co 1D structures on Pt(997) have been recently suggested from non-spin-polarized photoemission experiments [DCE+00].

Chapter 7

Complex band structures

In this chapter we present results for complex band structure calculations of several insulators obtained by means of the Screened KKR method. In the study of Mavropoulos *et al.* [MPD00] complex band structures for Si, Ge, GaAs and ZnSe were reported employing an empirical local pseudopotential plane-wave technique. The empirical approach proposed in [MPD00] requires smaller computational effort with respect to an *ab-initio* one, and is able to describe with good approximation real and complex band structures of insulators in the gap region. Such approach is however limited in its application range since it needs input parameters fitted to spectroscopic data, the so called *form factors*, which exist in the literature only for a limited number of systems. In order to provide for a more flexible parameter-free approach, we report herewith the implementation of real and complex band structure calculations within the SKKR approach. We discuss shortly how the analysis of the complex band structures of a insulator can supply for an intuitive understanding of tunneling phenomena at a ferromagnet/insulator/ferromagnet (FM/I/FM) tunnel junction. We then present the results for ZnSe, MgO and $SrTiO_3$.

7.1 FM/I/FM junctions and complex band structures

The broad interest in the study of the transport properties of (FM/I/FM) junctions has its origin in the first evidence in the early work of Julliere [Jul75] of the tunneling magnetoresistance (TMR) effect. In the study of Julliere [Jul75], it was shown that the conductance in FM/I/FM junctions is dependent on the orientation (parallel or antiparallel) of the magnetization of the two FM leads. While the TMR effect

itself was discovered long ago, only recently one has succeded to obtain TMR ratio as high as 20% at room temperature [MT95, MKWM95]. The reason is that many different phenomena at the interface like the appearence of domain walls as well as direct coupling between the two FM leads limit the TMR effect, and only with the advent of very refined experimental techniques it was possible to remove this limiting factors. After this achievements, FM/I/FM junctions imposed themselves as very competitive candidates for industrial applications on magnetic sensors or memory elements. From the theoretical point of view only recently first principles calculations of FM/I/FM junctions have appeared in the literature [BZW+97, Pap]. These studies suggest that an accurate description of the band structures of the materials composing the junction is of fundamental importance for a proper understanding of the TMR effect.

How are actually the complex band structures and the tunneling mechanism connected? In the case of a bulk material only solution with real wave vector $\mathbf{k}$ are allowed due to periodicity condition. This condition is absent in an interface (or surface) of a crystal; therefore solutions with complex $\mathbf{k}$ can actually match with wave functions on the other side of the interface (or surface) and form evanescent states or metal-induced gap states (MIGS) [Hei62]. In the specific case of semiconductors complex bands inside the gap region can therefore host such evanescent states arising from the leads. These complex $\mathbf{k}$ bands (or simply *complex bands*), though they do exist only at surface and interfaces, are in reality solutions of the Schrödinger equation associated to the bulk material. This can be understood considering the fact that they extend very deep in the bulk of a crystal, while the interface (or surface) changes in the charge density are restricted only to one or two layers. The tunneling at FM/I/FM junctions can thus be explained by the existance of such MIGS in the insulator spacer. Therefore, as was pointed out recently [MPD00], the mechanisms through which the tunneling takes place can be traced back very intuitively to the the analysis of the complex bands of the insulator, in connection with the analysis of the real bands of the leads under interest.

7.2 Band structure calculation

We give in the following a short description on how by means of the SKKR method, real and complex band structure can be calculated [Zah98, MMZ87]

As we have discussed in section 3.1, we can trace back the calculation of the electron density to the calculation of the Green's function of our system for which

it holds the equation (in operator notation)

$$(E - \hat{H})|\psi\rangle = 0 \quad \Longrightarrow \quad \hat{G}^{-1}|\psi\rangle = 0 \tag{7.1}$$

where $\hat{H}$ is the Hamiltonian of our system, and E are the energy eigenvalues associated to the eigenfunctions $|\psi\rangle$. The Green's function $\hat{G}$ of the real system are connected to the reference Green's function $\hat{G}^r$ by the Dyson equation in Eq. (4.14). As a consequence of the Bloch theorem the eigenfunctions of Eq. (7.1) are Bloch waves, and can be expanded on the radial regular solution $R^{\mu}_{L}(r, E)$ of the scattering from a single potential discussed in section 3.2, as

$$\psi_{\mathbf{k}}(\mathbf{R}^n + \mathbf{r}^{\mu} + \mathbf{r}) = \sum_{L} e^{i\mathbf{k}\cdot\mathbf{R}^n} C^{\mu}_{L}(\mathbf{k}) R^{\mu}_{L}(r, E) \tag{7.2}$$

where $\mathbf{R}^n$ are the lattice vectors and $\mathbf{r}^{\mu}$ are the basis vectors. The eigenvalue equation

$$G^{-1}C = G^{r\,-1}(1 - G^r \Delta t)C = \lambda C \tag{7.3}$$

where $G = \mathrm{G}^{\mu\mu'}_{LL'}(\mathbf{k}, E)$, $G^r = \mathrm{G}^{r\,\mu\mu'}_{LL'}(\mathbf{k}, E)$ and $\Delta t = \Delta t^{\mu}_{LL'}(E)$ holds. The energy eigenvalues $E^{\nu}_{\mathbf{k}}$ are then given by the condition

$$\lambda^{\nu}(\mathbf{k}, E^{\nu}_{\mathbf{k}}) = 0 \tag{7.4}$$

The zeros of G^{-1} characterize the eigenstates of the real system; the eigenvalue problem is then solved by means of the computation of the zeros of the determinant of G^{-1}. Moreover the repulsive reference system considered in the SKKR program and described in section 4.2 does not have any eigensolutions in the energy region of interest for a band structure calculation, i.e. $\det[G^{r\,-1}] \neq 0$. We can reformulate the eigenvalue problem with the help of the KKR matrix M, given by $M = (\Delta t)^{-1} - G^r$, as the calculation of the zeros of the determinant of M, i.e. $\det M = 0$

7.3 Complex band structures of ZnSe, MgO and $SrTiO_3$

We discuss here the complex band structures for three insulators (semiconductors) with different crystallographic structures, i.e. ZnSe (zinc-blende), MgO (NaCl) and $SrTiO_3$ (cubic perovskite); in the present calculation the experimental lattice constant are used. The band gaps obtained by the SKKR for the three semiconductors,

as we will find out in the following, will underestimate systematically the experimental gaps. This is a well known problem of the Local Density Approximation which fail to give a proper description of the excitation properties of semiconductors and insulators. For ZnSe and MgO we obtain a direct gap at the Γ point respectively of $1.1\,eV$ and $4.6\,eV$, while the experiments gives values of $2.8\,eV$ and $7.8\,eV$; our LDA results agree well with other theoretical results in the literature [CMF88, KPBZ87]. In the case of $SrTiO_3$ we obtain a direct gap at the Γ point of $2.6\,eV$ while in the experiment an indirect gap at the $\Gamma - R$ point of $3.3\,eV$ is measured. On the other hand our indirect $\Gamma - R$ point is only $.1eV$ larger than the direct one; in other theoretical investigations in the literature for $SrTiO_3$ evidences of direct or indirect gaps are found depending on the details of the calculations [Mat72, KYTW95, SSM00]

As anticipated in section 7.1, near a crystal surface or interface, solutions of the Schrödinger equation with complex $\mathbf{k}$ vectors can match with solution outside the crystal giving rise to evanescent states exponentially decaying in the crystal. The states in a metal/insulator/metal junction responsible for the transport properties are those at the Fermi energy E_F. Therefore, since E_F lies in the case of a metal/insulator interface inside the gap of the insulator, we are mainly interested in the complex bands with energies inside the gap region, which could host the leads states and make them tunnel through the insulator.

The complex band structure will be calculated for the bulk insulator, but introducing a "surface" notation for its Brillouin zone. This is necessary since we want to discuss the results relative to a precise interface orientation of the FM/I/FM junction. We use in the following the same notation as proposed [MPD00]. The wave vector $\mathbf{k}$ is divided into a component $\mathbf{k}_{||}$ parallel to the interface under interest and a component $\mathbf{k}_z$ perpendicular to it. The first component is real and is conserved during scattering (assuming a perfect periodic interface); the second component is complex, i.e. $k_z = q + i\kappa$, where κ is the *decay parameter*. Since the corresponding evanescent state will decay like $e^{-\kappa z}$, where z is the distance from the interface we are interested in the solutions with the minimal value of κ_{min}, i.e. the ones which decay slower inside the insulator. We denote as *real lines* the solutions of the Schrödinger equation associated with real energies, which span in the (q, κ, E) space, for certain $\mathbf{k}_{||}$ and arbitrary complex $\mathbf{k}_z$.

We present in Fig. (7.1) the complex band structure of ZnSe (semiconductor), for the value $\mathbf{k}_{||} = 0$, and some special complex k_z (with its real part along the (001) direction). In the central panel of Fig. (7.1) are plotted the real bands, i.e. with $\kappa = 0$ in the $\Gamma - X$ direction. For the two extremes, i.e. $q = 0$ (left panel) and $q = \frac{2\pi}{a}$ (right panel), with a being the lattice constant, the nonreal bands for $0 < \kappa < \frac{2\pi}{a}$ are

drawn. It goes beyond the scope of this study to enter in the details of the topology of the real lines, and we rather refer the reader to the study of Chang. Nevertheless, from Fig. (7.1), the main features of the real lines can be deduced. First of all, real

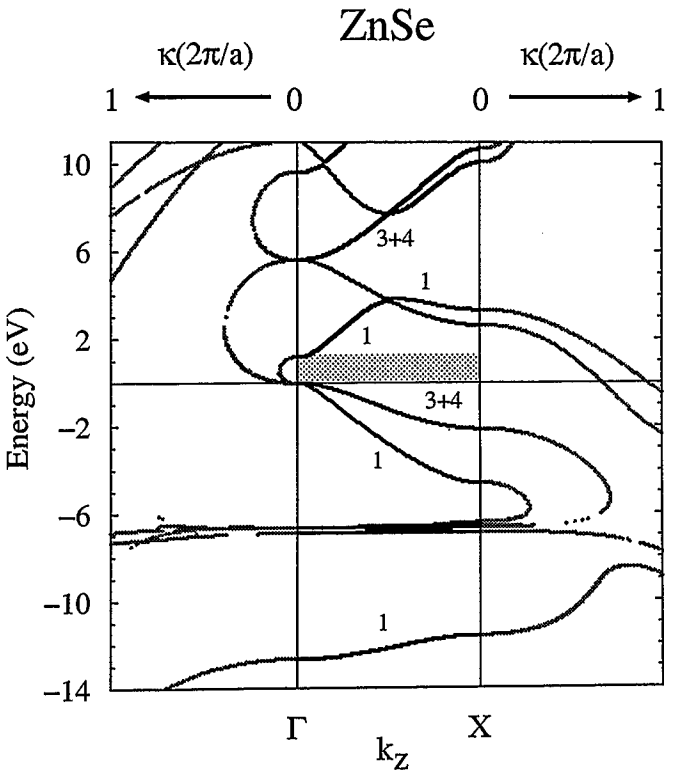

Figure 7.1: Complex band structure of ZnSe, for $\mathbf{k}_{||} = 0$ at $q = 0$ (left panel) and $q = \frac{2\pi}{a}$ (right panel); for space reasons the symmetries have been indicated omitting the letter Δ which characterizes the symmetry direction $\Gamma - X$.

lines depart from the real q axis wherever there is a local maximum or minimum of the real band with respect to q. They can either form loops reconnecting on the real q axis to other extrema of the real bands or present free-electron like parabolas extending to $E = -\infty$. This means that in reality the full map of real lines would be more complicated than the one shown in Fig. (7.1); for instance a real line would start in the local maximum shown by around $4\,eV$ and another one would depart from the local minimum at around $4\,eV$ in the middle of the $\Gamma - X$ direction, i.e. $q = \frac{\pi}{a}$. The lines on the top left corner of the picture arise from parabolic real lines departing at extrema in the high energy region. The complex band structure of ZnSe calculated by the SKKR method in Fig. (7.1) shows the same structures as the one presented in ref. [MPD00], obtained by empirical methods; the only difference is that in the empirical calculations presented in [MPD00] the $3d$ bands of Zn (the one

at around $-7\,eV$ in Fig. (7.1)) were not taken in the valence region. In this case in the left panel, i.e. $q = \frac{2\pi}{a}$, the real line starting at the X point around $-4.5\,eV$ connects with the X point around $-11.7\,eV$ (instead of connecting with the Zn $3d$ states, while the one around $-2\,eV$ shows the free-electronlike parabolic solution and extends to $-\infty$.

A full investigation of the complex bands, in order to determine where the minimal decay parameter κ is assumed, would require, as suggested in [MPD00], two different steps: at first for a fixed value of $\mathbf{k}_{||}$ and E to search among all the solutions the ones which smaller value of κ and afterwards varying $\mathbf{k}_{||}$ searching for the absolute minimum κ_{min}. In the case of the direct gap of ZnSe, a departure from the $\bar{\Gamma}$ which corresponds to $\mathbf{k}_{||} = 0$, implies an opening of the gap, as evident from the real bands along the $\Gamma - X$ direction in Fig. (7.1). Therefore the value of κ would become larger due to the larger loop, for $\mathbf{k}_{||} \neq 0$. This suggests us that the small decay parameter shown at the Γ point from the Δ_1 symmetry line is our minimal κ_{min}. This should be valid for all the semiconductors (or insulators) with direct gaps and with top valence and bottom conduction bands at the Γ point with the same Δ_1 symmetry.

What happens in a junction between this kind of semiconductors and, for instance, two Fe leads? Since the Δ_1 symmetry is the one with the smallest decay parameter, it will be the only one able to host the states from the two Fe leads and eventually make them tunneling; this actually is rigorously valid only for large semiconductor thicknesses [MPD00]. In the $\Gamma - H$ direction (001) of the *bcc* Brillouin zone only the majority band presents states at the Fermi energy E_F with Δ_1 symmetry. This means that states with Δ_1 symmetry from the majority bands will tunnel through the semiconductor; if the other lead has the same magnetization orientation, i.e. if the two leads are ferromagnetically aligned, then this states will be picked up by the majority bands of the second lead and contribute to the tunneling current. If on the other hand the leads are antiferromagnetically aligned, majority and minority states in the second lead are reversed with respect to the first one; since no Δ_1 states exist in the minority bands of the second lead, no coupling is allowed and therefore the Δ_1 state will not tunnel, i.e. the conductance is zero.

The above picture is valid also, as shown in Fig. (7.2), for MgO which as GaAs or ZnSe grows epitaxially on Fe and therefore is another interesting candidate for the study of tunneling junctions. In Fig. (7.2) the real lines for the same value of complex k_z as presented in (7.1) are shown. Similar to ZnSe, MgO shows a direct gap at the Γ point, and again the loop which connect points with symmetry Δ_1 is the one that presents the smallest value of κ inside the gap. Since the gap increases

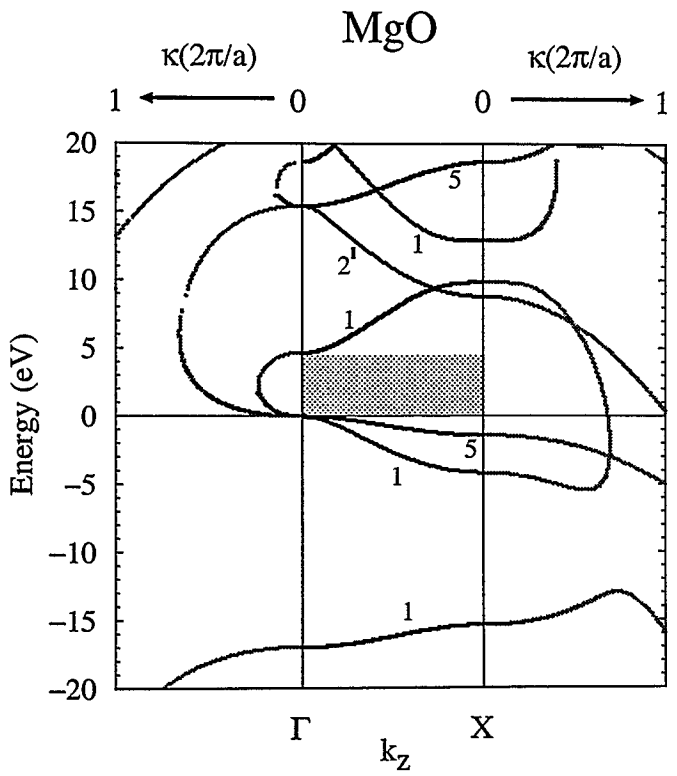

Figure 7.2: Complex band structure of MgO, for $\mathbf{k}_{||} = 0$, at $q = 0$ (left panel) and $q = \frac{2\pi}{a}$ (right panel); for space reasons the symmetries have been indicated omitting the letter Δ which characterizes the symmetry direction $\Gamma - X$.

moving away from the Γ point, the decay parameter shown by the Δ_1-loop at the $\mathbf{k}_{||} = 0$ (Γ) point is our κ_{min}.

Could values of $\mathbf{k}_{||} \neq 0$ and symmetries different than Δ_1 play a role in the tunneling process through semiconductors? It was discussed in ref. [MPD00] that in the case of indirect gaps, minimal values of κ could be assumed for different values of $\mathbf{k}_{||} \neq 0$. In that case a crucial role is assumed by the position of the Fermi energy inside the gap region. For instance, Si has a indirect gap where the maximum of the valence band is at the Γ point while the bottom of the conduction band is near the X point in the $\Gamma - X$ direction. Then also in the surface projected $\bar{\Gamma} - \bar{X}$ direction a minimum is assumed for a value of $\mathbf{k}_{||}$ in between Γ and X. For a value of the energy close to the conduction minimum, a value of κ arbitrarily small can be found. If we lower the energy, when could eventually reach the same small κ for a energy value near the valence maximum at theΓ point. Therefore the minimal κ is assumed at $\bar{\Gamma}$ if the energy is near the top of the valence band and near the $\bar{X}$ point if the energy is near the bottom of the conduction band. If the upper valence and lower

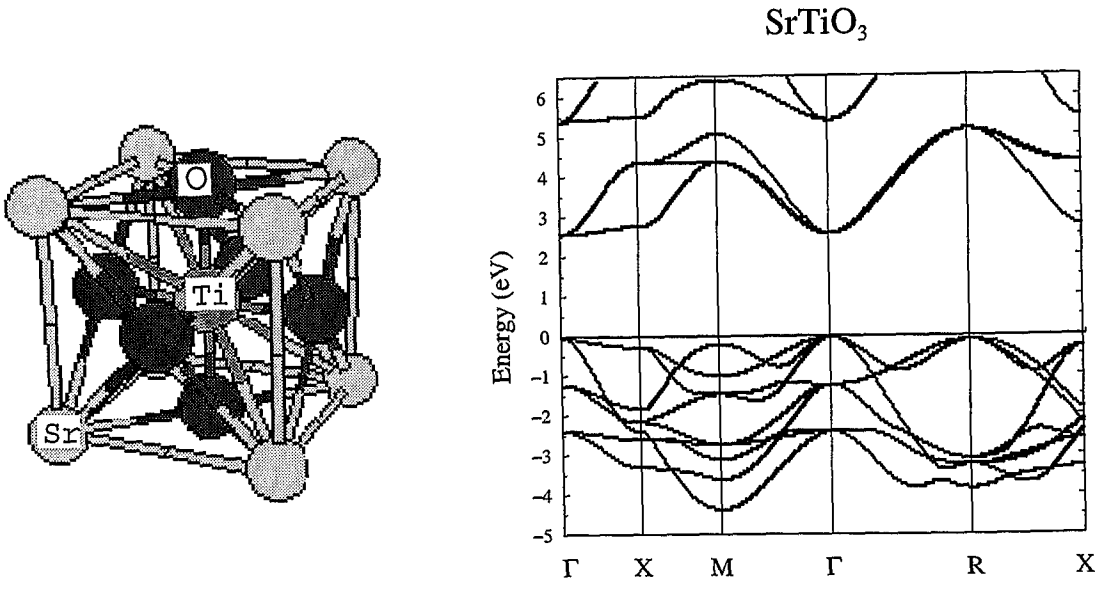

Figure 7.3: Cubic perovskite structure and real band structures of $SrTiO_3$.

conduction band have different symmetries then the position of the Fermi energy would determine not only the value of $\mathbf{k}_{||}$ with the smallest decay parameter κ_{min} but also which symmetry will favour the tunneling through the insulator.

We present in the following a third case which can arise and was observed investigating a perovskite semiconductor, i.e. $SrTiO_3$. In Fig. (7.3) we depict the cubic perovskite structure assumed in nature by $SrTiO_3$ at high temperature, i.e. $T > 110\,°K$, which is also the structure we used in our calculations. For lower temperature the cubic structure distorts to a tetragonal one. We show in Fig. (7.3) also the real band structure along the symmetry directions connecting the points $\Gamma - X - M - \Gamma - R - X$ belonging to the simple cubic Brillouin zone. The band gap in the present calculations is found at the Γ point, but the indirect gap at the $\Gamma - R$ points is only $0.1\,eV$ larger. We present in Fig. (7.4) the complex band structure only for the values of $q = 0$ (Γ) and $q = \frac{2\pi}{a}$ (X) at $\mathbf{k}_{||} = 0$ ($\bar{\Gamma}$); since, as shown in Fig. (7.3), for both the $\Gamma - X$ and $\Gamma - M$ directions the gap opens, the smallest decay parameters should be assumed near the $\mathbf{k}_{||} = 0$ point. At the Γ point two loops with different symmetry appear, i.e. Δ_1 and Δ_2, and they cross at a energy value roughly in the middle of the gap. Therefore the smallest value of κ will be assumed by the Δ_1-loop or the Δ_5-loop depending on whether the Fermi level lies near the valence bands or near the conduction bands inside the gap region. If for instance the Fermi energy of the leads lies in the position indicated by E_1, i.e. $E_F = E_1$

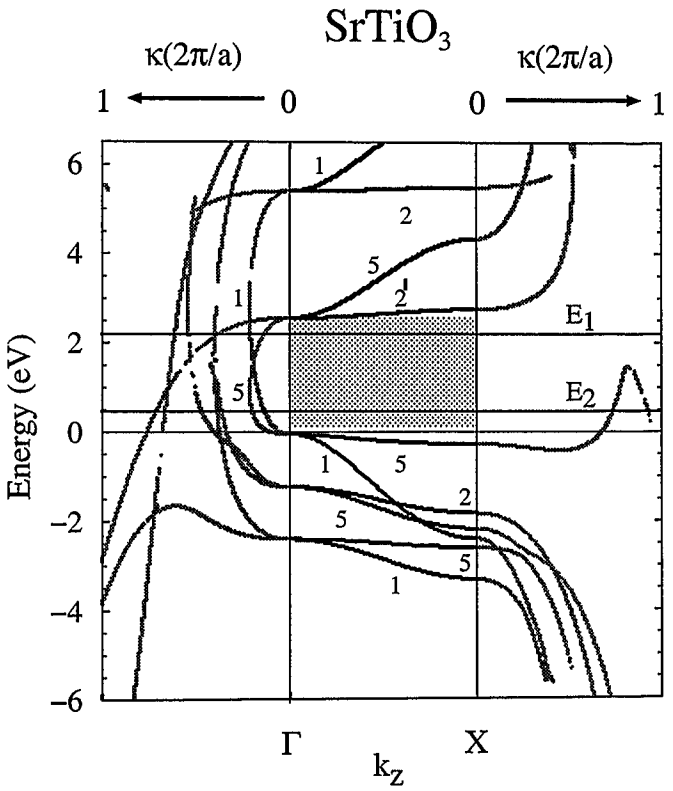

Figure 7.4: Complex band structure of $SrTiO_3$, for $\mathbf{k}_{||} = 0$, at $q = 0$ (left panel) and $q = \frac{2\pi}{a}$ (right panel); for space reasons the symmetries have been indicated omitting the letter Δ which characterizes the symmetry direction $\Gamma - X$.

then the Δ_1-loop assumes the smaller decay parameter κ; in the case of $E_F = E_2$ the Δ_5-loop has the smallest κ. Whether one or the other symmetry would play a role in the conductance, depends obviously on the existence of states with the same symmetry at the Fermi energy in the band structures of the leads. In the case of an Fe lead, for instance, states with Δ_5 symmetry exist for both majority and minority bands, and therefore only the usual Δ_1 states will induce a "spin" filtering through the semiconductor.

Chapter 8

Summary and conclusions

In this thesis we have performed *ab initio* calculations by means of the "Screened" KKR program within the Density Functional Theory (DFT) in the Local Spin Density approximation (LSDA). During this study many improvements to the existing version of the SKKR program have been performed in collaboration with N. Papanikolaou, in order to treat on the same footing systems with arbitrary two- or three-dimensional periodicity.

We summarize in the following the results for three different systems investigated during this thesis.

The study presented in the first part was inspired by a recent experimental investigation performed by Swinnen *et al.* [SMD+97] by means of Time Differential Perturbed Angular Correlation (TDPAC) spectroscopy. The hyperfine fields induced on Cd probe atoms implanted in a Fe/Co (110) multilayers system were measured, and the magnetic moments were deduced based on a model proposed by Stearns for the hyperfine fields [Ste73]. Large oscillations were predicted by Swinnen *et al.* [SMD+97] for the Fe and Co layers approaching the interface. The magnetic moment profiles at the *bcc* (001) and (110) Fe/Co interface obtained by our SKKR program, contrary to the experiments, does not show any oscillations; the Fe magnetic moment monotonically increases moving towards the interface, while the Co moment remains almost constant throughout the interface region. This is in agreement with other calculations existing in the literature obtained by different *ab-initio* methods [ŠV98, NJS99], and the calculated results can be explained similarly to the behaviour of bulk Fe, bulk Co and FeCo disordered alloys. The most probable origin of the discrepancy between the theoretical and experimental magnetization profiles is the very simplified model used by Swinnen *et al.* [SMD+97] to deduce the magnetic profiles from the measured hyperfine fields. The basic assumption made by this

model is that the main contribution to the hyperfine field at a diamagnetic probe atom (like Cd) arises from the polarization induced by the neighboring first shell of atoms, while further shells contribute only to a minor extent. We investigated the origin of the Cd hyperfine field by means of dilute Cd impurity in bulk Co calculations, where we replaced one by one the Co neighbors in the first two shells, i.e. NN and NNN atoms, with Fe atoms. We found that an Fe atom in the second shell contributes to the Cd hyperfine field more than an Fe atom in the first shell. The detailed comparison between the calculated Cd hyperfine fields and the measured ones, shows common points as well as disagreements. The hyperfine field values for the Cd in bulk Co and Cd in bulk Fe environment agree well with the measured ones, provided that the experimental Fe lattice constant is used. The same holds for the Cd at an interdiffused Fe/Co interface, where broad distributions are observed in the experiments due to many microscopically different magnetic environments. Since the well defined Cd hyperfine fields at sharp Fe/Co interface layers observed in our calculations have no counterparts in the experiments, we conclude that the interfaces investigated by Swinnen *et al.* [SMD+97] are strongly interdiffused. We also used the SKKR method to study the Fe and Co hyperfine fields at Fe/Co interfaces, and in dilute and ordered Fe/Co alloys. The behaviour of the calculated hyperfine fields at the Fe/Co (001) and (110) interfaces can be explained by the different polarization mechanism acting on the Fe and Co atoms. Detailed analysis of the results of dilute alloys calculations has shown an unexpected large "transferred" contribution to the hyperfine fields from the neighoring second shell (NNN) of atoms with respect to the first one (NN). This feature, which has been found for the hyperfine field induced to magnetic atoms, i.e. Fe and Co, as well to non-magnetic atoms, i.e. Cd, in *bcc* FeCo dilute alloys is therefore a peculiarity of the *bcc* structure for which the calculations have been performed. Calculations for the FeCo B2 ordered alloy confirmed this picture. If the behaviour of the hyperfine fields induced on an Fe atom as a function of the neighboring Co atoms is consistent with Mössbauer and NMR investigations, the results for the Co hyperfine field in the FeCo B2 ordered alloy are in clear disagreement with the experiments [JWP96]. No final conclusion can be proposed in this case since it is not clear whether the adoption of non local functionals [KA98], abandoning therefore the LSD approximation adopted throughout this study, could influence the calculated results.

In the next part of this thesis we performed calculations of magnetic monoatomic lines of $4d$-atoms, from Nb to Pd, obtained by step decoration of Ag vicinal substrates. This study was motivated by recent experimental investigations, where, by means of MBE techniques together with real time control of the deposition stage,

one has succeeded to grow one-dimensional monoatomic rows on stepped surfaces [RHB+93, GBB+00a], and to observe row-induced electronic states by means of angle-resolved photoemission experiments [DCE+00]. We exploit, similar to the experiments, the concept of vicinal (or high Miller index) surface to characterize an ordered array of monoatomic rows. The magnetization profile of the $4d$ rows has been investigated, placing the rows at terrace and step edge positions of three different high-index surfaces, i.e (711), (410) and (221) , of *fcc* Ag. The results can be explained by the coordination number of the row atoms, and by the hybridization acting between the $4d$ row atoms and the Ag substrate atoms. The effect of the dimensionality on the magnetic properties is also discussed comparing the results for the monoatomic rows with the ones in the literature for $4d$ adatoms, finite-length rows, and monolayers on the Ag(001) surface. The results obtained in this work for the monoatomic rows are in complete agreement with the picture proposed in the literature, showing how the increase in the hybridization between the $4d$ atoms leads to the progressive decrease of the local moments for the elements at the beginning and center of the series and to a simultaneous shift of the maximum in the moment profile towards higher valencies. Since it is predicted by general theorems about tight-binding bands [HS83], that antiferromagnetic solutions exist in the middle of the transition metal series, we investigated the occurrence of antiferromagnetic (AFM) coupling between the atoms in each rows, and discussed the stability of the AFM solution with respect to the FM ones. In detail, we found that Nb exhibits only the AFM solution while only two elements present both FM and AFM solutions, i.e. Mo and Tc; while the AFM solution of Mo is clearly the stabler one, the FM and AFM solutions for Tc are almost degenerate in energy. Parallel to the study of the magnetic rows, we have also directed our attention on the characterization of step energies. The role of steps is of fundamental importance in the characterization of a wide range of surface phenomena like faceting, roughening and crystal growth. Since accurate total energies can be calculated by means of our SKKR program, we presented preliminar results for high-index surface and step energies for Cu and Ag substrate; the results agree very well with the ones existing in the literature obtained by means of TB-LMTO methods [VRSK98, VSK99]. The calculation presented for the vicinal surfaces and magnetic monoatomic rows, for their extreme computational demand, can be considered as a first challenging application of our *Screened* KKR program. The linear scaling behaviour shown for planar systems, i.e. surfaces or interface, relieved sensibly the computational effort, and only for some selected problems like antiferromagnetic coupling in the monoatomic rows the use of parallel supercomputers has been necessary.

In the last part of the thesis we have presented results for the complex band structures of some semiconductors (insulators), i.e. ZnSe, MgO and $SrTiO_3$, obtained by means of the SKKR method. It was demonstrated recently [MPD00] that the analysis of the complex band structures of insulators supplies a powerful tool in connection with the concept of metal-induced gap states (MIGS) [Hei62] for the characterization of the tunneling processes in metal/insulator/metal junctions (FM/I/FM). Of crucial importance is the symmetry of the band which presents the smallest decay parameter, i.e. smallest imaginary value of the complex wave vector. In the case of direct gap semiconductors, e.g. GaAs and ZnSe, the Δ_1 symmetry is the one which shows the complex loop with the smallest decay parameter assumed at the center of the surface projected Brillouin zone, i.e. the $\bar{\Gamma}$ point. We found that MgO, which also is important for FM/I/FM systems since it grows epitaxially on Fe, behaves similarly to ZnSe. A different picture can be found for semiconductors with a indirect gap, i.e. Si, or for semiconductors for which the top valence and bottom conduction bands are of different symmetries. In those cases, and we have shown that the perovskite semiconductor $SrTiO_3$ is one of them, the pinning of the Fermi level inside the gap will decide for which symmetry the smallest decay parameter occurs; in the specific case of $SrTiO_3$ the two competing symmetries are Δ_1 and Δ_5. The implementation of complex band structure calculations in our SKKR program, will allow in the future to study semiconductors (or insulators) with more complicated structures like rutile TiO_2 and corundum Al_2O_3.

Appendix A

O(N) algorithm for the slab geometry

The solution of the Dyson equation, as discussed in section 4.5, is achieved through the calculation of the the scattering-path operator τ which, in the case of slab or supercell geometries, is given by

$$\tau = \mathrm{M}^{-1} = \left[(\Delta t^{-1}) - \mathrm{G}^{r}\right]^{-1} \tag{A.1}$$

I will present here the derivation of the algorithm used to calculate the diagonal and off-diagonal elements of τ in the case of the *slab* geometry. This algorithm was originally proposed by Godfrin [God91] and Wu *et al.* [WXP93], and extended to the supercell geometry by Zeller [Zel].

The matrix M, given in (A.1), assumes in the Principal Layer (PL) indices the form

$$M_{\cdot} = \begin{pmatrix} M_{1,1} & M_{1,2} & 0 & \cdots & \cdots & \cdots & 0 & M_{1,n} \\ M_{2,1} & M_{2,2} & M_{2,3} & 0 & \cdots & \cdots & 0 & 0 \\ 0 & M_{3,2} & M_{3,3} & \ddots & \ddots & \cdots & \vdots & \vdots \\ \vdots & 0 & \ddots & \ddots & \ddots & \ddots & \vdots & \vdots \\ \vdots & \vdots & \ddots & \ddots & M_{n-3,n-3} & M_{n-3,n-2} & 0 & \vdots \\ \vdots & \vdots & \cdots & \ddots & M_{n-2,n-3} & M_{n-2,n-2} & M_{n-2,n-1} & 0 \\ 0 & 0 & \cdots & \cdots & 0 & M_{n-1,n-2} & M_{n-1,n-1} & M_{n-1,n} \\ M_{n,1} & 0 & \cdots & \cdots & \cdots & 0 & M_{n,n-1} & M_{n,n} \end{pmatrix} \tag{A.2}$$

where the elements $M_{p,q}$ are given by Eq. (4.31), and n is the number of PL in the systems. The tridiagonal form of the matrix can be obtained only for a pseudo-

onedimensional cell, i.e. when the cell spans over one direction more than over the other two, as in the case of our layered systems; this is not valid for a general form of the cell, where only sparse matrix algorithm can be applied. The elements $M_{1,n}$ and $M_{n,1}$ arise because of the coupling between the atoms in the left and right side of the cell due to the periodic repeat of the cell in all the dimension; if the cell is repeated only in 2 dimensions, as it happens in the case of a slab calculation, these two blocks vanish, and the matrix M from cyclic tridiagonal becomes tridiagonal.

I give in the following the algorithm in the orginal notation proposed by Godfrin [God91], and rederive it afterwards in a more handy notation.

The elements of the inverse G of a n-block tridiagonal matrix are given, for $1 \leq p, q \leq n$, by

$$G_{p,p} = [M_{p,p} - X_p - Y_p]^{-1} \tag{A.3}$$

$$G_{p,q} = -[M_{p,p} - Y_p]^{-1} M_{p,p+1} G_{p+1,q} \quad \text{for } p < q \tag{A.4}$$

$$G_{p,q} = -[M_{p,p} - X_p]^{-1} M_{p,p-1} G_{p-1,q} \quad \text{for } p > q \tag{A.5}$$

where

$$X_n = 0 \tag{A.6}$$

$$X_{n-p} = M_{n-p,n-p+1} [M_{n-p+1,n-p+1} - X_{n-p+1}]^{-1} M_{n-p+1,n-p} \quad \text{for } 1 \leq p \leq n-1 \tag{A.7}$$

$$Y_1 = 0 \tag{A.8}$$

$$Y_{p+1} = M_{p+1,p} [M_{p,p} - Y_p]^{-1} M_{p,p+1} \quad \text{for } 1 \leq p \leq n-1 \tag{A.9}$$

A more transparent way to calculate the block elements of the inverse of a block tridiagonal matrix M is obtained factorizing the matrix M as

$$M = L^{-1} D^{-1} U^{-1} \tag{A.10}$$

where L and U are the products of very simple lower and upper block-triangular matrix,

$$L = \prod_{p=n-1}^{1} L_p = L_{n-1} L_{n-2} \cdots L_2 L_1 \tag{A.11}$$

$$U = \prod_{p=1}^{n-1} U_p = U_1 U_2 \cdots U_{n-2} U_{n-1} \tag{A.12}$$

and D is a block-diagonal matrices. Once this factorization is performed, the inverse of M can be calculated, simply inverting Eq. (A.10) , as

$$M^{-1} = U\,D\,L \tag{A.13}$$

The recursive factorization of the matrix M starts from the definition of the first diagonal block of the matrix D as the element $M_{1,1}^{-1}$; the matrix M, for the slab geometry, assumes thus the form

$$M = \begin{pmatrix} (D_1)^{-1} & M_{1,2} & 0 & \cdots & 0 \\ M_{2,1} & M_{2,2} & M_{2,3} & \cdots & 0 \\ 0 & M_{3,2} & M_{3,3} & \cdots & 0 \\ \vdots & \vdots & \vdots & \ddots & \vdots \\ 0 & 0 & 0 & \cdots & M_{n,n} \end{pmatrix} \tag{A.14}$$

If we choose the first lower triangular matrix as

$$L_1 = \begin{pmatrix} 1 & 0 & 0 & \cdots & 0 \\ -M_{2,1}\,D_1 & 1 & 0 & \cdots & 0 \\ 0 & 0 & 1 & \cdots & 0 \\ \vdots & \vdots & \vdots & \ddots & \vdots \\ 0 & 0 & 0 & \cdots & 1 \end{pmatrix} \tag{A.15}$$

and perform the matrix multiplication $L_1\,M$, we obtain

$$L_1\,M = \begin{pmatrix} (D_1)^{-1} & M_{1,2} & 0 & \cdots & 0 \\ 0 & (D_2)^{-1} & M_{2,3} & \cdots & 0 \\ 0 & M_{3,2} & \ddots & \cdots & 0 \\ \vdots & \vdots & \vdots & \ddots & \vdots \\ 0 & 0 & 0 & \cdots & M_{n,n} \end{pmatrix} \tag{A.16}$$

where we defined the second diagonal block of D as

$$(D_2) = (M_{2,2} - M_{2,1}\,D_1\,M_{1,2})^{-1} \tag{A.17}$$

Similarly we define the first upper triangular matrix U_1 as

$$U_1 = \begin{pmatrix} 1 & -D_1\,M_{1,2} & 0 & \cdots & 0 \\ 0 & 1 & 0 & \cdots & 0 \\ 0 & 0 & 1 & \cdots & 0 \\ \vdots & \vdots & \vdots & \ddots & \vdots \\ 0 & 0 & 0 & \cdots & 1 \end{pmatrix} \tag{A.18}$$

and by means of the product between $L_1\,M$ and U_1, we obtain

$$L_1\,M\,U_1 = \begin{pmatrix} (D_1)^{-1} & 0 & 0 & \cdots & 0 \\ 0 & (D_2)^{-1} & M_{2,3} & \cdots & 0 \\ 0 & M_{3,2} & M_{3,3} & \cdots & 0 \\ \vdots & \vdots & \vdots & \ddots & \vdots \\ 0 & 0 & 0 & \cdots & M_{n,n} \end{pmatrix} \tag{A.19}$$

The effect of the multiplication of M with the two triangular matrices L_1 and U_1 is to "clean" the first row and and the first column from the off-diagonal elements. The matrix thus obtained has the same form as the initial M matrix and with the appropriate choice of the L and U matrices, the procedure can be repeated until only the diagonal blocks remain. This happens after $n-1$ recursive moltiplication by L_p and U_p, and the matrix D^{-1}, which is the one in Eq. (A.10), turns out to be given by

$$D^{-1} = \left[\prod_{p=n-1}^{1} L_p\right] M \left[\prod_{p=1}^{n-1} U_p\right] = \begin{pmatrix} (D_1)^{-1} & 0 & 0 & \cdots & 0 \\ 0 & (D_2)^{-1} & 0 & \cdots & \vdots \\ 0 & 0 & \ddots & \ddots & \vdots \\ \vdots & \vdots & \ddots & (D_{n-1})^{-1} & 0 \\ 0 & \cdots & \cdots & 0 & (D_n)^{-1} \end{pmatrix} \tag{A.20}$$

and the p-th block element of the matrix D, with $p = 2, 3, ..., n$, is calculated recursively by the formula

$$D_p = (M_{p,p} - M_{p,p-1}\,D_{p-1}\,M_{p-1,p})^{-1} \tag{A.21}$$

The factorization is now complete and we can start to "back"-factorize the matrix D in order to calculate the elements of the matrix M^{-1}, by means of

$$\tau = \mathrm{M}^{-1} = \left[\prod_{p=1}^{n-1} U_p\right] D \left[\prod_{p=n-1}^{1} L_p\right] \tag{A.22}$$

After the first back-factorization step, i.e. $U_{n-1}\,D\,L_{n-1}$, we obtain the matrix

$$\tilde{M}_{n-1} = U_{n-1}\,D\,L_{n-1} = \begin{pmatrix} D_1 & 0 & 0 & \cdots & 0 & 0 \\ 0 & D_2 & \ddots & \cdots & 0 & 0 \\ 0 & \ddots & \ddots & \ddots & \vdots & \vdots \\ \vdots & \vdots & \ddots & D_{n-2} & 0 & 0 \\ 0 & 0 & \cdots & 0 & \tau_{n-1,n-1} & W_{n-1} \\ 0 & 0 & \cdots & 0 & V_{n-1} & \tau_{n,n} \end{pmatrix} \tag{A.23}$$

where

$$\tau_{n,n} = D_n \quad , \tag{A.24}$$

$$\tau_{n-1,n-1} = D_{n-1} + D_{n-1}\, M_{n-1,n}\, \tau_{n,n}\, M_{n,n-1}\, D_{n-1} \quad , \tag{A.25}$$

$$V_{n-1} = -D_n\, M_{n,n-1}\, D_{n-1} \quad , \tag{A.26}$$

$$W_{n-1} = -D_{n-1}\, M_{n-1,n}\, D_n \tag{A.27}$$

Proceeding recursively with such multiplication one notes that each matrix $\tilde{M}_p = U_p\, \tilde{M}_{p+1}\, L_p$ differs from the previous one $\tilde{M}_{p+1} = U_{p+1}\, U_{p+2} \cdots U_{n-1}\, D\, L_{n-1} \cdots L_{p+2}\, L_{p+1}$ only in the elements belonging to the p-th row and column, starting from the diagonal element $\tau_{p,p}$; this procedure is repeated up to the knowledge of $\tilde{M}_1$ which is obviously the seeked matrix τ. The final algorithm implemented in the code for the calculation of the diagonal and off-diagonal elements of the matrix τ is, resuming also the factorization step, the following:

- One defines the first block of the matrix D as $D_1 = (M_{1,1})^{-1}$.
- The elements $D_p = (M_{p,p} - M_{p,p-1}\, D_{p-1}\, M_{p-1,p})^{-1}$ are calculated recursively for $p = 2, 3, ..., n$.
- One defines $\tau_{n,n} = D_n$.
- All the other elements of the matrix τ are calculated for $q = n, n-1, ..., 1$ as follows:

$$\tau_{p,q} = \begin{cases} D_p + D_p\, M_{p,p+1}\, \tau_{p+1,p+1}\, M_{p+1,p}\, D_p & \text{for } p = q, \text{ and } p = n-1, n-2, ..., 1 \\ -D_p\, M_{p,p+1}\, \tau_{p+1,q} & \text{for } p < q, \text{ and } p = q-1, q-2, ..., 1 \\ C_p\, \tau_{p-1,q} & \text{for } p > q, \text{ and } p = q+1, q+2, ..., n \\ \text{with } C_p = -\left[M_{p,p} - (D_p)^{-1} - (\tau_{p,p})^{-1}\right]^{-1} M_{p,p-1} \end{cases} \tag{A.28}$$

The algorithm used to calculate the diagonal elements of the matrix τ, given in the first row of Eq. (A.28), is equivalent to the one given by Godfrin [God91] in Eq. (A.3); the proof for this equality can be found in [Wil97]. The formulas in Eq. (A.28) used to calculate the off-diagonal elements of the matrix τ are the same as the ones given in Eq. (A.4) and (A.5) where for the X and Y matrices hold the two relations $D_p = [M_{p,p} - Y_p]^{-1}$ and $X_p = (D_p)^{-1} - (\tau_{p,p})^{-1}$.

Examining closely the above formula, one realizes that for the calculation of the element $\tau_{p,q}$, for $p < q$ only the elements $\tau_{q,q}\ \tau_{q-1,q}\ \cdots\ \tau_{p+1,q}$ with decresing row number p, and for $p > q$ only the elements $\tau_{q,q}\ \tau_{q+1,q}\ \cdots \tau_{p-1,q}$ with increasing row number p are needed (see Fig. (A.1*a*) where the arrows show the order in which the blocks have to be calculated). The calculation of all the elements in the matrix τ

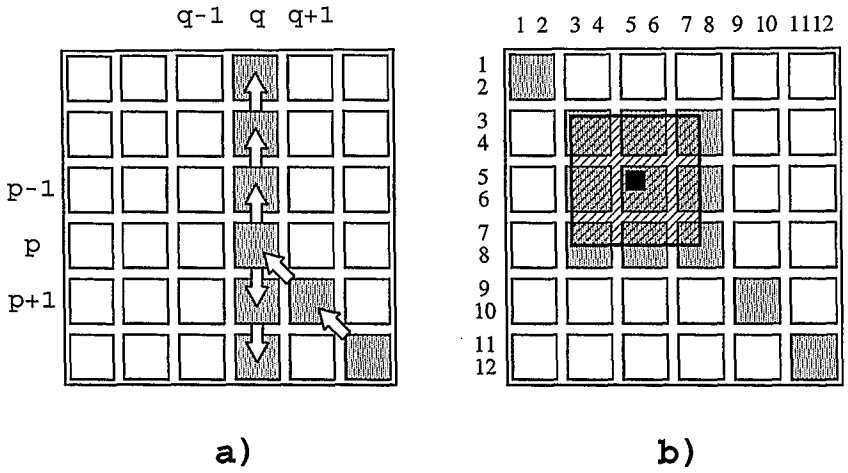

Figure A.1: *a*) Recursive procedure for the calculation of the diagonal and off-diagonal elements of the inverse matrix M^{-1}; *b*) example of off-diagonal elements needed for an impurity calculation; the black square shows the layer in which the impurity is placed.

requires a n^2 effort, while the calculation of the diagonal elements $\tau_{p,p}$, which are the only ones needed in the self-consistency procedure, scales linearly with n.

In the case of an impurity calculation, the Green's functions $G^{n,n'}$ which describe the multiple scattering processes inside a cluster C of atoms around the impurity have to be calculated. Only the blocks of the matrix τ which contains the elements which couple the layers spanned by the cluster are needed. For instance for the (001) *fcc* slab, a cluster of 43 atoms (up to the $3rd$ shell) spans over 5 layers, i.e. the central one + 2 layers on both sides; if the total number of layers is 12, the number N_p of layers in each PL = 2, and the impurity is placed at the 5-th layer, the elements which have to be calculated are the ones in gray in Fig. (A.1*b*), where the number refers to the layer indices, and the grid indicates the extent over the layer indices of the cluster C.

Bibliography

[AAB+90] H. Akai, M. Akai, S. Blügel, B. Drittler, H. Ebert, K. Terakura, R. Zeller, and P. H. Dederichs. Theory of hyperfine interactions in metals. *Progr. Theor. Phys. Suppl.*, 101:11, 1990.

[AEP59] V. Arp, D. Edmonds, and R. Petersen. Hyperfine coupling in CoFe and CoNi alloys as determined by heat capacity measurements. *Phys. Rev. Letters*, 3:212, 1959.

[AJ84] O. K. Andersen and O. Jepsen. Explicit, First-Principles Tight-Binding Theory. *Phys. Rev. Letters*, 53:2571, 1984.

[AK99] H. Akai and T. Kotani. Theory of hyperfine fields of iron. *Hyperfine Interactions*, 121:3, 1999.

[APJ86] O. K. Andersen, Z. Pawlowska, and O. Jepsen. Illustration of the linear-muffin-tin-orbital tight-binding representation: Compact orbitals and charge density in Si. *Phys. Rev. B*, 34:5253, 1986.

[APS92] O. K. Andersen, A. V. Postnikov, and S. Yu. Savrasov. The muffin-tin-orvital point of view. *Mat. Res. Soc. Symp. Proc.*, 253:37, Material Research Society, Pittsbburgh, 1992. edited by W. H. Butler, P. H. Dederichs, A. Gonis and R. L. Weaver.

[BAZD87] S. Blügel, H. Akai, R. Zeller, and P. H. Dederichs. Hyperfine fields of 3it d and $4d$ impurities in nickel. *Phys. Rev. B*, 35:3271, 1987.

[BB97] H. Beckmann and G. Bergmann. Magnetism of Rh and Ru atoms, clusters and monolayers on Au and Ag surfaces. *Phys. Rev. B*, 55:14350, 1997.

[BBF+88] M. N. Baibich, J. M. Broto, A. Fert, F. Nguyen Van Dau, F. Petroff, P. Etienne, G. Creuzet, A. Friederich, and J. Chazelas. Giant Magne-

toresistance of (001) Fe/(001) Cr Magnetic Superlattices. *Phys. Rev. Letters*, 61:2472, 1988.

[BDZD89] S. Blügel, B. Drittler, R. Zeller, and P. H. Dederichs. Magnetic properties of $3d$ transition metal monolayers on metal substrates. *Appl. Physics A*, 49:547, 1989.

[BEA96] M. Battocletti, H. Ebert, and H. Akai. Influence of gradient corrections to the local-density-approximation on the calculation of hyperfine fields in ferromagnetic Fe, Co and Ni. *Phys. Rev. B*, 53:9776, 1996.

[Bee67] J. L. Beeby. The density of electrons in a perfect or imperfect lattice. *Proc. Roy. Soc. (London) A*, 302:113, 1967.

[Bes96] F. Besenbacher. Scanning tunneling microscopy studies of metals surfaces. *Rep. Prog. Phys.*, 59:1737, 1996.

[BGSZ89] G. Binash, P. Grünberg, F. Saurenbach, and W. Zinn. Enhanced magnetoresistence in layered magnetic structures with antiferromagnetic interlayer exchange. *Phys. Rev. B*, 39:4828, 1989.

[BHF+94] J.-P. Bucher, E. Hahn, P. Fernandez, C. Massobrio, and K. Kern. Transition from one- to two-dimensional growth of Cu on Pd(110) promoted by cross-exchange migration. *Europhys. Lett.*, 27:473, 1994.

[BHS+00] D. I. Bazhanov, W. Hergert, V. S. Stepanyuk, A. A. Katsnelson, P. Rennert, K. Kokko, and C. Demangeat. One-dimensional magnetism of Rh chains on the Ag(001) surface. *Phys. Rev. B*, 72:???, 2000.

[Bih] G. Bihlmayer. Private communications.

[BKMK98] M. Blanc, K. Kuhnke, V. Marsico, and K. Kern. Probing step decoration by grazing-incidence helium scattering. *Surf. Sci.*, 414:L964, 1998.

[Blü92a] S. Blügel. Ferromagnetism of $4d$-metal monolayers on Ag, Cu and Pd(001) surfaces. *Europhys. Lett.*, 18:257, 1992.

[Blü92b] S. Blügel. Two-dimensional ferromagnetism of $3d$,$4d$ and $5d$ transition metal monolayers on noble metal (001) substrates. *Phys. Rev. Letters*, 68:851, 1992.

[BPD89] S. Blügel, D. Pescia, and P. H. Dederichs. Ferromagnetism versus antiferromagnetism of the Cr(001) surface. *Phys. Rev. B*, 39:R1392, 1989.

[Bre30] G. Breit. *Phys. Rev.*, 35:1447, 1930.

[BSD88] P. Blaha, K. Schwarz, and P. H. Dederichs. First-principles calculation of the electric-field gradient in *hcp* metals. *Phys. Rev. B*, 37:2792, 1988.

[BSLB96] H. Beckmann, R. Schäfer, W. Li, and G. Bergmann. First observation of a fully magnetic $4d$ impurity on the surface of Au. *Europhys. Lett.*, 33:563, 1996.

[BZLD84] P. J. Braspenning, R. Zeller, A. Lodder, and P. H. Dederichs. Selfconsistent cluster calculations with correct embedding for $3d$, $4d$ and some *sp* impurities in copper. *Phys. Rev. B*, 29:703, 1984.

[BZW+97] W. H. Butler, X.-G. Zhang, X. Wang, J. van Ek, and J. M. MacLaren. Electronic structure of FM|semiconductor|FM spin tunneling structures. *J. Appl. Physics*, 81:5518, 1997.

[CA80] D. M. Ceperley and B. J. Alder. Ground state of the electrons gas by a stochastic method. *Phys. Rev. Letters*, 45:566, 1980.

[CH00] S. Cottenier and H. Hass. Hyperfine fields and local lattice relaxation at $4d$ and $5sp$ impurities in *bcc* iron. *Phys. Rev. B*, 62:461, 2000.

[CL96] J. R. Chelikowsky and S. G. Louie. *Quantum Theory of Real Materials.* Kluwer Academic Publishers, Boston-Dordrecht-London, 1996.

[CLE93] M. F. Crommie, C. P. Lutz, and D. M. Eigler. *Science*, 262:218, 1993.

[CMF88] A. Continenza, S. Massidda, and A. J. Freeman. Structural and electronic properties of bulk ZnSe. *Phys. Rev. B*, 38:12996, 1988.

[CP85] L .L. Chang and K. Ploog. *Molecular Beam Epitaxy and Heterostructures.* Martinus Nijhoff Publishers, Dordrecht/Boston/Lancaster, 1985.

[Cun74] S. L. Cunningham. Special points in the two-dimensional Brillouin zone. *Phys. Rev. B*, 10:4988, 1974.

[DCE+00] A. Dallmeyer, C. Carbone, W. Eberhardt, C. Pampuch, O. Rader, W. Gudat, P. Gambardella, and K. Kern. Electronic states and magnetism of monoatomic Co and Cu wires. *Phys. Rev. B*, 61:R5133, 2000.

[DDP98] J. Dorantes-Dávila and G. M. Pastor. Magnetic anisotropy of one-dimensional nanostructures of transition metals. *Phys. Rev. Letters*, 81:208, 1998.

[DDZ92] P. H. Dederichs, B. Drittler, and R. Zeller. A full-potential KKR Green's function method for impurities in metals. *Mat. Res. Soc. Symp. Proc.*, 253:185, Material Research Society, Pittsbburgh, 1992. edited by W. H. Butler, P. H. Dederichs, A. Gonis and R. L. Weaver.

[DJML93] J. Dekoster, E. Jedryka, C. Mény, and G. Langouche. Epilayer-induced structural transition to *bcc* Co during epitaxial growth of Co/Fe superlattices. *Europhys. Lett.*, 22:433, 1993.

[Dri91] B. Drittler. *KKR-Greensche Funktionsmethode für das volle Zellpotential.* PhD thesis, RWTH-Aachen, 1991.

[DSB+89] B. Drittler, N. Stefanou, S. Blügel, R. Zeller, and P. H. Dederichs. Electronic structure and magnetic properties of dilute Fe alloys with transition-metal impurities. *Phys. Rev. B*, 40:8203, 1989.

[DSR+94] J. Dekoster, B. Swinnen, M. Rots, G. Langouche, and E. Jedryka. Impurity hyperfine fields in metastable body centered cubic Co. *J. Appl. Physics*, 76:6428, 1994.

[DWZD89] B. Drittler, M. Weinert, R. Zeller, and P. H. Dederichs. First-principles calculation of impurity-solution energies in Cu and Ni. *Phys. Rev. B*, 39:930, 1989.

[DZAE91] P. H. Dederichs, R. Zeller, H. Akai, and H. Ebert. Ab-initio calculations of the electronic structure of impurities and alloys of ferromagnetic transition metals. *J. Magn. Magn. Materials*, 100:241, 1991.

[EB96] H. Ebert and M. Battocletti. Spin and orbital polarized relativistic multiple scattering theory with application to Fe, Co and Ni and Fe_xCo_{1-x}. *Solid State Commun.*, 98:785, 1996.

[Ebe] H. Ebert. *NMR-Untersuchungen zur elektronischen Struktur metallischer Systeme - Theorie und Experiment.* Dissertation Ludwig Maximilians Universität, München, (1985).

[Eco79] E. N. Economou. *Green's functions in quantum physics.* Springer-Verlag, Berlin, 1979.

[ESG88] H. Ebert, P. Strange, and B. L. Gyorffy. The influence of relativistic effects on the magnetic moments and hyperfine fields of the Fe, Co and Ni. *J. Phys. F: Met. Phys.*, 18:L135, 1988.

[ESG89] H. Ebert, P. Strange, and B. L. Gyorffy. A fully relativistic description of the hyperfine interaction in magnetic systems. *Hyperfine Interactions*, 51:929, 1989.

[EWG+87] H. Ebert, H. Winter, B. Gyorffy, D. D. Johnson, and F. J. Pinski. A theoretical study of the environmental effects on the hyperfine fields of Ni and Fe in $Ni_{0.75}Fe_{0.25}$. *Solid State Commun.*, 64:1011, 1987.

[EWJP90] H. Ebert, H. Winter, D. D. Johnson, and F. J. Pinski. Theoretical study of the hyperfine fields in *bcc*-Fe_xCo_{1-x} alloys. *J. Phys. C: Solid State Phys.*, 2:443, 1990.

[Fei95] P. J. Feibelman. Energetics of steps on Pt(111). *Phys. Rev. B*, 52:16845, 1995.

[Fer27] E. Fermi. Un metodo statistico per la determinazione di alcune proprietá dell'atomo. *Rend. Accad., Lincei*, 6:602, 1927.

[Fer30] E. Fermi. *Z. Physik*, 60:320, 1930.

[FKBK99] O. Fruchart, M. Klaua, J. Barthel, and J. Kirschner. Self-organized growth of nanosized vertical magnetic Co pillars on Au(111). *Phys. Rev. Letters*, 83:2769, 1999.

[Ful91] B. Fultz. Kinetics of short-range and long-range *b*2 ordering in FeCo. *Phys. Rev. B*, 44:9805, 1991.

[GBB+00a] P. Gambardella, M. Blanc, H. Brune, K. Kuhnke, and K. Kern. One-dimensional metal chains on Pt vicinal surfaces. *Phys. Rev. B*, 61:2254, 2000.

[GBB+00b] P. Gambardella, M. Blanc, L. Bürgi, K. Kuhnke, and K. Kern. Co growth on Pt(997): From monoatomic chains to monolayer completion. *Surf. Sci.*, 449:93, 2000.

[GE96] G. Y. Guo and H. Ebert. First-principles study of the magnetic hyperfine field in Fe and Co multilayers. *Phys. Rev. B*, 53:2492, 1996.

[God91] Elena M. Godfrin. A method to compute the inverse of an n-block tridiagonal quasi-Hermitian matrix. *J. Phys.: Condensed Matter*, 3:7843, 1991.

[GSP+86] P. Grünberg, R. Schreiber, Y. Pang, M. B. Brodsky, and H. Sowers. Layered Magnetic Structures: Evidence for Antiferromagnetic Coupling of Fe Layers across Cr Interlayers. *Phys. Rev. Letters*, 57:2442, 1986.

[HB98] S. Handschuh and S. Blügel. Magnetic exchange coupling of $3d$ metal monolayers on Fe(001). *Solid State Commun.*, 105:633, 1998.

[HBG+91] Ph. Houdy, P. Boher, F. Giron, F. Pierre, C. Chappert, P. Beauvillain, K. Le Dang, P. Veillet, and E. Velu. Magnetic and structural poperties of rf-sputtered Co/Fe and Co/Cr multilayers. *J. Appl. Physics*, 69:5667, 1991.

[Hei62] V. Heine. *Proc. Roy. Soc. (London)*, 81:300, 1962.

[HFP89] H. H. Hamdeh, B. Fultz, and D. H. Pearson. Mössbauer spectrometry study of the hyperfine fields and electronic structure of Fe-Co alloys. *Phys. Rev. B*, 39:11233, 1989.

[HK64] P. Hohenberg and W. Kohn. Inhomogeneous electron gas. *Phys. Rev.*, 136:864, 1964.

[HM97] Y. Huang and W. F. McColl. Analytical inversion of general tridiagonal matrices. *J. Phys. A: Math. Gen.*, 30:7919, 1997.

[Hol75] N. A. W. Holzwarth. Theory of impurity scattering in dilute metal alloys based on the muffing-tin model. *Phys. Rev. B*, 11:3718, 1975.

[HOMW98] F. J. Himpsel, J. E. Ortega, G. J. Mankey, and R. F. Willis. Magnetic nanostructures. *Adv. Phys.*, 47:511, 1998.

[HS80] M. A. Van Hove and G. A. Somorjai. A new microfacet notation high-Miller-index surfaces of cubic materials with terrace, step and kink structures. *Surf. Sci.*, 92:489, 1980.

[HS83] V. Heine and J. H. Samson. Magnetic, chemical and structural ordering in transition metals. *J. Phys. F: Met. Phys.*, 13:2155, 1983.

[Isi25] E. Ising. *Z. Physik*, 31:253, 1925.

[Jan79] J. F. Janak. Calculated hyperfine fields and their pressure derivatives in Fe, Co and Ni. *Phys. Rev. B*, 20:2206, 1979.

[JG89] R. O. Jones and O. Gunnarsson. The density functional formalismm its applications and prospects. *Rev. Mod. Phys.*, 61:689, 1989.

[JMA78] O. Jepsen, J. Madsen, and O. K. Andersen. Band structure of thin films by the linear augmented-plane-wave method. *Phys. Rev. B*, 18:605, 1978.

[JMJ86] P. Jiang, P. M. Marcus, and F. Jona. Relaxation at clean metal surfaces. *Solid State Commun.*, 59:275, 1986.

[Jul75] M. Julliere. *Phys. Letters A*, 54:225, 1975.

[JWP96] J. P. Jay, M. Wójcik, and P. Panissod. Hyperfine field and ordering in *bcc* CoFe alloys studied by $^{5}9$Co NMR and Monte-Carlo simulation. *Z. Physik B*, 101:471, 1996.

[KA98] T. Kotani and H. Akai. Optimized-effective-potential method with exact exchange and exact RPA correlation: 3d metals. *J. Magn. Magn. Materials*, 177-181:569, 1998.

[Kor47] J. Korringa. On the calculation of the energy of a Bloch wave in a metal. *Physica*, 13:392, 1947.

[Kot98] T. Kotani. An optimized-effective-potential method for solids with exact exchange and random-phase approximation correlation. *J. Phys.: Condensed Matter*, 10:9241, 1998.

[KPBZ87] B. M. Klein, W. E. Pickett, L. L. Boyer, and R. Zeller. Theory of F centers in the alkaline-earth oxides MgO and CaO. *Phys. Rev. B*, 35:5802, 1987.

[KPF79] H. Krakauer, M. Posternak, and A. J. Freeman. Linearized augmented plane-wave method for the electronic band structure of thin films. *Phys. Rev. B*, 19:1706, 1979.

[KR54] W. Kohn and N. Rostoker. Solution of the Schrödinger equation in periodic lattices with an application to metallic lithium. *Phys. Rev.*, 94:1111, 1954.

[KR61] W. Kohn and N. Rostoker. Solution of the Schrödinger equation in periodic lattices with an application to metallic lithium. *Annals of Physics*, 15:63, 1961.

[Kra83] K. S. Krane. Dilute impurity hyperfine fields. *Hyperfine Interactions*, 15-16:1069, 1983.

[KS65] W. Kohn and L. J. Sham. Self-consistent equations including exchange and correlation effects. *Phys. Rev.*, 140:A1133, 1965.

[KSP+00] T. Korhonen, A. Settels, N. Papanikolaou, R. Zeller, and P. H. Dederichs. Lattice relaxations and hyperfine fields of heavy impurities in fe. *Phys. Rev. B*, 62:452, 2000.

[KYTW95] S. Kimura, J. Yamauchi, M. Tsukada, and S. Watanabe. First-principles study on electronic structure of the (001) surface of $SrTiO_3$. *Phys. Rev. B*, 51:11049, 1995.

[Lan96] P. Lang. *Theory of Interlayer Exchange Coupling: Co-Bilayers in Cu.* PhD thesis, RWTH-Aachen, 1996.

[LSW+94] P. Lang, V. S. Stepanyuk, K. Wildberger, R. Zeller, and P. H. Dederichs. Local moments of $3d$, $4d$ and $5d$ atoms at Cu and Ag (001) surfaces. *Solid State Commun.*, 92:755, 1994.

[Mac78] A. H. MacDonald. Coment on special points for Brillouin-zone integrations. *Phys. Rev. B*, 15:5897, 1978.

[Mat72] L. F. Mattheiss. Energy bands for $KNiF_3$, $SrTiO_3$, $KMoO_3$, and $KTaO_3$. *Phys. Rev. B*, 6:4718, 1972.

[MEJS95] S. Mirbt, O. Eriksson, B. Johansson, and H. L. Skriver. Magnetic coupling in $3d$ transition-metal monolayers and bilayers on *bcc* (100) iron. *Phys. Rev. B*, 52:15070, 1995.

[MHS92] M. Methfessel, D. Hennig, and M. Scheffler. Trends of the surface relaxations, surface energies and work functions of the $4d$ transition metals. *Phys. Rev. B*, 46:4816, 1992.

[MJW71] P.M. Marcus, J. F. Janak, and A. R. Williams. *Computational Methods in Band Theory: Efficient Numerical Techniques for the Calculation of KKR Structure Constants.* Plenum Press, New York, 1971.

[MKWM95] J. S. Moodera, L. R. Kinder, T. M. Wong, and R. Meservey. Large magnetoresistance at room temperature in ferromagnetic thin film tunnel junctions. *Phys. Rev. Letters*, 74:3273, 1995.

[MMZ87] I. Mertig, E. Mrosan, and P. Ziesche. *Multiple Scattering Theory of Point Defects in Metals: Electronic Properties.* BSB Teubner-Texte, Leipzig, 1987.

[MP76] H. J. Monkhorst and J. D. Pack. Special points for Brillouin-zone integrations. *Phys. Rev. B*, 13:5188, 1976.

[MPD00] Ph. Mavropoulos, N. Papanikolaou, and P. H. Dederichs. Complex band structure and tunneling through Ferromagetic/Insulator/Ferromagnetic junctions. *Phys. Rev. Letters*, 85:1088, 200.

[MSN+98] Ph. Mavropoulos, N. Stefanou, B. Nonas, R. Zeller, and P. H. Dederichs. Hyperfine fields of *sp* impurities on Ni and Fe surfaces. *Phys. Rev. Letters*, 81:1505, 1998.

[MSYN76] Y. Muraoka, M. Shiga, H. Yasuoka, and Y. Nakamura. NMR study of ordered and disordered Fe-Co alloy. *J. Phys. Soc. Japan*, 40:414, 1976.

[MT95] T. Miyazaki and N. Tezuka. Giant magnetic tunneling effect in $Fe/Al_2O_3/Fe$ junction. *J. Magn. Magn. Materials*, 139:L231, 1995.

[NJS99] A. M. N. Niklasson, B. Johansson, and H. L. Skriver. Interface magnetism of 3d transition metals. *Phys. Rev. B*, 59:6373, 1999.

[Non] B. Nonas. Private communications.

[Non00] B. Nonas. *Magnetische Adatome und Nanostrukturen auf Metalloberflächen.* PhD thesis, RWTH-Aachen, 2000.

[NWZ+98] B. Nonas, K. Wildberger, R. Zeller, P. H. Dederichs, and B. L. Gyorffy. Magnetic properties of $4d$ impurities on the (001) surfaces of nickel and iron. *Phys. Rev. B*, 57:84, 1998.

[NWZD98] B. Nonas, K. Wildberger, R. Zeller, and P. H. Dederichs. Energetics of $3d$ impurities on the (001) surface of iron. *Phys. Rev. Letters*, 80:4574, 1998.

[Pap] N. Papanikolaou. Private communications.

[PMR90] S. S. P. Parkin, N. More, and K. P. Roche. Oscillations in Exchange Coupling and Magnetoresistance in Metallic Superlattice Structures: Co/Ru, Co/Cr and Fe/Cr. *Phys. Rev. Letters*, 64:2304, 1990.

[Pri85] G. A. Prinz. Stabilization of *bcc* Co via Epitaxial Growth on GaAs. *Phys. Rev. Letters*, 54:1051, 1985.

[PTVF86] W. H. Press, S. A. Teukolsky, W. T. Vetterling, and B. P. Flannery. *Numerical Recipes in FORTRAN: the art of scientific computing.* Cambridge University Press, Cambridge-New York-Melbourne, 1986.

[PY89] R. G. Parr and W. Yang. *Density-functional theory of atoms and molecules.* Oxford University Press, New York, 1989.

[PZD80] R. Podloucky, R. Zeller, and P. H. Dederichs. Electronic structure of magnetic impurities calculated from first principles. *Phys. Rev. B*, 22:5777, 1980.

[PZDS97] N. Papanikolaou, R. Zeller, P. H. Dederichs, and N. Stefanou. Lattice distortion in Cu-based dilute alloys: A first-principles study by the KKR Green's-function method. *Phys. Rev. B*, 55:4157, 1997.

[RDF+97] B.-U. Runge, M. Dippel, G. Filleböck, K. Jacobs, U. Kohl, and G. Schatz. Induced magnetic hyperfine field at Ag sites near an Fe(100)/Ag(100) interface. *Phys. Rev. Letters*, 79:3054, 1997.

[RHB+93] H. Röder, E. Hahn, H. Brune, J.-P. Bucher, and K. Kern. Building one- and two-dimensional nanostructures by diffusion-controlled aggregation at surfaces. *Nature*, 366:141, 1993.

[RIV00] R. Robles, J. Izquierdo, and A. Vega. Magnetic behaviour of monoatomic Co wires on Pd(110). *Phys. Rev. B*, 61:6848, 2000.

[Rub68] M. Rubinstein. Hyperfine field spectra of binary Fe-Co alloys: Nuclear magnetic resonance of ^{5}7Fe and ^{5}9Co. *Phys. Rev.*, 172:277, 1968.

[SAZ90] N. Stefanou, H. Akai, and R. Zeller. An efficient numerical method to calculate shape truncation functions for Wigner-Seitz atomic polyhedra. *Comp. Phys. Commun.*, 60:231, 1990.

[SB96] R. Schäfer and G. Bergmann. Nb atoms on the surface of Ag, an unexpected Kondo system. *Solid State Commun.*, 98:45, 1996.

[SBZD87] N. Stefanou, P. J. Braspenning, R. Zeller, and P. H. Dederichs. Treatment of lattice relaxations in dilute alloys within the Korringa-Kohn-Rostoker Green's-function method. *Phys. Rev. B*, 36:6372, 1987.

[Sch88] G. Schatz. Surface studies with hyperfine probes. In E. Recknagel and J. C. Soares, editors, *Nuclear Physics Application on Materials Science*, NMR, page 297. Kluwer Academic Publishers, 1988.

[Set96] A. Settels. *Elektronische Struktur und Hyperfeineigenshaften von Störstellen in Halbleitern.* Diploma thesis, RWTH-Aachen, 1996.

[Set99] A. Settels. *Hyperfeineigenshaften und Gitterrelaxationen von Defekten in Halbleitern und Metallen.* PhD thesis, RWTH-Aachen, 1999.

[SHR+96] V. S. Stepanyuk, W. Hergert, P. Rennert, K. Wildberger, R. Zeller, and P. H. Dederichs. Magnetic dimers of transition-metal atoms on the Ag(001) surface. *Phys. Rev. B*, 54:14141, 1996.

[SHR+99] V. S. Stepanyuk, W. Hergert, P. Rennert, K. Wildberger, R. Zeller, and P. H. Dederichs. Imperfect magnetic nanostructures on a Ag (001) surface. *Phys. Rev. B*, 59:1681, 1999.

[SHW+96] V. S. Stepanyuk, W. Hergert, K. Wildberger, R. Zeller, and P. H. Dederichs. Magnetism of $3d$, $4d$ and $5d$ transition-metal impurities on Pd(001) and Pt(001) surfaces. *Phys. Rev. B*, 53:2121, 1996.

[Skr83] H. L. Skriver. *The LMTO-Method.* Springer-Verlag, New York, 1983.

[SMD+97] B. Swinnen, J. Meersschaut, J. Dekoster, G. Langouche, S. Cottenier, S. Demuynck, and M. Rots. Oscillation of the Fe and Co magnetic moments near the sharp (1 -1 0) Fe/Co interface. *Phys. Rev. Letters*, 78:362, 1997.

[SR91] H. L. Skriver and N. M. Rosengaard. Self-consistent Green's-function technique for surfaces and interfaces. *Phys. Rev. B*, 43:9538, 1991.

[SR92] H. L. Skriver and N. M. Rosengaard. Surface energy and work function of elemental metals. *Phys. Rev. B*, 46:7157, 1992.

[SS96] R. Stumpf and M. Scheffler. *Ab initio* calculations of energies and self-diffusion on flat and stepped surfaces of Al and their implications on crystal growth. *Phys. Rev. B*, 53:4958, 1996.

[SSK+97] J. Shen, R. Skomski, M. Klaua, H. Jenniches, S. Sundar Manoharan, and J. Kirschner. Magnetism in one dimension: Fe on Cu(111). *Phys. Rev. B*, 56:2340, 1997.

[SSM00] S. Saha, T. P. Sinha, and A. Mookerjee. Structural and optical properties od paraelectric $SrTiO_3$. *J. Phys.: Condensed Matter*, 12:3325, 2000.

[SSR85] M. P. López Sancho, J. M. López Sancho, and J. Rubio. Highly convergent schemes for the calculation of bulk and surface green functions. *J. Phys. F: Met. Phys.*, 15:851, 1985.

[Ste73] Mary Beth Stearns. On the origin of ferromagnetism and the hyperfine fields in Fe, Co and Ni. *Phys. Rev. B*, 8:4383, 1973.

[SÚWK94] L. Szunyogh, B. Újfalussy, P. Weinberger, and J. Kollár. Self-consistent localized KKR scheme for surfaces and interfaces. *Phys. Rev. B*, 49:2721, 1994.

[ŠV98] Ž. V. Šljivančanin and F. R. Vukajlović. Comment on "Oscillation of the Fe and Co magnetic moments near the sharp (1 - 1 0) interface". *Phys. Rev. Letters*, 80:1568, 1998.

[TAK94] Ch. Teichert, Ch. Ammer, and M. Klaua. *Phys. Status Solidi A*, 146:223, 1994.

[TDK+97] I. Turek, V. Drchal, J. Kudrnovský, M. Šob, and P. Weinberger. *Electronic structure of disordered alloys, surfaces and interfaces.* Kluwer Academic Publishers, Boston-Dordrecht-London, 1997.

[Tho27] L. H. Thomas. The calculation of atomic fields. *Proc. Camb. Phil. Soc.*, 23:542, 1927.

[TKŠ+95] I. Turek, J. Kudrnovský, M. Šob, V. Drchal, and P. Weinberger. Ferromagnetism of imperfect ultrathin Ru and Rh films on a Ag(001) substrate. *Phys. Rev. Letters*, 74:2551, 1995.

[vBH72] U. von Barth and L. Hedin. A local exchange-coorelation potential for the spin polarized case: I. *J. Phys. C: Solid State Phys.*, 5:1629, 1972.

[VRSK98] L. Vitos, A. V. Ruban, H. L. Skriver, and J. Kollár. The surface energy of metals. *Surf. Sci.*, 411:186, 1998.

[VSK99] L. Vitos, H. L. Skriver, and J. Kollár. The formation energy for steps and kinks on cubic transition metal surfaces. *Surf. Sci.*, 425:212, 1999.

[VWN80] S. H. Vosko, L. Wilk, and N. Nusair. Accurate spin-dependent electron liquid correlation energies for local spin density calculations: a critical analysis. *Can. J. Phys.*, 58:1200, 1980.

[WF92] R. Wu and A. J. Freeman. Possible $4d$ ferromagnetism of Rh and Ru overlayers on a Ag (001) substrate. *Phys. Rev. B*, 45:7222, 1992.

[Wil94] K. Wildberger. *Elektronische Struktur vob Punktdefekten an Oberflächen.* Diploma thesis, RWTH-Aachen, 1994.

[Wil97] K. Wildberger. *Tight-Binding-Korringa-Kohn-Rostoker-Methode und Grenzflächenreflektivität in magnetischen Schichtsystemen.* PhD thesis, RWTH-Aachen, 1997.

[WJP+97] M. Wójcik, J. P. Jay, P. Panissod, E. Jedryka, J. Dekoster, and G. Langouche. New phases and chemical short range order in co-deposited CoFe thin films with *bcc* structure: An NMR study. *Z. Physik B*, 103:5, 1997.

[WLZD95] K. Wildberger, P. Lang, R. Zeller, and P. H. Dederichs. Fermi-Dirac distribution in *ab initio* Green's-function calculations. *Phys. Rev. B*, 52:11502, 1995.

[WSL+95] K. Wildberger, V. S. Stepanyuk, P. Lang, R. Zeller, and P. H. Dederichs. Magnetic nanostructures: $4d$ clusters on Ag(001). *Phys. Rev. Letters*, 75:509, 1995.

[WXP93] S. Y. Wu, Z. L. Xie, and N. Potoczak. Feasibility study on the application of the method of the resolvent matrix to complex systems. *Phys. Rev. B*, 48:14826, 1993.

[WZD92] K. Willenborg, R. Zeller, and P. H. Dederichs. Magnetic $4d$ impurities in Ag. *Europhys. Lett.*, 18:263, 1992.

[WZD97] K. Wildberger, R. Zeller, and P. H. Dederichs. Screened KK-Green's-function method for layered systems. *Phys. Rev. B*, 55:10074, 1997.

[WZD+98] K. Wildberger, R. Zeller, P. H. Dederichs, J. Kudrnovský, and P. Weinberger. Interface reflectivities and quantum-well states in magnetic multilayers. *Phys. Rev. B*, 58:13721, 1998.

[YS97] B. D. Yu and M. Scheffler. *Ab initio* study of step formation and self-diffusion on Ag(100). *Phys. Rev. B*, 55:13916, 1997.

[Zah98] P. Zahn. *Screened Korringa-Kohn-Rostoker-Methode für Vielfachschichten.* PhD thesis, Technische Universität Dresden, 1998.

[ZD79] R. Zeller and P. H. Dederichs. Electronic structure of impurities in Cu, calculated self-consistently by korringa-kohn-rostoker green's function method. *Phys. Rev. Letters*, 42:1713, 1979.

[ZDD82] R. Zeller, J. Deutz, and P. H. Dederichs. Application of complex energy integration to selfconsistent electronic structure calculations. *Solid State Commun.*, 44:993, 1982.

[ZDÚ+95] R. Zeller, P. H. Dederichs, B. Újfalussy, L. Szunyogh, and P. Weinberger. Theory and convergence properties of the screened Korringa-Kohn-Rostoker method. *Phys. Rev. B*, 52:8807, 1995.

[Zel] R. Zeller. Private communications.

[Zel97] R. Zeller. Evaluation of the screened Korringa-Kohn-Rostoker method for accurate and large scale electronic-structure calculations. *Phys. Rev. B*, 55:9400, 1997.

[ZLDD92] R. Zeller, P. Lang, B. Drittler, and P. H. Dederichs. A full-potential KKR Green's function method to calculate the electronic structure of surfaces. *Mat. Res. Soc. Symp. Proc.*, 253:357, Material Research

Society, Pittsbburgh, 1992. edited by W. H. Butler, P. H. Dederichs, A. Gonis and R. L. Weaver.

Acknowledgments

In first place I would like to thank Prof. Dr. P. H. Dederichs for the interesting topics proposed and for many helpful discussions on the various subjects treated in this thesis. I thank him for his guidance and for the freedom left me during the thesis to deepen my research interests.

Many thanks also to Dr. R. Zeller for the interesting discussions and for the work spent in the parallelization of the SKKR program which relieved sensibly the computational effort needed for some of the results presented in this thesis. I thank him very much for the correction of the manuscript, too.

My gratitude goes to Prof. Dr. K. Schroeder for the correction of the summary of this thesis.

I thank Prof. Dr. G. Güntherodt for having accepted to be the second referee of this thesis.

Herewith I would like to thank Prof. Dr. H. Müller-Krumbhaar for the opportunity to graduate in his Institute.

I would like to thank Prof. F. Manghi for the friendly support and for the good hints.

My special regards go to Dr. N. Papanikolaou for the many interesting discussions and for the close and friendly collaboration during the realization of the up-to-date version of the SKKR program.

Furthermore I want to thank Dr. M. Freyss, H. Hoehler, Dr. I. Cabria, A. Baranov for the teamwork and for their friendship.

I would like to thank all the persons in the KKR group met during these three years for interesting discussions and for having contributed to a very nice atmosphere. In

particular I thank Dr. B. Nonas and Dr. Ph. Mavropoulos for the nice time spent together and for their friendship, Dr. A. Settels for having lost some time playing tennis and for his friendship and Dr. T. Korhonen for his friendship.

My gratitude goes to Fr. J. Gollnick, Prof. H.R. Schober, Dr. S. Blügel, Dr. D. Caprion, Ph. Kurz, Dr. S. Heinze and Wi. Kromen for having contributed to a very pleasant atmosphere in the institute.

I thank Dr. B. Chesca and J. Steinbrecher for their support.

My special thanks go to O. Wunnicke for the relaxing atmosphere in the office during the draft of this thesis and for his friendship. I thank him also for the tests on the surface energies, for the correction of part of the manuscript and for his light coffees.

My special regards go to J. Zabloudil for his support, friendship and for the nice time spent together during his visits in Jülich.

I have the pleasure to thank Dr. A. Lamura for the many tasty italian dinners we had together and for his friendship.

My gratitude goes to my friends in Italy, and among them A. Lugli, A. Vanossi, M. Campani and M. Fattori. Double thanks go to A. Lugli and A. Vanossi for the daily e-mails and "talks" and for their support.

Last but not least, my very best thanks go to my parents and my brother which with their lovely support constantly motivated me and helped me to overcome the difficult periods. It is therefore a pleasure to dedicate this thesis to them.

Valerio Bellini

Jülich, September 2000.

Forschungszentrum Jülich

Jül-3856
März 2001
ISSN 0944-2952